1225-0767(ISSN Print)
2287-6715(ISSN Online)
한국연구재단 우수등재학술지

# Journal of Ocean Engineering and Technology

Vol. 34, No. 4 (Serial Number 155)

August 2020

# 한국해양공학회지

KSOE

www.joet.org

KSOE The Korean Society of Ocean Engineers

Journal of Ocean Engineering and Technology
한국해양공학회지
Vol. 34 No. 4
(Serial Number 155)
August 31, 2020
www.JOET.org

## Editorial Board



## Research Ethics Board



**Published on** August 31, 2020
**Published by** The Korean Society of Ocean Engineers (KSOE)
Room1302, 13, Jungang-daero 180beon-gil, Dong-gu, Busan, 48821, Korea
TEL: +82-51-759-0656 FAX: +82-51-759-0657 E-mail: ksoehj@ksoe.or.kr URL: http://www.ksoe.or.kr
**Printed by** Hanrimwon Co., Ltd., Seoul, Korea E-mail: hanrim@hanrimwon.co.kr
**ISSN(print)** 1225-0767 **ISSN(online)** 2287-6715

This journal was supported by the Korean Federation of Science and Technology Societies (KOFST) grant funded by the Korean government.

Journal of Ocean Engineering and Technology
한국해양공학회지

# CONTENTS

Volume 34, Number 4 August, 2020

**<Original Research Articles>**



**<Review Article>**

# GENERAL INFORMATION

"Journal of Ocean Engineering and Technology" is the official journal published by "The Korean Society of Ocean Engineers (KSOE)". The ISO abbreviation is "J. Ocean Eng. Technol." and acronym is "**JOET**". It was launched in 1987. It is published bimonthly in February, April, June, August, October, and December each year. Supplement numbers are published at times.

Journal of Ocean Engineering and Technology (JOET) is a medium for the publication of original research and development work in the field of ocean engineering. JOET covers the entire range of issues and technologies related to the following topics:

Ships and offshore platforms: Design of marine structures; Resistance and propulsion; Seekeeping and maneuvering; Experimental and computational fluid dynamics; Ocean wave mechanics; Fatigue strength; Plasticity; Optimization and reliability; Arctic technology and extreme mechanics; Noise, vibration, and acoustics; Concrete engineering; Thermodynamics and heat transfer; Hydraulics and pneumatics;
Coastal civil engineering: Coastal structures; Port and harbor structures; Soil mechanics; Drilling and exploration; Hydraulics of estuary; Seismic engineering; Coastal disaster prevention engineering;
Ocean renewable energy platforms: Offshore wind turbines; Wave energy platforms; Tidal current energy platforms; Floating photovoltaic energy platforms;
Marine robots: Robot sensor system; Autonomous navigation; Robot equipments; Spatial information and communications; Underwater network; Design of underwater vehicles;
Multidisciplinary areas: Design for safety; IT-based design; IT-based production engineering; Welding mechanics; Control engineering; GPS and GIS; Inspection and sensor; Port and logistics; Leisure boat and deep see water; Offshore process systems engineering; Marine metallic materials; Marine organic materials; Marine Composite materials; Materials properties; Corrosion and Anti-corrosion; Tribology;

It contains original research articles, case reports, brief communications and reviews on technial issues. Conference papers, research papers, diploma papers and academic articles can be submitted.

All of the manuscripts are peer-reviewed. **JOET** has a system where two or more peer reviewers must review each submitted paper and it is operated very strictly.



**JOET** is being indexed in some prominent database such as Korean Citatation Index (KCI), Google Scholar, Science Central, Korea Science and Directory of Open Access Journals (DOAJ).

For correspondences concerning business matters, author needs to contact KSOE Secretariat by email or phone (e-mail: ksoehj@ksoe.or.kr or Tel: +82 51 759 0656). Correspondences for publication matters can be asked via email to the Editor-in-Chief (email: heroeswise2@gmail.com).

KSOE
Original Research Article

**Journal of Ocean Engineering and Technology** 34(4), 237-244 August, 2020
https://doi.org/10.26748/KSOE.2020.014

pISSN 1225-0767
eISSN 2287-6715

# Maneuvering Hydrodynamic Forces Acting on Manta-type UUV Using CFD

Seong-Eun Lee[1], Sung-Wook Lee[2] and Jun-Young Bae[3]

[1]*Graduated Student Naval Architecture and Ocean Engineering, KMOU, Busan, Korea*
[2]*Professor, Naval Architecture and Ocean Engineering, KMOU, Busan, Korea*
[3]*Professor, Department of Automobile & Mechanics, Dongju College, Busan, Korea*

**KEY WORDS:** Manta-type, Unmanned underwater vehicles(UUV), Model test, Computational fluid dynamics(CFD), Manoeuvring hydrodynamic forces

**ABSTRACT:** *In this study, we investigate surge force, heave force, and pitch moment, which are vertical plane hydrodynamics acting on Manta-type unmanned underwater vehicles (UUVs), using a model test and computational fluid dynamics (CFD) simulation. Assessing the maneuvering hydrodynamic characteristic of an underwater glider in the initial design stage is crucial. Although a model test is the best approach for obtaining the maneuvering hydrodynamic derivatives for underwater vehicles, numerical methods, such as Reynolds averaged Navier–Stokes (RANS) equations, have been used owing to their efficiency in terms of time and cost. Therefore, we conducted an RANS-based CFD calculation and a model test for Manta-type UUVs. In addition, we conducted a validation study through a comparison with a model test conducted at a circular water channel (CWC) in Korea Maritime & Ocean University Furthermore, two RANS solvers (Star-CCM+ and OpenFOAM) were used and compared. Finally, the maneuvering hydrodynamic forces obtained from the static drift and resistance tests for a Manta-type UUV were presented.*

## 1. Introduction

In the past 20 years in South Korea, underwater vehicles—which can be used for various purposes, such as marine exploration and military use—have been actively researched (Bae and Sohn, 2009; Ko et al., 2013). Despite the emerging utilization of aquatic bodies, not much research data related to their varied linearities have been revealed, compared to the results published for various surface-piercing vessels.

In general, the estimation of maneuvering performance is an important factor in the initial design stage of surface vehicle development. The maneuvering performance can be predicted using the following two methods: captive model test and free-running model test. The prediction method using the free-running model test shows the closest results to the maneuvering performance of a vehicle; however, it is difficult to build a free-running system and conduct tests. Therefore, the maneuvering performance is mostly predicted by measuring the force and moment acting on the hull, using the captive model test. There is another prediction method, based on sea-trial data that have been researched and accumulated thus far. With the recent development of computer hardware, performance prediction through virtual captive model testing or virtual planar motion mechanism is being actively performed using computational fluid dynamics (CFD) simulation.

Conversely, applying the same method of predicting the performance of a surface vehicle for predicting the maneuvering performance of an underwater vehicle requires watertightness of the model, as the experiment for a captive model test is conducted under the free surface, which results in increased production cost and difficulties in preparing the test apparatus. The free-running model test conducted for an underwater vehicle is more difficult than that conducted for a surface vehicle; moreover, no previously reviewed or disclosed trial run data is available.

For this reason, CFD can be easily used for predicting the maneuvering performance of an underwater vehicle; in fact, this has been extensively researched (Singh et al., 2017; Cheon et al., 2018).

Therefore, this study aims to examine the hydrodynamic force acting on the forward and static drift motions of an underwater vehicle using CFD, based on Reynolds-averaged Navier–Stokes (RANS) equations.

Star-CCM+, a commercial software, and OpenFOAM, an open-

Received 2 March 2020, revised 22 June 2020, accepted 25 June 2020
Corresponding author Sung-Wook Lee: +82-51-410-4303, swlee@kmou.ac.kr

source tool kit, are used as the CFD solvers. In addition, to examine the effectiveness of the CFD analysis results and usefulness of CFD, the obtained results are compared with those obtained using the captive model tests conducted by Bae and Sohn (2009) in a circular water channel (CWC) for the same linear underwater vehicle. Meanwhile, to verify the previously obtained results, retests are conducted using the same unmanned underwater vehicle (UUV) model, to compare and review the final results.

## 2. Experimental and Numerical Analysis Conditions

We conducted a resistance test and static drift test to study the maneuvering hydrodynamic forces acting on a Manta-type UUV, through an experiment and a CFD analysis. Table 1 shows the maneuvering hydrodynamic derivatives obtained from each test.

**Table 1** Hydrodynamic derivatives obtained from each test

| Item | | Maneuvering hydrodynamic derivative |
|---|---|---|
| Resistance test | | $X_{uu}'$ |
| Static drift test | Surge | $X_{uu}'$, $X_{uw}'$, $X_{ww}'$ |
| | Heave | $Z_{uu}'$, $Z_{uw}'$, $Z_{w}'$, $Z_{w\|w\|}'$ |
| | Pitch | $M_{uu}'$, $M_{uw}'$, $M_{w}'$, $M_{w\|w\|}'$ |

### 2.1 Geometric Specification of Manta-type UUV

Among the underwater vehicles, a Manta-type UUV model, which has already been studied, was selected as the target vehicle for this study. Fig. 1 shows the shape of the Manta model, and Table 2 lists its dimensions.

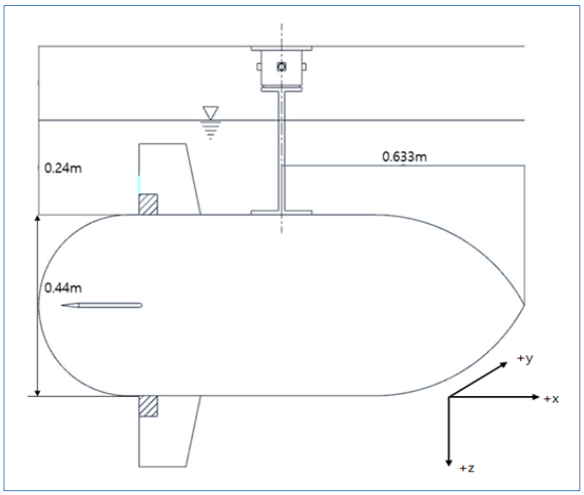


(a) Horizontal plan

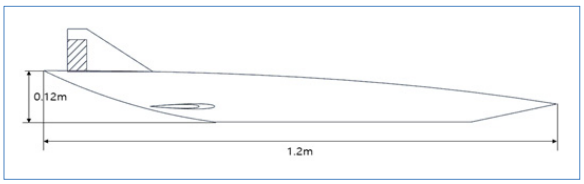


(b) Manta UUV profile

**Fig. 1** Drawings of Manta-type UUV

**Table 2** Principal dimensions of Manta-type UUV

| Manta UUV & Model principal | | |
|---|---|---|
| Item | Manta | model |
| Length (m) | 12 | 1.2 |
| Breadth (m) | 4.4 | 0.44 |
| Height (m) | 1.2 | 0.12 |
| Centroid (m) (from nose) | 6.333 | 0.6333 |
| Scale ratio | 0.1 | |

### 2.2 Experimental Conditions

The experiment was conducted in a CWC at Korea Maritime and Ocean University, whose specifications are listed in Table 3. As shown in Fig. 2, the hydrodynamic force acting on the Manta-type UUV was measured for 3 min, twice for each experimental condition, using a three-component force transducer with capacities of ±50 N for force ($F_x$, $F_y$) and ±10 N-m for moment ($M_z$).

**Table 3** CWC details

| CWC details | |
|---|---|
| Type | 2 Impeller vertical type (OV2-60B) |
| Dimensions whole body | L : 12.5 m, W : 2.2 m, H : 5.2 m |
| Dimensions measuring section | L : 5 m, W : 1.8 m, H : 1.2 m |
| Water capacity | 60 t |
| Performance | Max. 2.0 m/s |
| Driving system Impeller motor | AC22KWX2SETS |
| Date MFD | JULY 1990 |


**Fig. 2** Three-component force transducer

#### 2.2.1 Resistance test

In this study, the same velocity as that used for the Manta UUV in the model test conducted by Bae and Sohn (2009) was selected using the Reynolds number, whose details are presented in Table 4. In the subsequent results, $Vm$ denotes the velocity used in each test and the CFD analysis.

**Table 4** Conditions for resistance test

| Velocity (m/s) | 0.32, 0.4, 0.5, 0.6 |
|---|---|

2.2.2 Static drift test

A static drift test was conducted to experimentally measure the surge force, heave force, and pitch moment, which are the vertical hydrodynamic damping forces acting on the model. Owing to the limited capacity of the three-component force transducer, the elevation test was conducted only at 0.32 and 0.4 m/s under the conditions listed in Table 5. As shown in Fig. 3, the velocity was measured at measurement points 15 cm away from the center, left, and right of the hull, to confirm if the velocity in the circular water tank was uniformly distributed during the static drift test.

**Table 5** Conditions for static drift test

| Velocity (m/s) | Drift angle (°) |
|---|---|
| 0.32 | ±0, 3, 6, 9, 12, 15, 20 |
| 0.4 | ±0, 5, 10, 15, 20 |

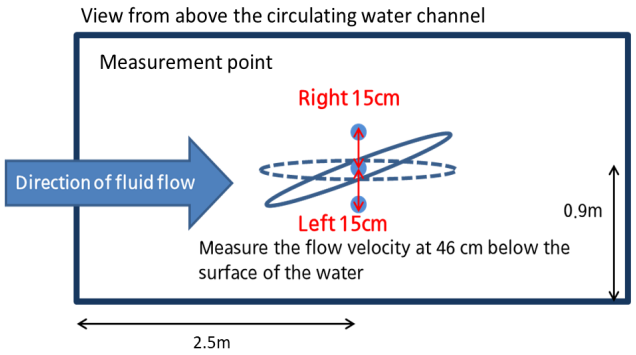


**Fig. 3** Velocity calibration measuring point

## 2.3 Numerical Analysis Conditions

The CFD solver mainly used in this study was Star-CCM+, which performed numerical analysis to understand the hydrodynamic forces and phenomena acting on the underwater vehicle, as mentioned in the Introduction. To confirm the reliability of the numerical analysis result, according to the difference between the Star-CCM+ solver and interFOAM, which is the transient-flow solver of OpenFOAM, a numerical analysis was conducted using the same grid mesh and numerical technique as those used for OpenFOAM under certain conditions in Table 7.

The size of the computational domain used for the CFD analysis was set similarly to the measuring points set for the CWC, as shown in Fig. 4. The volume-of-fluid technique was used for the governing equation of the multiphase flow, and $k-\omega$ was used as the turbulence model. Table 6 shows the details of the numerical techniques applied to the analysis.

As shown In the table, the analysis time was set to 50 s to allow the forces acting on the vehicle to converge sufficiently. Fig. 5 presents the results obtained for the time-step sensitivity test, indicating the

**Table 6** Conditions for CFD (Star-CCM+ & OpenFOAM)

| Item | Applied techniques |
|---|---|
| Space | Three dimensional |
| Time | Implicit unsteady<br>Solve time: 50.0 s \| Time step: 0.01 s \| Iteration: 5 |
| Courant No. | 0.04096 ~ 0.0768 |
| Material | Eulerian multiphase ~ Volume of fluid (VOF) |
| Viscous | Turbulent - $k-\omega$ |
| Boundary condition | (1) Hull: Wall<br>(2) Bottom: Wall<br>(3) Inlet, Side, Top: Velocity inlet<br>(4) Outlet: Pressure outlet<br>Damping zone (0.2 m) from (3), (4) |
| Number of cell | Approximately 2.33 million |
| y+ | Min.: 0.058, Average: 0.925, Max.: 40.394 |

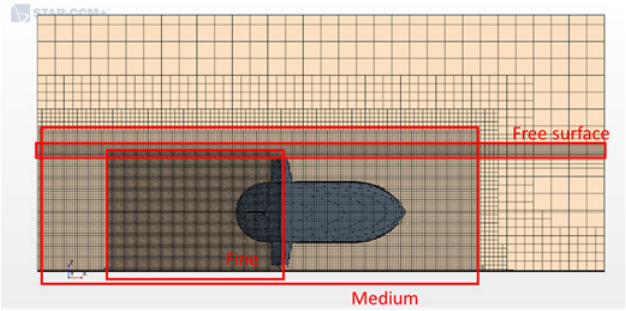


(a) Refinement grid mesh in CFD

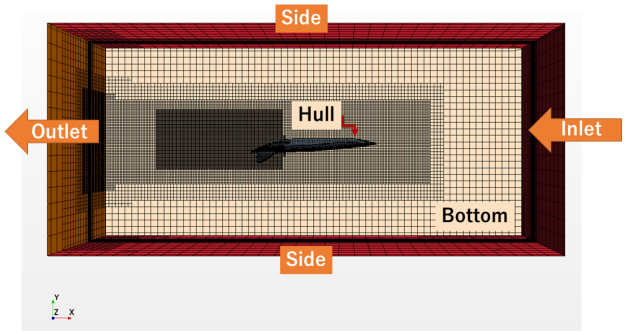


(b) Set boundary condition in CFD

**Fig. 4** Grid system in CFD

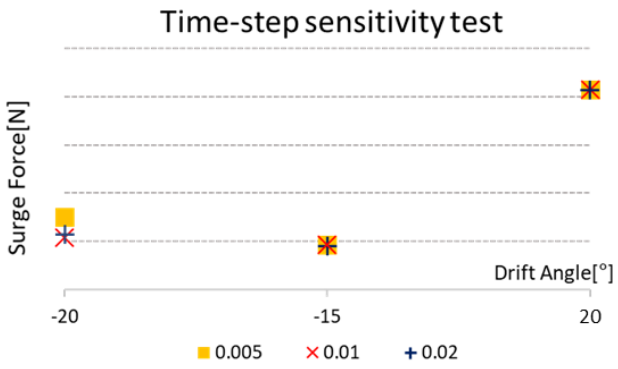


**Fig. 5** Results obtained for time-step sensitivity test

surge force at a specific drift angle. According to the results, there were slight differences in the analysis results at a drift angle of −20°. However, there was no difficulty in setting the time step to 0.01 s, considering the efficiency of the calculation. When assuming the computational domain to be a CWC, there was no significant difference from the results obtained with the boundary conditions set to "Wall" for the side parts, referred to as the side walls. Therefore, for convenience of calculation, the velocity inlet boundary conditions, assuming far-field boundary conditions, were used.

## 3. Comparison of Experimental and Numerical Results

### 3.1 Comparison of Resistance Test Results

Fig. 6 shows the experimental and CFD analysis results obtained for the resistance at different velocities. Here, the vertical axis indicates the resistance coefficient ($X'_{uu}$), which is a dimensionless value of the measured resistance of $0.5\rho L^2 U^2$ (where $\rho$: fluid density, $L$: length of the Manta-type UUV, and $U$: fluid velocity).

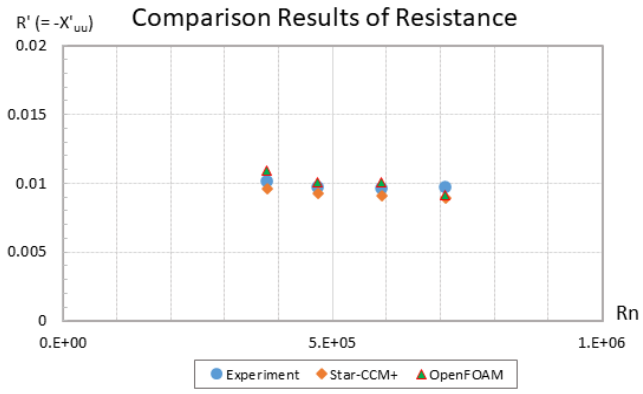


**Fig. 6** Comparison of results obtained for resistance acting on Manta-type UUV at different velocities

First, the calculation results obtained for Star-CCM+ indicated smaller resistance values than those indicated by the model test results, while those obtained for OpenFOAM had larger values, except for 0.6 m/s. This suggests that the $k-\omega$ SST turbulence model of OpenFOAM used in this study tends to be estimated with a smaller force as the velocity increases, which needs to be studied further. Considering that this study aims to show the usefulness of CFD analysis in the motion of underwater vehicles, rather than its advancement, the obtained result is reliable.

### 3.2 Comparison of Static Drift Test Analysis

As described above, the CFD solver mainly used in this study was Star-CCM+ and a numerical analysis was performed using OpenFOAM under the calculation conditions listed in Table 7. For reference, all CFD results presented in 3.2.1−3.2.3 were analyzed prior to performing the model test, which was used as a reference to verify the CFD analysis results.

In addition, the force and moment were non-dimensionalized as $0.5\rho L^2 U^2$ and $0.5\rho L^2 U^2$, respectively, to review the results.

**Table 7** Static drift test and CFD calculation conditions

| Velocity | Experiment | CFD (Star-CCM+) | CFD (OpenFOAM) |
|---|---|---|---|
| (m/s) | (°) | (°) | (°) |
| 0.32 | ±0, 3, 6, 9, 12, 15, 20 | ±0, 3, 9, 15, 20 | N/A |
| 0.4 | ±0, 5, 10, 15, 20 | ±0, 5, 10, 15, 20 | ±0, 5, 10 |

#### 3.2.1 Surge force

Figs. 7 and 8 show the dimensionless results obtained for the model test and CFD calculation for the surge force (force acting on the model vehicle in the straight direction) according to the change in the drift angle of the Manta-type UUV at 0.32 and 0.4 m/s velocities, respectively. These velocities result from the curve fitting conducted using the least-squares method and Eq. (1). The relevant hydrodynamic derivatives obtained from the results are shown in Tables 8 and 9.

As shown in Fig. 8, the surge force was temporarily reduced at a drift angle of −5° in the model test, whereas such phenomenon was not observed in CFD. It is believed that the flow at the small negative drift angle affected the overall surge force due to the change in the surge force acting on the vertical wing of the underwater vehicle. This change may have been detected in the model test, but not in the CFD.

This is considered to be a limitation of the CFD analysis conducted using the RANS equation, and for the purpose of this study, the analysis for a more specific cause identification has not been conducted. Overall, in Fig. 8, the experimental and CFD results tend to be similar, except at the drift angle of −5°, as described above.

$$X' = X_{uu}{}'u'^2 + X_{uw}{}'u'w' + X_{ww}{}'w'^2 \quad (1)$$

A detailed analysis of Figs. 7 and 8 shows that as the drift angle increases in the positive (+) direction, the surge force decreases; in

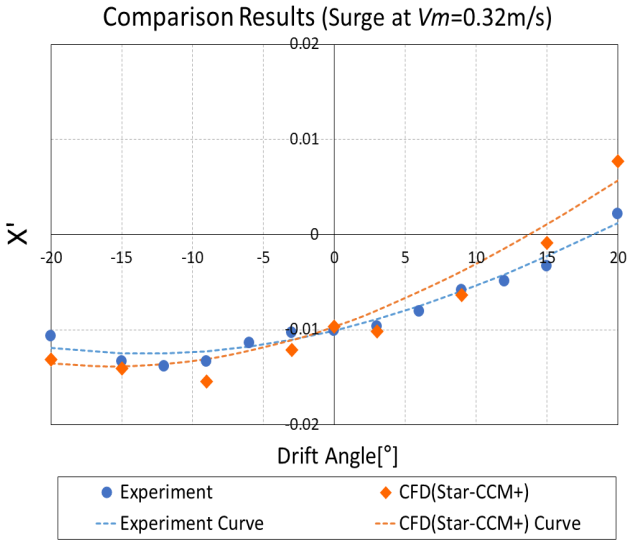


**Fig. 7** Comparison of surge force acting on Manta-type UUV between the experiment and CFD calculation at $Vm$ = 0.32 m/s

**Table 8** Comparison of hydrodynamic derivatives obtained from the surge force acting on Manta-type UUV between the experiment and CFD calculation at $Vm$ = 0.32 m/s

| Hydrodynamic derivatives | Experiment | CFD (Star-CCM+) |
|---|---|---|
| $X_{uu}'$ | −0.0101 | −0.0096 |
| $X_{uw}'$ | 0.0204 | 0.0299 |
| $X_{ww}'$ | 0.0305 | 0.0394 |

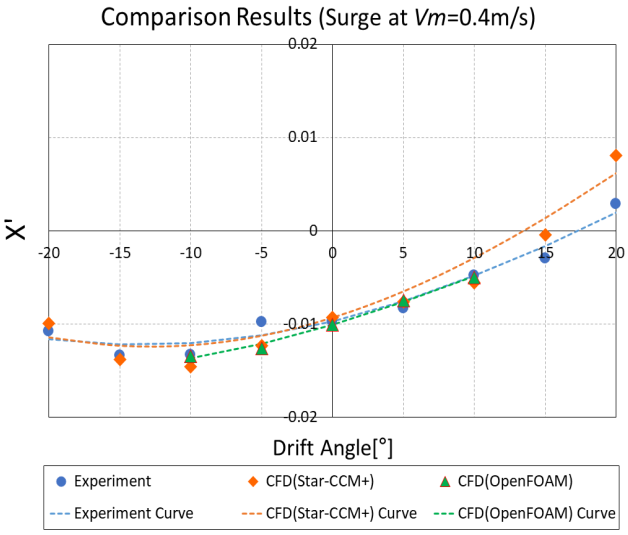


**Fig. 8** Comparison of surge force acting on Manta-type UUV between the experiment and CFD calculation at $Vm$ = 0.4 m/s

**Table 9** Comparison of hydrodynamic derivatives obtained from the surge force acting on Manta-type UUV between the experiment and CFD calculation at $Vm$ = 0.4 m/s

| Hydrodynamic derivatives | Experiment | CFD (Star-CCM+) | CFD (OpenFOAM) |
|---|---|---|---|
| $X_{uu}'$ | −0.0097 | −0.0093 | −0.0101 |
| $X_{uw}'$ | 0.0211 | 0.0273 | 0.0250 |
| $X_{ww}'$ | 0.0319 | 0.0478 | 0.0157 |

contrast, when it increases in the negative (−) direction, the surge force increases and then decreases.

An analysis of the maneuvering hydrodynamic derivatives, obtained from the experimental and CFD calculation results listed in Tables 8 and 9, indicates that although the hydrodynamic derivatives obtained from the Star-CCM+ calculation results slightly differ from those obtained from the experimental results, they are still quite similar. This indicates that there are some quantitative differences because the physical quantity of the surge force itself has a small value, but they are in good agreement when viewed qualitatively. As the maneuvering hydrodynamic derivatives obtained from the OpenFOAM results listed in Table 9 are calculated only under some conditions, the result for $X_{ww}'$ is significantly different from the experimental and Star-CCM+ results, but those for $X_{uu}'$ and $X_{uw}'$ are similar, indicating that the results are in good agreement.

An the analysis of the tendency of the surge force according to the drift angle, conducted only using the model test results, indicated that when the drift angle increased in the positive direction in Fig. 10(b), a counter-current was generated in the back due to the sharply bent shape of part ③ and a force in the opposite direction to the surge force was applied. Similarly, when the drift angle increased in the negative direction, the force in the opposite direction to the surge force acted at a diagonal angle as separation occurred near the vertical wing of part ④.

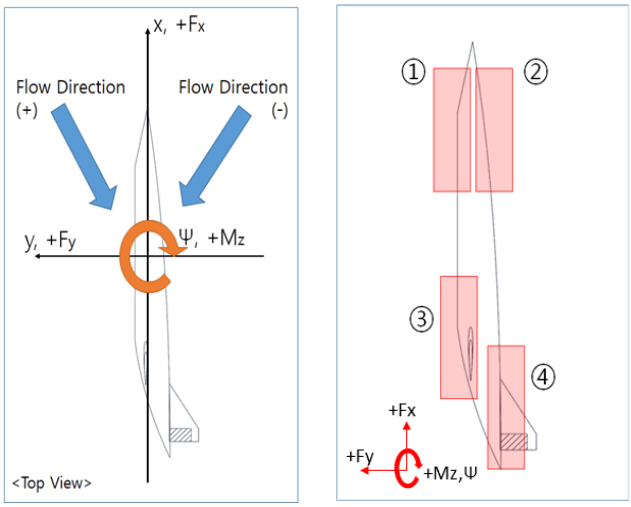


(a) Coordinate system (b) Model features

**Fig. 10** Coordinate system of static drift test and UUV model features

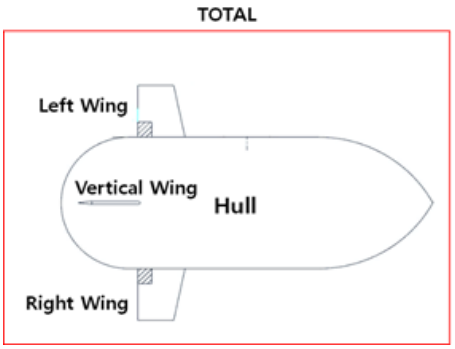


**Fig. 11** Components of Manta-type UUV

**Table 10** Comparison of static drift test surge force acting on Manta-type UUV's each component at $Vm$ = 0.32 m/s

| Component | $Fx$ (N) ($\Psi$ = 20°) | $Fx$ (N) ($\Psi$ = −20°) |
|---|---|---|
| Hull | 0.780 | −0.783 |
| Left wing | −0.050 | −0.041 |
| Right wing | −0.048 | −0.029 |
| Vertical wing | −0.114 | −0.118 |
| Total | 0.568 | −0.973 |

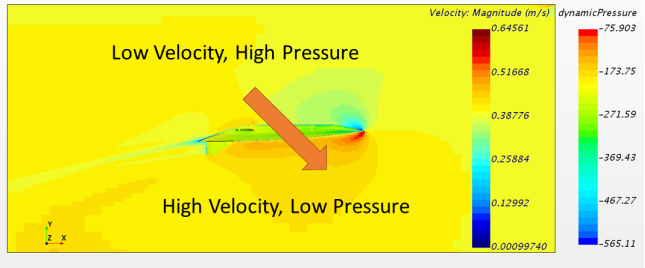


(a) Top view in CFD ( $Vm$ = 0.32 m/s, $\Psi$ = 20°)

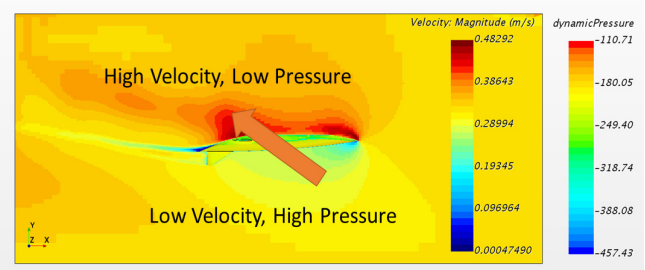


(b) Top view in CFD ( $Vm$ = 0.32 m/s, $\Psi$ = -20°)

**Fig. 12** Flow field of $\Psi$ = 20° & -20° in CFD

To understand the exact trend when calculating using CFD, the Manta-type UUV was divided into the hull and wing parts, as shown in Fig. 11, to examine the hydrodynamic forces acting on each part. Table 10 shows the numerical values for the calculation results obtained at drift angles of +20° and −20°. Fig. 12 shows the flow field around the hull at drift angles of +20° and −20°, where the colors of the object surface indicate the pressure distribution acting on the hull. As shown in Table 10, the surge force (force acting in the straight direction) acting on the horizontal wings (left and right wings) and vertical wing is similar regardless of the drift angle. However, the surge force (force acting in the straight direction) acting on the hull shows a significant difference. At +20°, a faster flow apparently occurs at the bow side, and a force, such as thrust, is generated through the pressure difference, as shown in Fig. 12(a); at −20°, the opposite phenomenon occurs, increasing the resistance as shown in Fig. 12(b). However, as shown in the comparison of the two flow field plots in Fig. 12, because a more complex flow phenomenon occurs and the force in the opposite direction of the surge force acts on the UUV due the counter-current at a drift angle of −20°, the resistance tends to decrease when the drift angle increases in the negative direction.

Due to the limitations of the experimental facility, the experiment was conducted with the horizontal wings of the UUV placed near the free surface and bottom, and the CFD calculation was conducted in the same computational domain as that of the experiment. Table 10 shows almost the same results for the surge forces acting on the left wing close to the free water surface and the right wing close to the bottom, indicating that the effect of the free surface on the UUV is rather insufficient.

3.2.2 Heave force

Figs. 13 and 14 show the dimensionless results of the model test and CFD calculation for the heave force (force acting on the model vehicle in the transverse direction) according to the change in the drift angle of the Manta-type UUV at velocities of 0.32 and 0.4 m/s, respectively. These velocities are the curve fitting results obtained using the least-squares method and Eq. (2). The relevant maneuvering hydrodynamic derivatives obtained from the results are shown in Tables 11 and 12.

$$Z' = Z_{uu}{}'u'^2 + Z_{uw}{}'u'w' + Z_{ww}{}'w'^2 + Z_{w|w|}{}'w'^3 \quad (2)$$

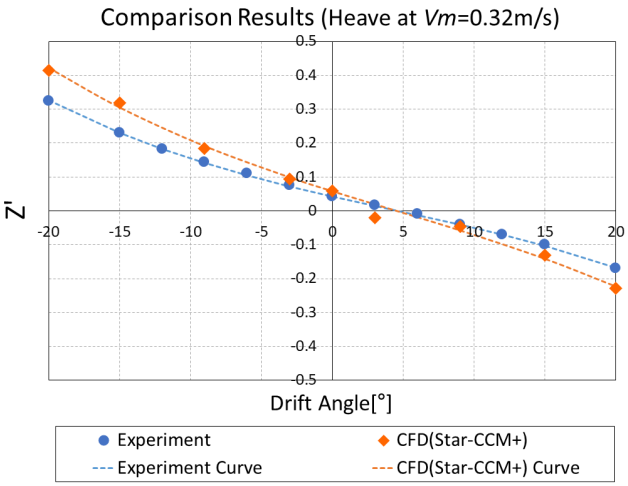


**Fig. 13** Comparison of heave force acting on Manta-type UUV at $Vm$ = 0.32 m/s

**Table 11** Comparison of hydrodynamic derivatives obtained from the heave force acting on Manta-type UUV between the experiment and CFD calculation at $Vm$ = 0.32 m/s

| Hydrodynamic derivatives | Experiment | CFD (Star-CCM+) |
|---|---|---|
| $Z_{uu}{}'$ | 0.0430 | 0.0584 |
| $Z_{uw}{}'$ | 0.5417 | 0.7542 |
| $Z_{ww}{}'$ | 0.3509 | 0.4110 |
| $Z_{w\|w\|}{}'$ | 1.8038 | 1.9965 |

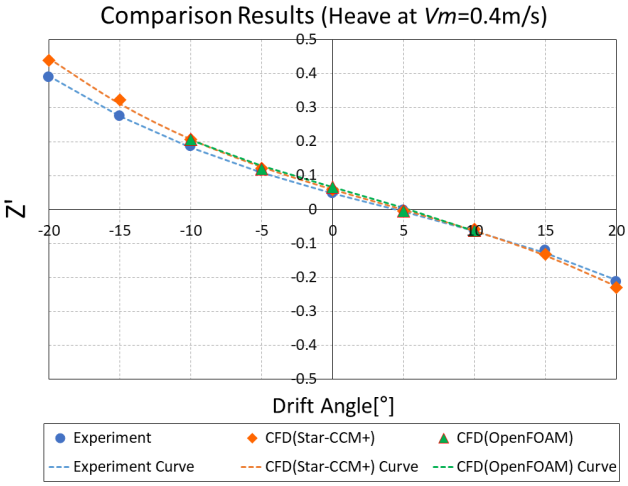


**Fig. 14** Comparison of heave force acting on Manta-type UUV between the experiment and CFD calculation at $Vm$ = 0.4 m/s

**Table 12** Comparison of hydrodynamic derivatives obtained from heave force acting on Manta-type UUV between the experiment and CFD calculation at $Vm$ = 0.4 m/s

| Hydrodynamic derivatives | Experiment | CFD (Star-CCM+) | CFD (OpenFOAM) |
|---|---|---|---|
| $Z_{uu}'$ | 0.0481 | 0.0590 | 0.0667 |
| $Z_{uw}'$ | 0.6429 | 0.7064 | 0.6931 |
| $Z_{ww}'$ | 0.4251 | 0.4899 | 0.1893 |
| $Z_{w\|w\|}'$ | 2.3354 | 2.7201 | 2.9859 |

As shown in Figs. 13 and 14, the heave force occurred at a drift angle of 0°, and was not symmetrical with respect to the positive and negative directions of the drift angle. This is attributable to, based on the model test results alone, the lift caused by the top-bottom asymmetry of the hull of the model vehicle, as shown in Fig. 10(b).

Analyzing the maneuvering hydrodynamic derivatives obtained from the experimental and CFD calculation results shown in Tables 11 and 12, although the hydrodynamic derivatives obtained from the Star-CCM+ calculation results slightly differed from those obtained from the experimental results, they are still quite similar, as in the case of the maneuvering hydrodynamic derivatives obtained for the surge force. Similarly, as the maneuvering hydrodynamic derivatives from the OpenFOAM results shown in Table 12 were calculated only under some conditions, the result for $Z_{ww}'$ was different from the experimental and Star-CCM+ results, while those for the other hydrodynamic derivatives agreed well.

For a detailed examination of the result of the heave force according to the drift angle, as shown in Fig. 11, the vertical force acting on each part of the vehicle was calculated as for the surge force. Table 13 shows the numerical values for the calculation results at drift angles of +20° and −20°. According to the calculation results, disregarding the sign due to the difference in direction, such as the positive or negative direction (that is, analyzing the absolute value of the acting hydrodynamic force), heave forces of similar size acted on the horizontal wings and the hull. However, this result is different from the abovementioned statement that the left-right asymmetry of the heave force generated at a drift angle of 0° results from the lift generated by the top-bottom asymmetry of the hull. In other words, the lift caused by the top-bottom asymmetry of the hull is judged to be the cause of the left-right asymmetry, based on the model test results shown in Figs. 13 and 14. However, the CFD calculation suggests that the direction of the force acting on the vertical wing plays a greater role than the top-bottom asymmetry of the hull, regardless of the direction of the drift angle.

**Table 13** Comparison of static drift test heave force acting on Manta-type UUV's each component at $Vm$ = 0.32 m/s

| Component | $Fy$ (N) ($\Psi$ = 20°) | $Fy$ (N) ($\Psi$ = −20°) |
|---|---|---|
| Hull | −21.490 | 20.597 |
| Left wing | −0.966 | 1.646 |
| Right wing | −1.041 | 1.748 |
| Vertical wing | −6.617 | 6.647 |
| Total | −16.880 | 30.616 |

3.2.3 Pitch moment

Finally, Figs. 15 and 16 show that the pitch moment has an asymmetrical curve as the heave force forms an asymmetrical curve according the drift angle.

Similar to the cases of the surge and heave forces, the dimensionless results of the model test and CFD calculation for the pitch moment are shown, which are the results of curve fitting performed using the least-squares method and Eq. (3). The relevant hydrodynamic derivatives obtained from the results are shown in Tables 14 and 15.

While the results of the calculated hydrodynamic derivatives show a similar tendency to those of the heave force, the result of the third term, $M_{w|w|}'$, shows a huge difference as the value of the pitch moment is much smaller than that of the heave force in terms of the size of the hydrodynamic force. In addition, as the hydrodynamic derivatives obtained from the OpenFOAM results shown in Table 15 are calculated only under some conditions, the result for $M_{ww}'$ is considerably different from the experimental and Star-CCM+ results, while the results for other hydrodynamic derivatives are in good agreement.

$$M' = M_{uu}'u'^2 + M_{uw}'u'w' + M_{ww}'w'^2 + M_{w|w|}'w'^3 \quad (3)$$

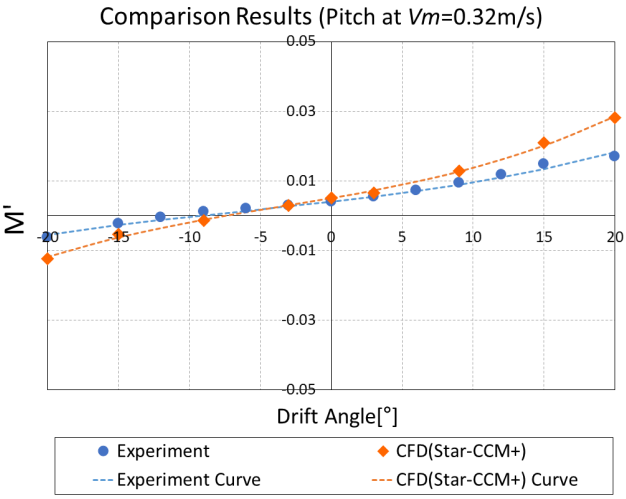


**Fig. 15** Comparison of pitch moment acting on Manta-type UUV between the experiment and CFD calculation at $Vm$ = 0.32 m/s

**Table 14** Comparison of hydrodynamic derivatives obtained from the pitch moment acting on Manta-type UUV between the experiment and CFD calculation at $Vm$ = 0.32 m/s

| Hydrodynamic derivatives | Experiment | CFD (Star-CCM+) |
|---|---|---|
| $M_{uu}'$ | 0.0040 | 0.0051 |
| $M_{uw}'$ | 0.0265 | 0.0404 |
| $M_{ww}'$ | 0.0244 | 0.0331 |
| $M_{w\|w\|}'$ | 0.0837 | 0.1813 |

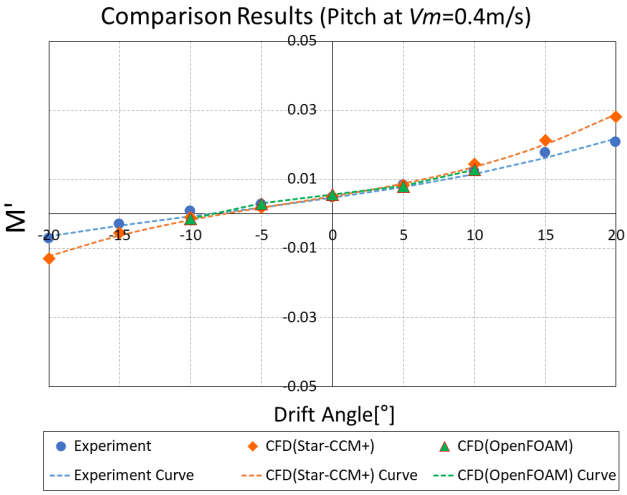


**Fig. 16** Comparison of pitch moment acting on Manta-type UUV between the experiment and CFD calculation at $Vm$ = 0.4 m/s

**Table 15** Comparison of hydrodynamic derivatives obtained from the pitch moment acting on Manta-type UUV between the experiment and CFD calculation at $Vm$ = 0.4 m/s

| Hydrodynamic derivatives | Experiment | CFD (Star-CCM+) | CFD (OpenFOAM) |
|---|---|---|---|
| $M_{uu}'$ | 0.0046 | 0.0051 | 0.0055 |
| $M_{uw}'$ | 0.0333 | 0.0387 | 0.0250 |
| $M_{ww}'$ | 0.0307 | 0.0326 | 0.0091 |
| $M_{w\|w\|}'$ | 0.0857 | 0.2028 | 0.5421 |

## 4. Conclusion

The results of this study—conducted to determine the hydrodynamic forces, such as the surge force, heave force, and pitch moment, which act on a Manta-type UUV in longitudinal motion through model testing and CFD analysis—are described as follows.

(1) The model test and CFD results showed a similar tendency for resistance by velocity.

(2) In the static drift test, as a result of obtaining the hydrodynamic forces from each part of the Manta-type UUV model in CFD, the surge force acting on the hull, excluding the wings, changed depending on the direction of the drift angle, showing an asymmetric tendency. In addition, for the heave force and pitch moment, the same heave force acted on the vertical wing regardless of the direction of the drift angle, and the heave force and pitch moment occurred at a drift angle of 0°.

(3) The model test and CFD analysis were conducted simultaneously, and the study was conducted without knowing the results. As shown in the results, the differences between the results obtained by different CFD solvers were rather insignificant and mutually reliable.

As mentioned in the Introduction, this study provides a good example for the usefulness of CFD in predicting the maneuvering performance in the initial stage of designing underwater vehicles. Nevertheless, as the model test and CFD analysis results showed a slight difference at a diagonal angle under certain conditions, further study is required to increase the accuracy of the CRD analysis. However, using CFD in combination with model testing would be beneficial in identifying the trends in hydrodynamic forces, which are difficult to be judged through model testing alone.

## Acknowledgments

This research is a part of the research project which is funded by the Basic Science Research Program through the National Research Foundation of Korea (NRF) and funded by the Ministry of Education (NRF-2017R1D1A3B03030423).

## References

Ko, S.H., Kim, D.H., & Kim, J.Y. (2013). Implementation and Field Test for Atonomous Nigation for Mnta UUV. Jornal of the Korean Society of Marine Engineering, 37(6), 644-652. https://doi.org/10.5916/jkosme.2013.37.6.644

Bae, J.Y., & Sohn, K.H. (2009). A Sudy on Manoeuvring Motion Characteristics of Manta-type Unmanned Undersea Vehicle. Journal of the Society of Naval Architects of Korea, 46(2), 114-126. https://doi.org/10.3744/SNAK.2009.46.2.114

Cheon, K.H., Park, J.Y., Seok, W.C., & Rhee, S.H. (2018). Prediction of Hyrodynamic Derivatives to Estimate Manoeuvrability of A Submersible Body Using SNUFOAM. Proceedings of Korean Society for Computational Fluids Engineering Conference, 169-170. Retrieved June 2020 from http://www.dbpia.co.kr/pdf/pdfView.do?nodeId=NODE07438390

Singh, Y., Bhattacharyya, S.K., & Idichandy, V.G. (2017). CFD Approach to Modelling, Hydrodynamic Analysis and Motion Characteristics of a Laboratory Underwater Glider with Experimental Results. Journal of Ocean Engineering and Science, 2(2), 90-119. https://doi.org/10.1016/j.joes.2017.03.003

## Author ORCIDs


| Author name | ORCID |
|---|---|
| Lee, Seong-Eun | 0000-0003-1633-2387 |
| Lee, Sung-Wook | 0000-0001-6089-303X |
| Bae, Jung-Young | 0000-0001-7869-5330 |

KSOE
Original Research Article

**Journal of Ocean Engineering and Technology** 34(4), 245-252 August, 2020
https://doi.org/10.26748/KSOE.2020.026

pISSN 1225-0767
eISSN 2287-6715

# Numerical Study on Wave Run-up of a Circular Cylinder with Various Diffraction Parameters and Body Drafts

Ho-Jin Jeong[1], Weoncheol Koo[2] and Sung-Jae Kim[1,3]

[1]*Researcher, Department of Naval Architecture and Ocean Engineering, Inha University, Incheon, Korea*
[2]*Professor, Department of Naval Architecture and Ocean Engineering, Inha University, Incheon, Korea*
[3]*Visiting scholar, Department of Ocean Engineering, Texas A&M University, College Station, Texas, USA*

**KEY WORDS:** Wave run-up, Numerical wave tank, Circular cylinder, Diffraction parameter

**ABSTRACT:** *Wave run-up is an important phenomenon that should be considered in ocean structure design. In this study, the wave run-up of a surface-piercing circular cylinder was calculated in the time domain using the three-dimensional linear and fully nonlinear numerical wave tank (NWT) techniques. The NWT was based on the boundary element method and the mixed Eulerian and Lagrangian method. Stokes second-order waves were applied to evaluate the effect of the nonlinear waves on wave run-up, and an artificial damping zone was adopted to reduce the amount of reflected and re-reflected waves from the sidewall of the NWT. Parametric studies were conducted to determine the effect of wavelength, wave steepness, and the draft of the cylinder on the wave run-up of the cylinder. The maximum wave run-up value occurred at 0°, which was in front of the cylinder, and the minimum value occurred near the circumferential angle of 135°. As the diffraction parameter increased, the wave run-up increased up to 1.7 times the wave height. Furthermore, the wave run-up was 4% higher than the linear wave when the wave steepness was 1/35. In particular, the crest height of the wave run-up increased by 8%.*

## 1. Introduction

Fossil fuel use is steadily increasing due to global energy consumption and economic development. Owing to the depletion of fossil fuels, studies on the development of marine energy resources are being actively conducted (Lee et al., 2013). Accordingly, various marine structures such as wind farms and wave power structures as well as traditional spar or semi-submersible structures have been developed. In recent years, the installation and operation of offshore structures in coastal waters as well as in deep sea and polar conditions have increased. Therefore, studies are being conducted to understand the structural safety and motion performance of marine structures under environmental loads such as extreme waves and winds. Typical research topics include the wave run-up or air-gap due to design wave height, and model tests and numerical analysis techniques are being developed to understand such phenomena (Song and Park, 2017).

Studies on the estimation of wave run-up based on the potential flow theory have been conducted. McCamy and Fuchs (1954) calculated the wave run-up of a bottom fixed single cylinder based on the linear potential theory. Kriebel (1992) conducted a model experiment on a bottom fixed cylinder and confirmed that the wave run-up calculated based on the linear potential theory was lower than the measurement taken in an actual model experiment. Yang and Ertekin (1992) employed a second-order Stokes wave and solitary wave to calculate the external force and wave run-up applied to a cylinder. Lee et al. (2013) estimated wave run-up based on the linear wave theory and compared it to that measured in a model experiment with a two-dimensional wave tank. Li and Liu (2019) proposed an analytical solution by calculating the external force and moment for a surface-piercing cylinder, bottom fixed cylinder, and fully submerged floating cylinder based on the multi-term Galerkin method, and compared the results with the numerical analysis results based on the high-order boundary element method (HOBEM). Oh et al. (2019) conducted a similar study based on the potential flow theory in which they analyzed the hydrodynamic behavior of the body through frequency domain analysis. In addition, a number of numerical studies have been conducted using a three-dimensional numerical wave tank (NWT) based on the potential flow theory. In the three-dimensional NWT, the physical wave tank experiments are numerically simulated through techniques such as the boundary element or finite element

Received 8 May 2020, revised 24 June 2020, accepted 25 June 2020
Corresponding author Weoncheol Koo: +82-32-860-7348, wckoo@inha.ac.kr

methods, which is an analysis technique for nonlinear wave analysis and nonlinear motion analysis. Koo and Kim (2004), Oh et al. (2018), and Wu and Eatock Taylor (1995) have conducted analyses using a two-dimensional nonlinear NWT. In particular, Wu and Eatock Taylor (1995) analyzed the radiation problem with a circular cylinder using the boundary element method and finite element method for a two-dimensional nonlinear NWT. Boo and Kim (1996) solved the diffraction problem using HOBEM for a three-dimensional NWT, and Celebi et al. (1998) analyzed nonlinear environmental loads and wave run-ups of a bottom fixed cylindrical structure and moored floating cylinder in a three-dimensional nonlinear NWT. Bai and Eatock Taylor (2007) solved the diffraction problem of single and concentrated waves by a floating cylinder using the decomposition method for a three-dimensional NWT. Kim and Koo (2019) developed a three-dimensional fully nonlinear potential NWT based on the constant panel method to solve the diffraction, radiation, and vertical motion problems for a wave energy converter.

Various other studies on wave run-up have been conducted. For instance, Li et al. (2012) studied wave run-up between a multi-directional focused wave and cylinder, and Kim et al. (2014) performed numerical analyses of the frequency domain based on the potential flow theory for experiments and a comparison of the characteristics of nonlinear wave run-up around the column of semi-submersible marine structures. In the experiment conducted under light draft and short period conditions, strong nonlinearity was observed at the front of the column, and based on this, it was necessary to consider the nonlinear wave run-up characteristics for semi- submersible marine structures. Recently, with the development of computational fluid dynamics (CFD), many studies have been conducted on wave run-up and wave load. Moon et al. (2018), Liu and Wan (2017), Song and Park (2017), and Fan et al. (2019) conducted a study on the wave run-up of vertical circular cylinders using OpenFOAM. In particular, Fan et al. (2019) studied the effects of wave steepness, relative size of an object, and change in water depth on wave run-up, and confirmed that the size of the wave run-up was significantly influenced by the wave steepness and relative size of the object.

In this study, a wave run-up phenomenon that acts on a cylinder having a circular cross section, which is a typical shape for a marine structure column, was studied using a three dimensional NWT. To this end, the three-dimensional fully nonlinear potential NWT technique developed by Kim and Koo (2019) was used. This technique is an analysis program based on the boundary element and Mixed Eulerian–Lagrangian (MEL) methods, and it is a suitable analysis program for nonlinear wave and wave-floating body interaction analysis. Based on this analysis technique, the wave run-ups were compared at all circumferential angles of the circular cylinder to compare the locations where the maximum and minimum values were formed. In addition, the effect of the diameter ($D$) and draft ($d$) of the cylinder at various wavelengths on the wave run-up was studied by analyzing the incident waves of various periods. The effect of wave nonlinearity on the wave run-up at various wave steepness values was studied by comparing changes in the wave run-up under various wave steepness conditions.

## 2. Problem Formulation

In order to calculate the wave run-up occurring on the cylinder surface, it is assumed that the computational domain is a non-viscous, incompressible, non-rotating potential fluid. Based on this, the velocity potential($\phi$) is introduced, and the governing equation becomes the Laplace equation as in Eq. (1).

To calculate the wave run-up occurring on the surface of a cylinder, it is assumed that the fluid in the computational domain is a non-viscous, incompressible, and non-rotating potential fluid. Therefore, when the velocity potential ($\phi$) is introduced, the governing equation becomes the Laplace equation, which is shown below:

$$\nabla^2\phi = 0 \tag{1}$$

In addition, the Laplace equation can be converted to a boundary integral equation by Green's second identity:

$$\alpha\phi = \iint_S (\phi \frac{\partial G}{\partial n} - G\frac{\partial \phi}{\partial n})ds \tag{2}$$

where $\alpha$ denotes a three-dimensional angle, and $G$ denotes the kernel function. The three-dimensional basic Rankine source expression in 3D is $1/4\pi r$, where $r$ denotes the distance between the source and field points (Kim and Koo, 2019).

Free surface boundary conditions can be divided into kinematic and dynamic conditions, and the linear free surface boundary conditions can be expressed by Eqs. (3)–(4).

$$\frac{\partial \eta}{\partial t} = \frac{\partial \phi}{\partial z} \tag{3}$$

$$\frac{\partial \phi}{\partial t} = -g\eta \tag{4}$$

The semi-Lagrangian approach ($\vec{v} = (0, 0, \delta\eta/\delta t)$) is applied to the nonlinear free surface boundary conditions, which can be expressed by Eqs. (5)–(6), to consider the effects of nonlinear waves.

$$\frac{\delta \eta}{\delta t} = \frac{\partial \phi}{\partial z} - \frac{\partial \phi}{\partial x}\frac{\partial \eta}{\partial x} - \frac{\partial \phi}{\partial y}\frac{\partial \eta}{\partial y} \tag{5}$$

$$\frac{\delta \phi}{\delta t} = -g\eta - \frac{1}{2}|\nabla\phi|^2 + \frac{\delta \eta}{\delta t}\frac{\partial \phi}{\partial z} \tag{6}$$

where $\eta$ denotes the displacement of the free surface. As the boundary condition of the incident wave, a progressive wave is generated by substituting the incident wave component in the left end of the computational domain. The linear wave is applied as the incident wave for linear analysis, and the second-order Stokes wave is applied in the

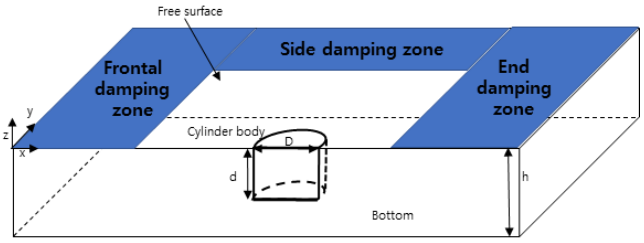


**Fig. 1** Overview of computational domain

nonlinear analysis. Eq. (7) shows the boundary condition of the incident wave according to the second-order Stokes wave that is applied in the analysis of the nonlinear wave. In the case where the incident wave is linear, only the first term of Eq. (7) was applied for the boundary condition.

$$\frac{\partial \phi}{\partial n} = n_x \frac{\partial \phi}{\partial x} = n_x \frac{gAk}{\omega} \frac{\cosh k(z+h)}{\cosh kh} cos(kx - wt) + n_x \frac{3}{8} A^2 \omega(2k) \frac{\cosh 2k(z+h)}{\sinh^4 kh} cos2(kx - \omega t) \quad (7)$$

where $g$ denotes the gravitational acceleration, $A$ denotes the amplitude of the incident wave, $k$ denotes the wave number, and $w$ denotes the wave frequency.

In addition, the boundary surface of the circular cylinder and side wall surface of the numerical wave tank are applied as a rigid interface ($\partial\phi/\partial n = 0$), and the bottom surface is expressed using the image method. Fig. 1 shows the overall computational domain used to determine wave run-up around the cylinder. To create an open sea condition while eliminating the unnecessary reflected waves that may be generated on the free surface, an artificial damping zone is applied in the frontal, side, and end damping zones, and the length of each damping zone is set to one wavelength ($1\lambda$). Moreover, the analysis domain is represented by x-axis symmetry to shorten the analysis time by reducing the number of computational elements. The least square technique is employed for reconstructing the gradient for spatial differentiation, and the inverse distance weighting (IDW) method is employed for interpolation of the nodes. Further details can be found in Kim and Koo (2019).

## 3. Numerical Analysis Model and Results

### 3.1 Numerical Analysis Model and Analysis Conditions

In this study, numerical analysis was performed on a surface-piercing cylinder protruding from a free surface. Fig. 1 shows an overview of the computational domain. Fig. 2 shows the positions of the wave gauges for measuring the wave run-up on the free surface. Each wave gauge was placed at an interval of 22.5°. Table 1 shows the dimensions and specifications of the numerical analysis models. As shown in Table 1, the analysis was performed by increasing the draft ($d$) from 1.5 m to 9 m while maintaining the diameter ($D$) at 3 m. Fig. 3 shows the appearance of the panel (mesh) in the numerical analysis model. The number of elements in the numerical analysis model is 250

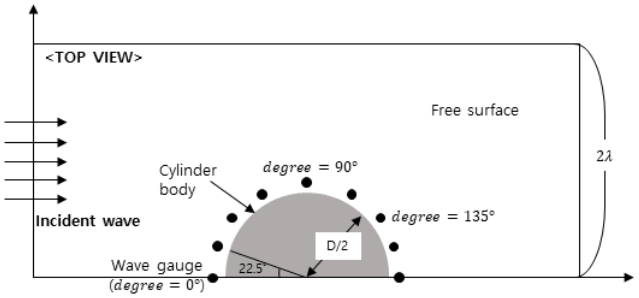


**Fig. 2** Top view of the computational domain

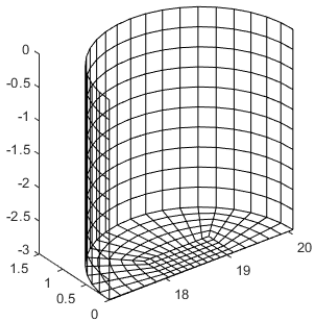


**Fig. 3** Meshes of the circular vertical cylinder

**Table 1** Principal dimensions of the cylinder models

| | Model 1 | Model 2 | Model 3 | Model 4 | Model 5 |
|---|---|---|---|---|---|
| Diameter, $D$ (m) | 3 | 3 | 3 | 3 | 3 |
| draft, $d$ (m) | 1.5 | 3 | 4.5 | 6 | 9 |
| $d/D$ | 0.5 | 1.0 | 1.5 | 2.0 | 3.0 |

**Table 2** Incident wave conditions

| Method | Case No. | Wave period, $T$ (s) | Wave length, $\lambda$ (m) | $D/\lambda$ | Wave height, $H$ (m) |
|---|---|---|---|---|---|
| Linear simulation | 1 | 2.1 | 6.88 | 0.4360 | 0.3 |
| | 2 | 2.3 | 8.26 | 0.3634 | |
| | 3 | 2.5 | 11.38 | 0.3075 | |
| | 4 | 2.7 | 13.13 | 0.2636 | |
| | 5 | 2.9 | 15.97 | 0.2286 | |
| | 6 | 3.2 | 20.22 | 0.1879 | |
| | 7 | 3.6 | 24.95 | 0.1483 | |
| | 8 | 4.0 | 27.47 | 0.1203 | |
| Nonlinear simulation | 9 | 2.3 | 8.26 | 0.3634 | 0.055 |
| | 10 | | | | 0.083 |
| | 11 | | | | 0.165 |
| | 12 | | | | 0.206 |
| | 13 | | | | 0.236 |

at $d$ = 1.5 m; 350 at $d$= 3 m; 450 at $d$ = 4.5 m; 550 at $d$ = 6 m; and 750 at $d$ = 9 m. Table 2 shows the 13 incident wave conditions that were calculated for linear and nonlinear analyses. First, the effect of the diffraction parameter was examined by changing $D/\lambda$ from a

minimum of 0.1203 to a maximum of 0.4360, and analysis was performed with varying wave steepness from 0.006 to 0.03 under the condition of a specific diffraction parameter. The water depth was fixed at 15 m.

### 3.2 Wave Run-up Analysis Using a Three-dimensional Linear NWT

To verify the wave run-up of the NWT, wave run-ups at various angles of the cylinder were compared with the numerical analysis results of Lee et al. (2013), as shown in Fig. 4. The specifications of the numerical analysis model were $D$ = 16 m, $d$ = 24 m, and $h$ = 60 m. The incident wave height was fixed at 0.3 m, and the wave run-up height ($R$) was calculated by averaging time series results in which the steady state lasted for five cycles after the incident wave reached the cylinder. Fig. 4 shows that the results of the numerical analysis of this study agree well the results of Lee et al. (2013) for all circumferential angles.

Based on the developed NWT, the effects of the diffraction parameter ($D/\lambda$) and cylinder draft ($d$) on the wave run-up were determined. Fig. 5 shows a comparison of the wave run-ups for various diffraction parameters and the representative circumferential angles, which were set to 0°, where wave run-up was at its maximum as shown in Fig. 4; 135°, where wave run-up was at its minimum; and 90°, which was the central point of the cylinder. The draft and the diameter of the cylinder were set to 3 m each. As the diffraction parameter increased, wave run-up decreased when the circumferential angle was 135°, but it gradually increased at 0° and 90°. In particular, at 0°, where the wave run-up reached its maximum value, it converged to approximately 1.7 times the incident wave height as the diffraction parameter increased. An increased diffraction parameter indicates that the incident wavelength is relatively small compared to the cylinder diameter, and a considerable portion of the incident wave is reflected from the front of the cylinder. If total reflection occurs, such as under completely blocked conditions, which could be achieved with a sea wall, a standing wave is generated, and the maximum wave run-up that can be measured is twice the incident wave height.

This study confirmed that wave-run up was at maximum at

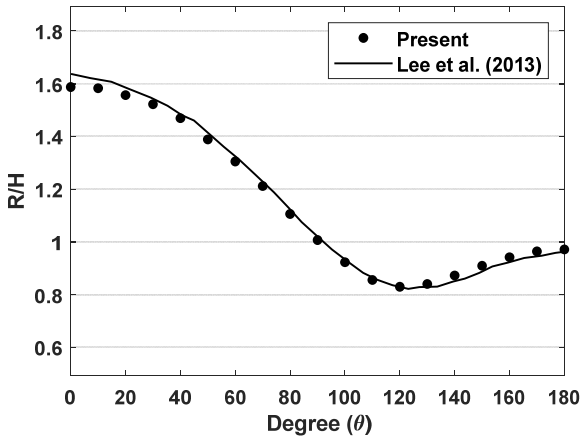


**Fig. 4** Comparison of the wave run-up obtained in the present study and that obtained by Lee et al. (2013) ($T$ = 7.0 s, $h$ = 60 m)

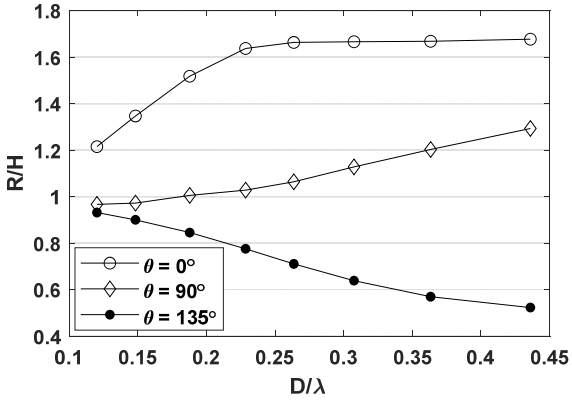


**Fig. 5** Comparison of wave run-ups for various diffraction parameters and measurement points ($d$ = 3 m, $D$ = 3 m)

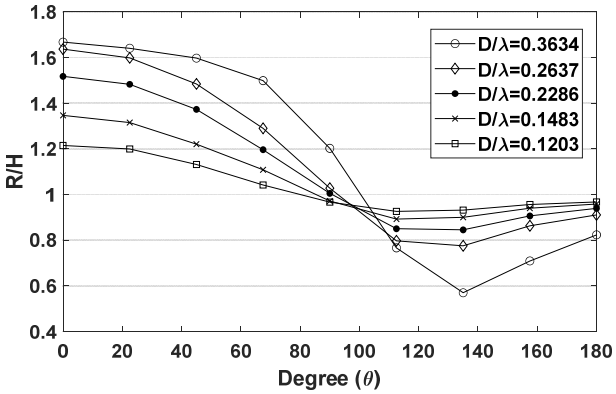


**Fig. 6** Wave run-up at all circumferential angles for various $D/\lambda$ ($d$ = 3 m, $h$ = 15 m)

approximately 1.7 times the incident wave height owing to the shape characteristics of the circular cylinder. If this analysis is applied to an actual design, it can be expected that the free-board of a structure should be at least 1.7 times the incident wave height under the head sea condition, where the incident wave enters (circular angle 0°), to secure the air gap without affecting the topside of a fixed structure. Fig. 6 compares the wave run-up for various angular and diffraction conditions. As the diffraction parameter decreases, the difference in wave run-up decreases, and $R/H$ gradually approaches 1. This is considered to be due to the decreased diffraction effect of the incident wave caused by the cylinder as the diffraction parameter falls below 0.2. Conversely, as the diffraction parameter increases, the difference in wave run-up according to the circumferential angle increases. In particular, when the diffraction parameter is the highest at 0.3634, wave run-up of approximately 1.6 times the wave height occurs around the circumferential angle of 0° to 50°. At a circumferential angle of 90° or greater, the wave run-up is generally reduced, and only approximately 0.6 times the incident wave height at 135°.

Fig. 7 compares the wave run-up at measurement point (a) with a circumferential angle of 0° and measurement point (b) with a circumferential angle of 135° for cylinders with various draft conditions, where the maximum and minimum wave run-ups occur, respectively. As shown in Fig. 7(a), as the draft of the circular cylinder

increases, the wave run-up at the measurement point where the circumferential angle was 0° generally increases. However, this trend decreases as the draft increases, and as the diffraction parameter increases, the increase decreases. When the diffraction parameter is small ($D/\lambda < 0.2$), the maximum wave run-up difference according to the draft is approximately 26%, and when the diffraction parameter is large ($D/\lambda > 0.25$), the maximum difference is approximately 7.4%. When the draft is small compared to the cylinder diameter (0.5 times), the wave run-up is considerably smaller than under other cylinder conditions with a small diffraction parameter. It appears that the incident wave does not affect the cylinder owing to the low draft, and most of it passes through. As shown in Fig. 5, the wave run-up increases and converges to 1.7 as the diffraction parameter increases. Based on this, it can be confirmed that the free-board of the cylindrical structure should be at least 1.7 times the incident wave height regardless of the cylinder draft.

Fig. 7(b) shows the variation in the wave run-up with the ratio of the draft and diameter of the cylinder at the circumferential angle of 135°, where the wave-run up is at its lowest. The wave run-up decreases under all draft conditions as the diffraction parameter increases. Furthermore, when the draft is greater than or equal to the cylinder diameter ($d/D \geq 1$), a similar wave run-up is generated irrespective of the value of the draft.

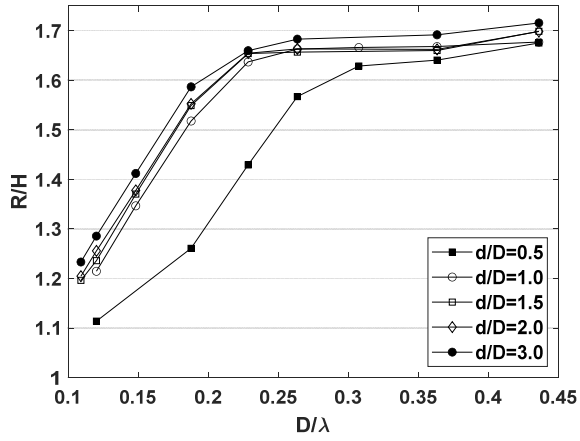


(a) Cylinder circumferential angle = 0°

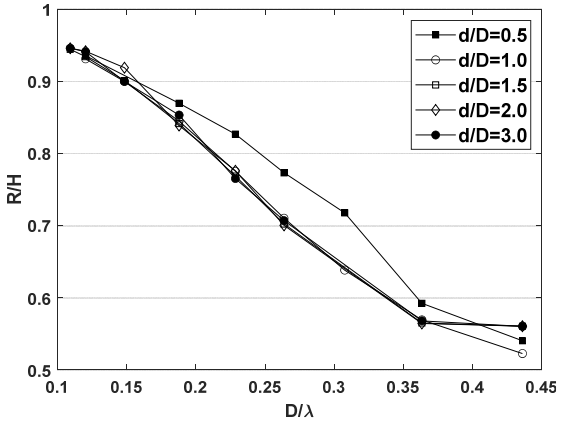


(b) Cylinder circumferential angle = 135°

**Fig. 7** Wave run-up under various $d/D$ conditions for two different circumferential angles (a: angle = 0°and b: angle = 135°)

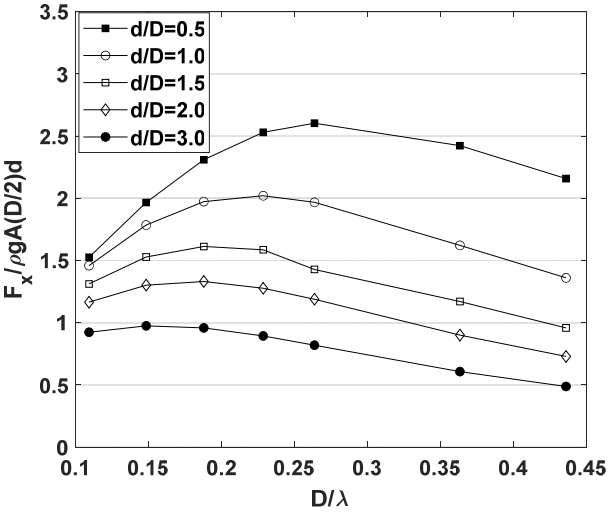


(a) Horizontal force

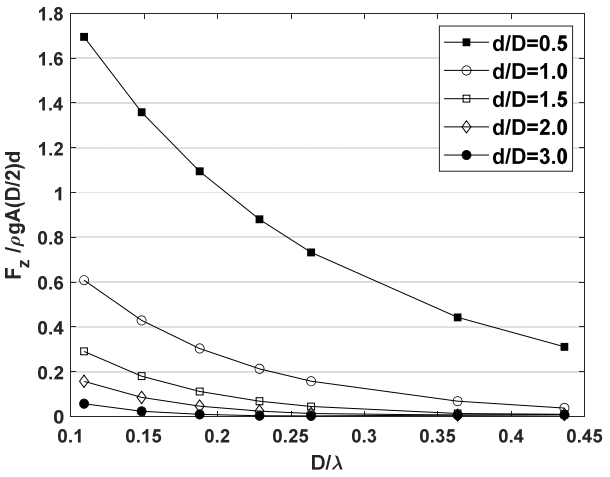


(b) Vertical force

**Fig. 8** Comparison of (a) horizontal forces and (b) vertical forces under various draft conditions

Fig. 8 compares the horizontal and vertical forces of a circular cylinder under various draft conditions. All vertical forces were nondimensionalized with $F/\rho gA(D/2)d$, where $A$ denotes the amplitude of the incident wave. As the cylinder draft increases and the diffraction parameter decreases, the horizontal force generally increases, which is due to the relatively long wavelength of the incident wave increasing the area where the wave energy acts on the cylinder. This relationship between the wavelength and cylinder draft can be observed more prominently by comparing the horizontal force when the diffraction parameter is large. When the diffraction parameter increases, the incident wavelength becomes relatively small, and its effect on the lower surface of the water plane of the circular cylinder is reduced. Because of this, the horizontal force remains almost similar for a deep draft cylinder. In Fig. 8(b), it can be seen that the vertical forces decrease unlike the horizontal forces. The vertical force decreases as the diffraction parameter increases, that is,

as the wavelength is relatively reduced. This is because the effect of the wave on the bottom surface of the cylinder, based on which the vertical force is calculated, is reduced.

### 3.3 Wave Run-up Analysis Using a Full Nonlinear NWT

The variation in the wave run-up of the cylinder because of the nonlinear effect of the incident wave was investigated using a full nonlinear NWT. Unlike linear NWT, which uses linear free surface conditions and incident wave conditions that do not show the variations in the wave run-up due to variations in the wave height, the nonlinear analysis using the nonlinear free water surface boundary conditions can reveal the effect of wave steepness on wave run-up.

Fig. 9 compares the time series data of the wave run-up for the linear and nonlinear analyses for two wave steepness conditions. The wave steepness ($H/\lambda$) values were selected as 1/150 and 1/35 for the linear and relatively large nonlinear effects, respectively. All results used were from the period when $t/T$ was between 6 and 11, during which the time series data reached a steady state. When the wave steepness of a typical nonlinear wave (Stokes wave) condition (1/35) is applied, the crest height of the wave run-up increases by 8% and the trough height decreases by 6% compared to the linear analysis results. When the wave steepness is 1/150, it is almost identical to the time series obtained by the linear NWT, which confirms that the nonlinear effect occurs as the wave steepness increases.

Fig. 10(a) and 10(b) show snapshots of the free water surface area around the cylinder of the NWT for the maximum and minimum diffraction parameters of 0.3634 and 0.1203, respectively, for a wave steepness of 1/35. Fig. 10(a) shows a more pronounced wave run-up. Moreover, this visually confirms that the wave run-up is small in general when the cylinder circumferential angle is 90° or greater.

Figs. 11(a) and 11(b) show the variations in the wave run-up with changes in the draft and wave steepness ($H/\lambda$) of each cylinder at a

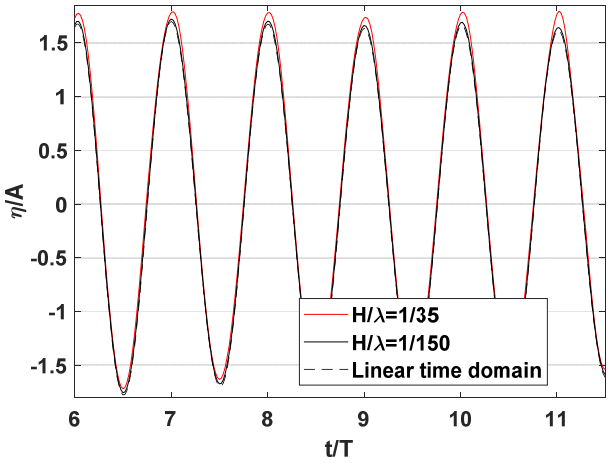


**Fig. 9** Time histories of the wave run-up for different wave steepness values ($d/D$ = 1.0, $D/\lambda = 0.3634$, and angle = 0°)

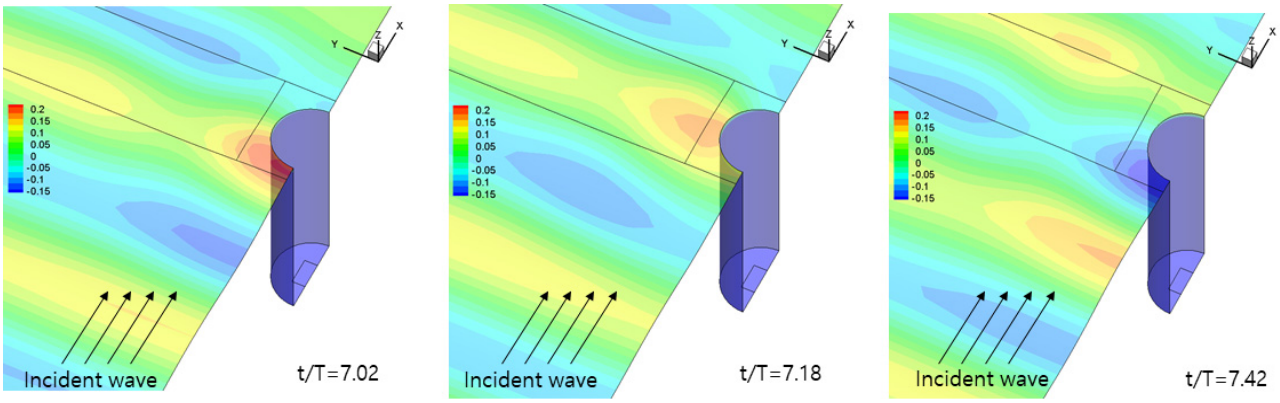


(a) $D/\lambda = 0.3634$

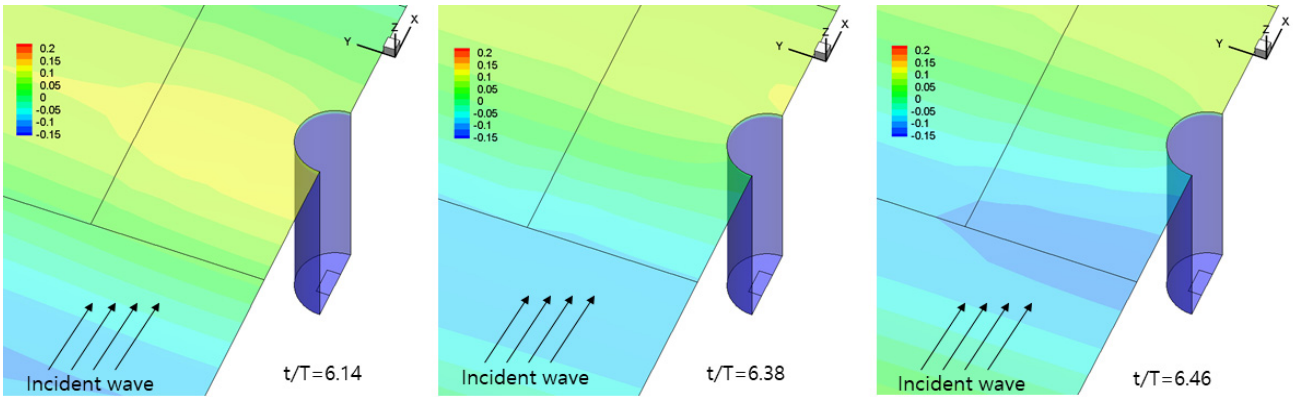


(b) $D/\lambda = 0.1203$

**Fig. 10** Snapshot results of numerical wave tank calculations for two different diffraction parameters ($d$ = 9.0 m, $H/\lambda = 1/35$)

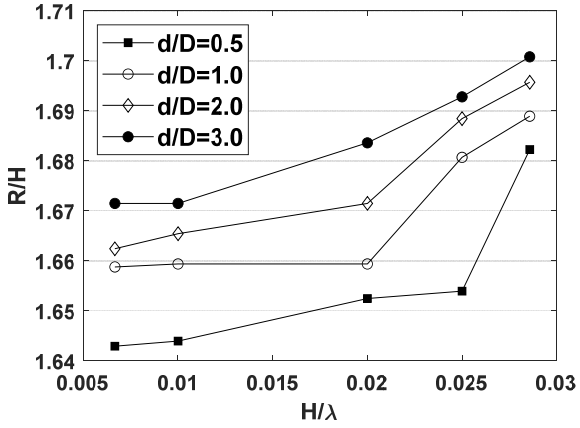


(a) Circumferential angle = 0°

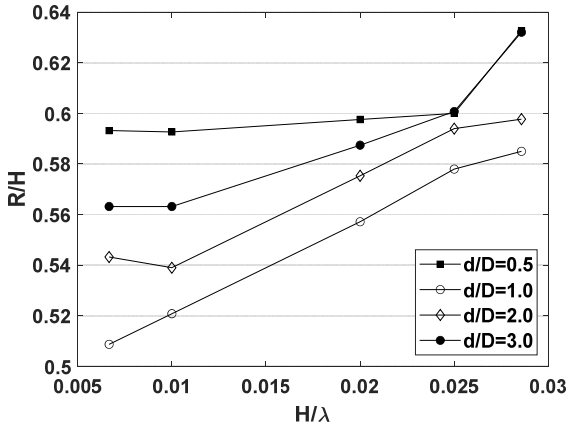


(b) Circumferential angle = 135°

**Fig. 11** Wave run-ups for various wave steepness values: (a) Angle = 0°; (b) Angle = 135°

**Table 3** Frequency components of the wave run-up ($d/D$ =3.0, Angle = 0°, $H/\lambda = 1/35, 1/150$)

| $\omega/\omega_w$ | $\eta/A$ | |
|---|---|---|
| | $H/\lambda$= 1/35 | $H/\lambda$= 1/150 |
| 0 | 0.08336 | 0.01885 |
| 1 | 1.673 | 1.672 |
| 2 | 0.02712 | 0.006119 |
| 3 | 0.003543 | 0.000687 |

cylinder circumferential angle of 0°, where the wave run-up is at its maximum in the linear analysis, and 135°, where the wave run-up is at its minimum. The diffraction parameter ($D/\lambda$) was fixed at 0.3634. The wave run-up increases as the wave steepness increases in all cylinders irrespective of the cylinder draft. For 0°, the relative increase rate of the wave run-up increases when the wave steepness is 0.02 or more. As the linear and nonlinear waves are usually demarcated at the wave steepness of 0.02, it can be understood that a larger crest height occurs in the nonlinear wave section, resulting in a greater wave run-up. At 135°, the measuring point with the minimum wave run-up, a relatively high wave run-up occurs when the ratio of the draft and diameter is the smallest ($d/D$ = 0.5). As the light draft allows the incident wave to easily pass through the lower part of the cylinder, a relatively small wave run-up occurs at 0° (Fig. 7 (a)), and a relatively large run-up occurs at 135°.

To clearly determine the effect of the ratio of the cylinder draft to the radius on changes in wave run-up, the wave run-ups for $d/D$ of 3.0 measured at 0° for the maximum wave steepness of 1/35 and minimum wave steepness of 1/150 were separated for each frequency component (Fast Fourier Transform applied), as shown in Table 3. A comparison of the frequency components for various wave steepness values reveals that the primary wave frequency components of the wave run-up remain the same as the wave run-up values irrespective of the wave steepness. As the wave steepness increases, the mean value and double frequency components of the wave run-up that are proportional to the square of the wave amplitude and triple frequency components of the wave run-up that are proportional to the cube of the wave amplitude increase. The wave run-up increases by 4% when the wave steepness is approximately 1/35. In particular, when the wave steepness is 1/35, the mean value of the wave run-up (zero order frequency components) is 5% of the primary frequency components and 3% for the secondary frequency components.

## 4. Conclusion

In this study, the wave run-up of a circular cylinder was calculated in the time domain using three-dimensional linear and fully nonlinear NWT techniques. The change in the wave run-up was compared and analyzed based on changes in the diffraction parameter ($D/\lambda$), which is the ratio of the diameter of the cylinder to the incident wavelength, the circumferential position (angle) of the cylinder, and the change in cylinder draft. In addition, the effect of wave nonlinearity on the wave run-up under various wave steepness conditions was investigated using a nonlinear NWT.

The three-dimensional NWTs used linear and nonlinear free water surface boundary conditions; furthermore, the least square technique and IDW method were applied for gradient reconstruction and spatial differentiation, respectively.

The wave run-up had a maximum value at 0°, in front of the cylinder where the incident wave reached, and a minimum value occurred at approximately 135°. The wave run-up gradually increased as the diffraction parameter increased, but it converged to approximately 1.7 times the wave height irrespective of the draft when $D/\lambda$ was 0.25 or greater. Based on this, the free-board of a fixed structure composed of a cylindrical lower body should be at least 1.7 times the incident wave height.

The wave run-up, for nonlinear waves with increasing incident wave height increased as the wave steepness increased irrespective of the cylinder draft. The crest height of the wave run-up increased by as much as 8% when the wave steepness was 1/35 compared to when the wave steepness of 1/150. At 0°, where the maximum wave run-up was achieved, the relative increase rate of the wave run-up increased when the wave steepness is 0.02 or greater.

## Acknowledgments

This research was supported by the MOTIE (Ministry of Trade, Industry, and Energy) in Korea, under the Fostering Global Talents for Innovative Growth Program (P0008750) supervised by the Korea Institute for Advancement of Technology (KIAT)

This research was funded and conducted under 「the Competency Development Program for Industry Specialists」 of the Korean Ministry of Trade, Industry and Energy (MOTIE), operated by Korean Institute for Advancement of Technology (KIAT). (No. N0001287, HRD program for Korea-UK Global Engineer Education Program for Offshore Plant)

## References

Bai, W., & Eatock Taylor, R. (2007). Numerical Simulation of Fully Nonlinear Regular and Focused Wave Diffraction around a Vertical Cylinder Using Domain Decomposition. Applied Ocean Research, 29(1-2), 55-71. https://doi.org/10.1016/j.apor.2007.05.005

Boo, S.Y., & Kim, C.H. (1996). Fully Nonlinear Diffraction due to a Vertical Circular Cylinder in a 3-D HOBEM Numerical Wave Tnk. Proceedings of the Sixth International Offshore and Polar Engineering Conference, Los Angeles, CA, USA. https://www.onepetro.org/conference-paper/ISOPE-I-96-163

Celebi, M.S., Kim, M.H., & Beck, R.F. (1998). Fully Nnlinear 3D Nmerical Wave Tank Simulation. Journal of Ship Research, 42(1), 33-45.

Fan, X., Zhang, J.X., & Liu, H. (2019). Numerical Investigation of Run-ups on Cylinder in Steep Regular Wave. China Ocean Engineerng. 33(5), 601-607. https://www.doi.org/10.1007/s13344-019-0058-9

Kim, N.W., Nam, B.W., Cho, Y.S., Sung, H.G., & Hong, S.Y. (2014). Experimental Study of Wave Run-up on Semi-submersible Offshore Structures in Regular Waves. Journal of Ocean Engineering and Technology, 28(1), 6-11. https://doi.org/10.5574/KSOE.2014.28.1.006

Kim, S.J., & Koo, W.C. (2019). Development of a Three-Dimensional Fully Nonlinear Potential Numerical Wave Tank for a Heaving Buoy Wave Energy Converter. Mathematical Problems in Engineering. https://doi.org/10.1155/2019/5163597

Koo, W.C., & Kim, M.H. (2004). Freely Floating-body Simulation by a 2D Fully Nonlienr Numerical Wave Tank. Ocean Engineering, 31, 2011-2046. https://doi.org/10.1016/j.oceaneng.2004.05.003

Kriebel, D.L. (1992). Nonlinear Wave Interaction with a Vertical Circular Cylinder. Part Ⅱ: Wave Run-up. Ocean Engineering, 19(1), 75-99. https://doi.org/10.1016/0029-8018(92)90048-9

Lee, S.B., Han, S.Y., Choi, M.C., Kwon, S.H., Jung, D.W., & Park, J.S. (2013). Study on Wave Run-Up Phenomenon over Vertical Cylinder. Journal of Ocean Engineering and Technology, 27(4), 62-67. https://doi.org/10.5574/KSOE.2013.27.4.062

Li, A.J., & Liu, Y. (2019). New Analytical Solutions to Water Wave Diffraction by Vertical Truncated Cylinders. International Journal of Naval Architecture and Ocean Engineering, 11(2), 952-969. https://doi.org/10.1016/j.ijnaoe.2019.04.006

Li, J., Wang, Z., & Liu, S. (2012). Experimental Study of Interactions between Multi-directional Rocused Wave and Vertical Circular Cylinder, Part Ⅰ: Wave run-up. Coastal Engineering, 64, 151-160. https://doi.org/10.1016/j.coastaleng.2012.02.003

Liu, Z., & Wan, D. (2017). Numerical Simulation of Regular Waves onto a Vertical Circular Cylinder. Proceedings of International Conference on Computational Methods, Guilin, Guangxi, China, 1008-1018.

McCamy, R.C., & Fuchs, R.A. (1954). Wave Force on Piles: A Diffraction Theory. Beach Erosion Board Office of the Chief Engineers, Washington DC, 1-17.

Moon, S.H., Lee, S.W., Paik, K.J., & Kwon, C.S. (2018). A Parametric Study on EOM-based 2D Numerical wave Generation Using OpenFOAM. Journal of Society of Naval Architects of Korea. 55(6). 490-496. https://doi.org/10.3744/SNAK.2018.55.6.490

Oh, S.H., Cho, S.K., Jung, D.H., & Sung, H.G. (2018). Development and Application of Two-Dimensional Numerical Tank Using Desingularized Indirect Boundary Integral Equation Method. Journal of Ocean Engineering and Technology, 32(6), 447-457. https://doi.org/10.26748/KSOE.2018.32.6.447

Oh, S.H., Jung, D.H., Cho, S.K., Nam, B.W., & Sung, H.G. (2019). Frequency Domain Analysis for Hydrodynamic Responses of Floating Structure using Desigularized Indirect Boundary Integral Equation Method. Journal of Society of Naval Architects in Korea, 56(1), 11-22. https://doi.org/10.3744/SNAK.2019.56.1.011

Song, S.J., & Park, S.H. (2017). Analysis on Interaction of Regular Waves and a Circular Column Structure. Journal of the Korean Society for Marine Environment & Energy, 20(2), 63-75. https://doi.org/10.7846/JKOSMEE.2017.20.2.63

Wu, G.X., & Eatock Taylor, R. (1995). Time Stepping Solutions of the Two-dimensional Nonlinear Wave Radiation Problem. Ocean Enginerring, 22(8), 785-798. https://doi.org/10.1016/0029-8018(95)00014-C

Yang, C., & Ertekin, R.C. (1992). Numerical Simulation of Nonlinear Wave Diffraction by a Vertical Cylinder. Journal of Offshore Mechanics and Artic Engineering, 114(1), 36-44. https://doi.org/10.1115/1.2919950

## Author ORCIDs

| Author name | ORCID |
|---|---|
| Jeong, Ho-Jin | 0000-0001-5728-0099 |
| Koo, Weoncheol | 0000-0002-4384-0996 |
| Kim, Sung-Jae | 0000-0001-9582-8983 |

KSOE
Original Research Article

**Journal of Ocean Engineering and Technology** 34(4), 253-262 August, 2020
https://doi.org/10.26748/KSOE.2020.025

pISSN 1225-0767
eISSN 2287-6715

# Evaluation of Structural Design Enhancement and Sensitivity of Automatic Ocean Salt Collector According to Design of Experiments

Chang Yong Song[1], Dong-Jun Lee[2], Jin Sun Lee[3], Eun Mi Kim[4] and Bo-Youp Choi[5]

[1]*Professor, Department of Naval Architecture and Ocean Engineering, Mokpo National University, Jeonnam, Korea*
[2]*MS candidate, Department of Naval Architecture and Ocean Engineering, Mokpo National University, Jeonnam, Korea*
[3]*R&D Director, Jang Sung Tech Co., Ltd., Jeonnam, Korea*
[4]*General manager, Jang Sung Tech Co., Ltd., Jeonnam, Korea*
[5]*Researcher, Research Institute of Medium & Small ShipbuildJeonnam, Jeonnam, Korea*

**KEY WORDS:** Ocean automatic salt collector, Design of experiments, Approximate model, Sensitivity analysis

**ABSTRACT:** *This study provides a comparative analysis of experiments-based enhancements and sensitivity evaluations for the structural design of an automatic ocean salt collector under various load conditions. The sizing variables of the structural members were considered as design factors. The strength and weight performances were selected as output responses. The design of experiments used in the comparative study consisted of the orthogonal array design, Box–Behnken design, and central composite design. The response surface model, one of the metamodels, was applied to the approximate model generation. The design enhancement performance metrics, including numerical costs and weight minimization, according to the design of experiments, were compared from the best design case results. The central composite design method showed the most enhanced design results for the structural design of the automatic ocean salt collector.*

## 1. Introduction

The ocean and fisheries industries are expected to become major providers of food resources in the future, and the development of these enterprises is being strengthened to ensure stable fishery resources worldwide. The market size of the ocean and fisheries equipment industry, the main supplier underpinning the ocean and fisheries industry, is expected to increase from $63.6 billion in 2017 to $89 billion in 2022, with growth particularly expected to increase in the Asia Pacific (Lee et al., 2019). However, the product competitiveness and automation rate of Korean ocean and fisheries equipment is very low, and the ratio of location to market size is only about half, making it considerably reliant on imports.

Salt collectors, a type of ocean and fisheries equipment used to collect salt from ocean salt farms, are in urgent need of development for automation owing to the poor state of salt farming. As shown in Fig. 1, the existing salt collection method in ocean salt farms involves manually unloading crystallized salt into a collection bin on a rail to transfer the salt. To enhance the safety of ocean salt collection and the production per unit of the salt collection and crystallizing pond area, the development of locations for electric automatic ocean salt collectors (AOSC) has recently begun. However, owing to insufficient domestic and foreign design regulations for ocean and fisheries equipment, it is necessary to analyze the sensitivity of the design characteristics according to structural performance conditions to ensure the safety of structural designs of new types of ocean and fisheries equipment such as the AOSC while enhancing design efficiency to minimize weight.

Researchers have conducted several studies on enhancing the safety of ocean equipment designs through sensitivity analysis and optimal design techniques. Park et al. (2011) applied an evolutionary algorithm to minimize the design weight of the support while satisfying strength constraints defined in piping design regulations for pipelines installed in floating production storage and offloading (FPSO) flare system. Song et al. (2011) explored the best design cases to minimize design risk by applying the constraint-feasible moving least squares method, a conservative approximate model for the reliability-based design optimization of FPSO riser adducts. To investigate the safety design of high-pressure quadruple eccentric butterfly valves, Lee and Kim (2014) conducted a design parameter analysis and variance analysis of

Received 8 May 2020, revised 6 June 2020, accepted 8 June 2020
Corresponding author Chang Yong Song: +82-61-450-2732, cysong@mokpo.ac.kr

(a) collecting (b) loading (c) transfer

**Fig. 1** Work process of manual ocean salt collecting production

the seating torque response function. Ji et al. (2015) used a genetic algorithm to realize an optimal placement design considering the stress and dynamic properties of the resilient mount for naval ships. Park et al. (2019) used various design of experiments (DOE) techniques to explore reasonable design cases to solve the issue of resonance in the normal operating range of the main engine of a navigational communication radar mast mounted on large merchant vessels.

To efficiently derive a design improvement case that secures the design safety of the AOSC, the present study explored best design cases by applying various DOE techniques, conducted a sensitivity analysis of major structural members, and compared the results according to DOE characteristics. To evaluate the strength performance in the AOSC's initial design state, a structural analysis model was generated using the finite element method (FEM). The load conditions were calculated considering the AOSC's actual operating conditions and applied to the structural analysis model, and the strength performance was assessed for each load condition. To improve the initial structural design of the AOSC, the influence of the major design members on strength performance was analyzed using DOE, and design improvement cases that satisfy the allowable stress while minimizing weight increase were explored. To derive a design improvement case based on DOE, three DOE techniques—OAD (orthogonal array design), BBD (Box–Behnken design), and CCD (central composite design)—were implemented to analyze the sensitivity results, and the DOE technique most suited for the AOSC's structural design was examined considering the design improvement characteristics and numerical calculation cost. To verify the suitability of the sensitivity analysis results of major structural members and the exploration of DOE-based AOSC improvement cases applied in this study, approximate modeling using the response surface method (RSM) was conducted for each DOE technique, and the RSM design space exploration accuracy generated from each DOE technique was examined. Chapter 2 of this study describes the FEM-based strength performance evaluation of the AOSC's initial structural design. Chapter 3 briefly reviews the theory of DOE, explores best design cases using DOE, conducts a sensitivity evaluation of weight and strength performance, and verifies the suitability of the DOE techniques using an approximate model. Finally, the study is concluded in Chapter 4.

## 2. Structural Analysis of the Initial Design

### 2.1 Calculation of Design Load Conditions

Fig. 2 shows the initial design of the electric AOSC developed to

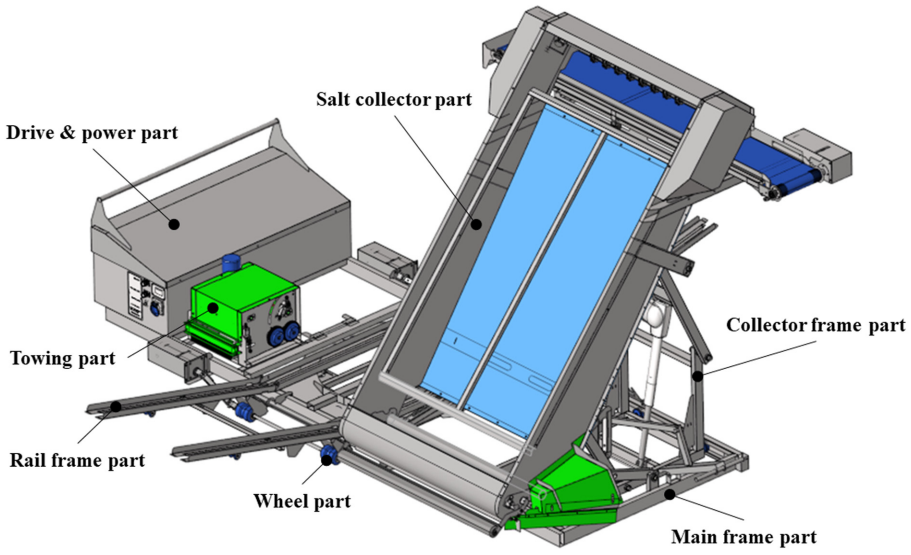


**Fig. 2** Initial design configuration of the AOSC

**Table 1** Principal AOSC dimensions and system specifications

| | Parameter | Particulars |
|---|---|---|
| Dimensions | Length | 3.4 m |
| | Breadth | 3.2 m |
| | Height | 2.1 m |
| System specifications | Max. salt collecting capacity | 0.7 t |
| | Max. towing capacity | 490 N |
| | Operation speed | 6 m/min |
| | Brake | Belt type |

automate the collection of salt in ocean salt farms and enhance ocean salt collection safety as well as production per unit of salt collection crystallizing pond area.

As shown in Fig. 2, a salt collector part and towing part were designed and applied to the AOSC to automate ocean salt collection, and a drive and power part for transferring electric driving power and a rail frame part for transferring the collected salt were installed. To safely support the load generated during operation and mounting of the AOSC's functional components, a collector frame, rail frame, and main frame were applied. Table 1 summarizes principal information on the AOSC.

In terms of the main design load conditions for reviewing the AOSC's structural safety, considering the harshest operating conditions that may arise during salt collection, a maximum loading case, braking case, and operating case under the maximum loading case were selected. Table 2 summarizes the design load conditions for each load case.

As shown in Table 2, the design loads generated in the AOSC for each load case were combined to configure the design load conditions. In the loading case (LC1), the weight of each functional product was applied considering the center of gravity and mounting position. To reflect the entire AOSC's weight, an inertial load was applied considering gravity acceleration, and the maximum salt collecting

**Table 2** Design load cases

| Design loads | Load cases | | |
|---|---|---|---|
| | Loading (LC1) | Operating (LC2) | Braking (LC3) |
| Salt collector weight | √ | √ | √ |
| Drive & power part weight | √ | √ | √ |
| Towing part weight | √ | √ | √ |
| Wheel part weight | √ | √ | √ |
| Inertial load | √ | √ | √ |
| Max. salt collecting capacity | √ | √ | √ |
| Max. towing capacity | - | √ | - |
| Acceleration at operating | - | √ | - |
| Acceleration at braking | - | - | √ |

capacity was applied as distribution pressure on the top of the rail frame in the center of the AOSC. In the operating case (LC2), along with the loading case, the maximum towing capacity and acceleration measured through the operation of prototype equipment manufactured with the initial design were applied in the transport direction. In the braking case (LC3), to consider a sudden braking case along with the loading case, driving acceleration was applied in the opposite direction of the transport direction. Gravity load was applied for the acceleration of LC2 and LC3 so that the gravitational influence of acceleration acted on the entire structure.

### 2.2 FEM-based Structural Analysis

To conduct an FEM-based strength performance evaluation of the AOSC's initial structural design, an FEM (Fig. 3) was generated considering the main structure (main frame, rail frame, and collector frame) and bracket part that can apply the weight and design load of the functional products.

As shown in Fig. 3, the thicknesses of the main frame part, rail frame part, collector frame part, and bracket part are 2.5 mm, 1.5–4.0

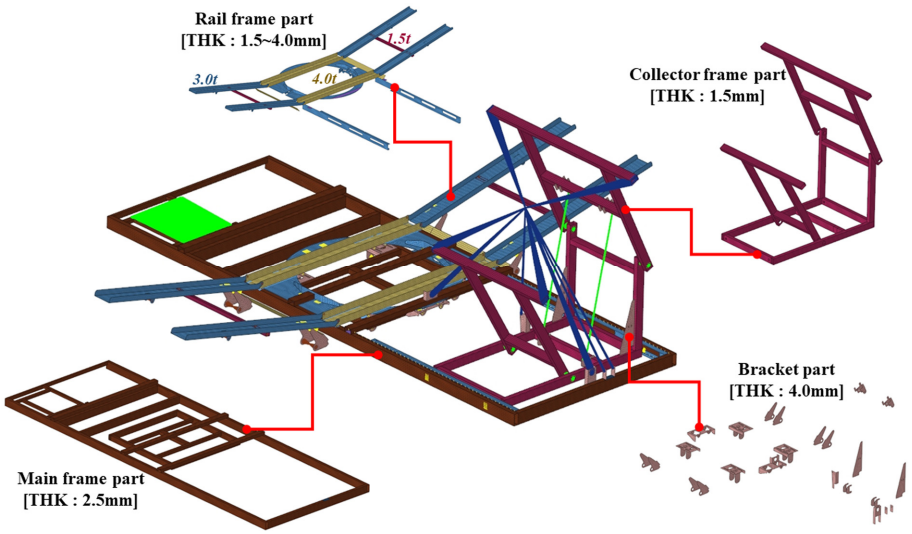


**Fig. 3** Finite element model of the AOSC

**Table 3** FEM model information and material property

| Material property | | | | Model information | |
|---|---|---|---|---|---|
| Density | Elastic modulus | Poisson's ratio | Yield strength | # of elements | # of nodes |
| 8,000 kg/m$^3$ | 193 GPa | 0.29 | 215 MPa | 112,896 | 114,431 |

mm, 1.5 mm, and 4.0 mm, respectively, which were applied in the initial design stage through empirical design. The elements used in the FEM consisted of a shell element for the main structure of the main frame part, rail frame part, collector frame part, and bracket part, and lumped mass elements for the weight of each functional product. Rigid links were used for the connection of each structural member and application part of the functional weight and design load, and the driving direction constraints of the rigid links were defined considering the operating mode. Table 3 summarizes the model information used in the FEM, and material properties of the austenitic stainless steel (SUS304L). The design conditions defined in Table 2 were applied for the load condition used in the structural analysis and for the boundary condition; all degrees of freedom were constrained except the rotation direction of the driving direction for each wheel of the wheel part.

Abaqus/Implicit (Simulia, 2018), a general-purpose finite element analysis program, was used to conduct the structural analysis, and the stress and deformation of the major structural parts were calculated for each design load condition. Table 4 summarizes the structural analysis results of the AOSC's initial design stage, and Fig. 4 shows the overall stress and strain distribution results for the braking case (LC3).

As shown in Table 4, under all design load cases, the stress values of the main frame part and the rail frame part failed to satisfy the material's allowable yield stress. Furthermore, the braking case (LC3) showed the harshest results of all design cases. In all design load cases, the maximum stress occurred in the main frame part, and as shown in Fig. 4, the maximum stress was distributed in the center of the main frame part. The maximum stress occurred locally at the upper center of the main frame and bracket joint, which is likely because the design thickness of the main frame was 2.5 mm in a thin plate, and a gentle shape change design was not applied in the bracket joint. Accordingly, the structural analysis results of the initial design stage demonstrate that design improvements are required to secure the strength and safety of the AOSC's structural design.

**Table 4** Structure analysis results of initial design

| Structure part | Max. von-Mises stress [MPa] / Max. deformation [mm] | | | Safety check | Allowable strength [MPa] |
|---|---|---|---|---|---|
| | LC1 | LC2 | LC3 | | |
| Overall structure | 260.0 / 17.6 | 236.6 / 17.5 | 285.2 / 17.9 | NG | 85% of material yield strength[1) ] : 182.8 |
| Main frame | 260.0 / 12.3 | 236.6 / 12.2 | 285.2 / 12.5 | NG | |
| Rail frame | 185.1 / 11.7 | 180.9 / 11.6 | 191.8 / 12.0 | NG | |
| Collector frame | 45.3 / 17.6 | 66.5 / 17.5 | 52.2 / 17.9 | OK | |
| Bracket | 137.2 / 12.7 | 170.5 / 12.6 | 154.9 / 12.0 | OK | |

[1)] Det Norske Veritas and Germanischer Lloyd (DNV-GL) (2015) Rules and Standards CH.2, Sec.1

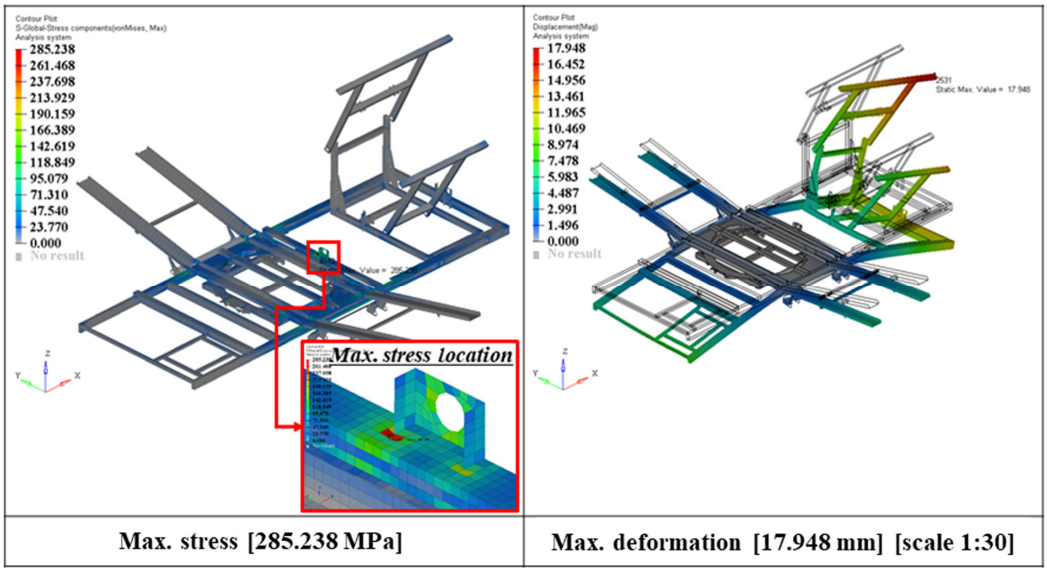


**Fig. 4** LC3 - Overall stress and deformation contours for the initial design

## 3. DOE-based Structural Design Improvement and Sensitivity Evaluation

To improve the initial structural design of the AOSC, the influence of the major design members on strength performance was analyzed using DOE, and design improvement cases that satisfy the allowable stress while minimizing weight gain were explored. To derive a design improvement case based on the DOE method, three DOE techniques (OAD, BBD, and CCD) were implemented to analyze the sensitivity results. The DOE technique most suited for the AOSC's structural design was examined considering the design improvement characteristics and numerical calculation cost. Using the three DOE techniques considered in this study, considering three levels for the design factors, the secondary effects and interaction effects of the design factors can be observed. Unlike random DOE techniques, such as Latin hypercube design, the number of experiments is automatically determined for each DOE method, making it easy to use. However, even for the same design problem, the number of experiments and methods of filling the experiment space differ according to the DOE method, which may result in different design space exploration results. Hence, to utilize the DOE results for approximate optimization or reliability analysis, it is important to select a DOE technique suitable for the design problem. First, the theoretical characteristics of the DOE techniques used in this study are briefly summarized, after which each DOE technique is used to explore best AOSC structural design cases and evaluate the design sensitivity according to strength performance. In addition, to verify the suitability of the sensitivity analysis results of the major structural members and the exploration of DOE-based AOSC improvement cases applied in this study, approximate modeling using RSM was conducted for each DOE technique, and the RSM design space exploration accuracy generated from each DOE technique was examined.

### 3.1 DOE Theory

OAD detects the main effects and interactions between factors for experiments with a large number of factors and excludes information on high-order interaction and interaction between low-influence factors, thereby reducing the number of experiments through an OAT. The OAT has two, three, four, five, and mixed levels, with two and three levels typically used. This study applied OAT with three levels, as in the following equation (Park, 2012).

$$L_{3^m}\left[3^{(3^m-1)/2}\right] \tag{1}$$

where $m$ is an integer of 2 or more, $3^m$ is the experiment size, and $(3^m-1)/2$ is the number of rows in the OAT.

As shown in Fig. 5, the BBD method has a feature by which corner points are not used in the experimental space. This technique is also referred to as spherical, rotational, or approximate rotational quadratic design (Box and Behnken, 1960).

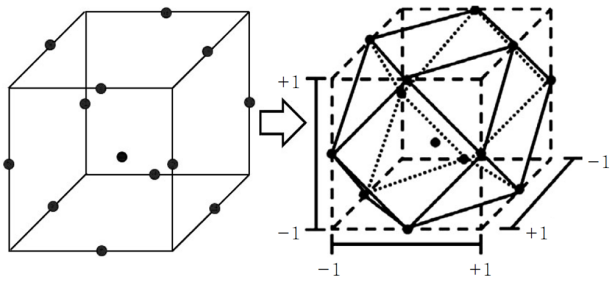


**Fig. 5** Design experimental space of the BBD method (Kim et al., 2015)

As shown in Fig. 5, BBD uses polyhedral edge center points, excluding center points and corner points in the entire experimental space, thus allowing economical DOE. BBD is advantageous for calculating quadratic regression equations and exploring optimal conditions when the factors are quantitative and have three levels. In terms of the number of independent variables $k$, BBD can easily generate orthogonal blocks with a small number of experimental points, through which a quadratic regression equation can be obtained.

CCD adds center points and axial points to $2^k$ factor experiments and detects the curved change in the amount of responses caused by changes in the level of variables (Park, 2012). In CCD, the number of center points becomes at least one, and the number of axial points becomes $2k$. If the number of center points is $n_o$, then the number of CCD experiments $n$ can be defined by the following equation.

$$n = 2^k + 2k + n_0 \tag{2}$$

As in Eq. (2), in the case of $k>2$, the DOE method can be performed with significantly fewer experiments than factorial design, and it is highly advantageous if the experimental cost is high. Moreover, rather than performing DOE again when the regression model estimation must be changed, CCD can perform sequential experiments that add new data points to the center and axis.

### 3.2 Comparison of Best Design Cases and Structural Design Sensitivity According to DOE Characteristics

To conduct the AOSC structural design effect evaluation according to the DOE characteristics, the thickness of the main structural members was set to three levels of the design factors, and the maximum stress and weight for each design load case shown in Tables 2 and 4 were set as the output response. The upper and lower limits of

**Table 5** Design factors and ranges for the AOSC

| Design factors | Lower limit value (mm) | Original design value (mm) | Upper limit value (mm) |
|---|---|---|---|
| DF-#1 | 1.5 | 2.5 | 6.0 |
| DF-#2 | 2.0 | 3.0 | 6.0 |
| DF-#3 | 3.0 | 4.0 | 6.0 |
| DF-#4 | 1.0 | 1.5 | 2.0 |
| DF-#5 | 3.0 | 4.0 | 6.0 |

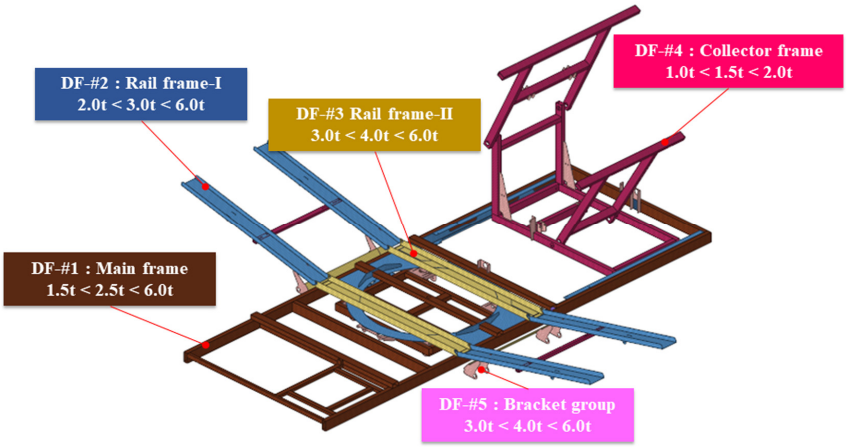


**Fig. 6** Detailed setup for design factors of the AOSC

the design factors were set considering the range within which the AOSC can be manufactured. Table 5 and Fig. 6 show the configuration of AOSC design factors.

The configured design factors and three-level design factor range in Table 5 and Fig. 6 were applied. An experimental matrix with 81 runs was configured for OAD, 41 runs for BBD, and 43 runs for CCD. Tables 6–8 show the results of the response functions calculated via finite element analysis according to changes in design factors in the experimental matrices configured through each DOE technique.

From the results summarized in Tables 6–8, combinations of design

**Table 6** DOE run table for the OAD method

| DOE run # | DF-#1 (mm) | DF-#2 (mm) | DF-#3 (mm) | DF-#4 (mm) | DF-#5 (mm) | LC1-Stress (MPa) | LC2-Stress (MPa) | LC3-Stress (MPa) | Weight (Ton) |
|---|---|---|---|---|---|---|---|---|---|
| 1 | 1.5 | 2.0 | 3.0 | 1.0 | 3.0 | 380.235 | 361.76 | 401.707 | 0.102 |
| 2 | 1.5 | 3.0 | 4.0 | 1.0 | 3.0 | 351.492 | 333.592 | 371.932 | 0.118 |
| 3 | 1.5 | 6.0 | 6.0 | 1.0 | 3.0 | 292.933 | 275.534 | 312.25 | 0.163 |
| ⋮ | ⋮ | ⋮ | ⋮ | ⋮ | ⋮ | ⋮ | ⋮ | ⋮ | ⋮ |
| 79 | 6.0 | 2.0 | 3.0 | 2.0 | 6.0 | 150.947 | 142.658 | 162.610 | 0.246 |
| 80 | 6.0 | 3.0 | 4.0 | 2.0 | 6.0 | 148.831 | 137.775 | 161.666 | 0.262 |
| 81 | 6.0 | 6.0 | 6.0 | 2.0 | 6.0 | 142.700 | 135.897 | 158.452 | 0.307 |

**Table 7** DOE run table for the BBD method

| DOE run # | DF-#1 (mm) | DF-#2 (mm) | DF-#3 (mm) | DF-#4 (mm) | DF-#5 (mm) | LC1-Stress (MPa) | LC2-Stress (MPa) | LC3-Stress (MPa) | Weight (Ton) |
|---|---|---|---|---|---|---|---|---|---|
| 1 | 3.0 | 1.0 | 3.7 | 4.0 | 4.5 | 195.489 | 174.749 | 192.559 | 0.193 |
| 2 | 3.0 | 2.0 | 3.7 | 4.0 | 4.5 | 194.121 | 188.503 | 201.541 | 0.207 |
| 3 | 6.0 | 1.0 | 3.7 | 4.0 | 4.5 | 201.973 | 181.225 | 219.986 | 0.2017 |
| ⋮ | ⋮ | ⋮ | ⋮ | ⋮ | ⋮ | ⋮ | ⋮ | ⋮ | ⋮ |
| 39 | 4.5 | 2.0 | 3.7 | 2.0 | 4.5 | 205.034 | 184.206 | 201.340 | 0.188 |
| 40 | 4.5 | 2.0 | 3.7 | 6.0 | 4.5 | 193.310 | 172.53 | 190.529 | 0.236 |
| 41 | 4.5 | 1.5 | 3.7 | 4.0 | 4.5 | 198.581 | 177.792 | 195.323 | 0.204 |

**Table 8** DOE run table for the CCD method

| DOE run # | DF-#1 (mm) | DF-#2 (mm) | DF-#3 (mm) | DF-#4 (mm) | DF-#5 (mm) | LC1-Stress (MPa) | LC2-Stress (MPa) | LC3-Stress (MPa) | Weight (t) |
|---|---|---|---|---|---|---|---|---|---|
| 1 | 3.0 | 1.0 | 1.5 | 2.0 | 3.0 | 380.235 | 361.760 | 401.707 | 0.102 |
| 2 | 3.0 | 1.0 | 1.5 | 2.0 | 6.0 | 375.933 | 357.500 | 396.333 | 0.115 |
| 3 | 3.0 | 1.0 | 1.5 | 6.0 | 3.0 | 329.727 | 297.065 | 324.220 | 0.150 |
| ⋮ | ⋮ | ⋮ | ⋮ | ⋮ | ⋮ | ⋮ | ⋮ | ⋮ | ⋮ |
| 41 | 4.0 | 1.5 | 2.5 | 6.0 | 4.0 | 244.688 | 219.646 | 258.191 | 0.191 |
| 42 | 4.0 | 1.5 | 2.5 | 3.0 | 3.0 | 268.999 | 242.611 | 286.073 | 0.151 |
| 43 | 4.0 | 1.5 | 2.5 | 3.0 | 6.0 | 258.978 | 235.593 | 283.710 | 0.164 |

**Table 9** Best design cases for design enhancement of the AOSC

| | | Initial design | Best design case from DOE | | |
|---|---|---|---|---|---|
| | | | OAD | BBD | CCD |
| Design factors | DF-#1 | 2.5 mm | 6.0 mm (↑3.5 mm) | 6.0 mm (↑3.5 mm) | 6.0 mm (↑3.5 mm) |
| | DF-#2 | 3.0 mm | 2.0 mm (↓1.0 mm) | 2.0 mm (↓1.0 mm) | 2.0 mm (↓1.0 mm) |
| | DF-#3 | 4.0 mm | 3.0 mm (↓1.0 mm) | 4.5 mm (↑0.5 mm) | 3.0 mm (↓1.0 mm) |
| | DF-#4 | 1.5 mm | 1.0 mm (↓0.5 mm) | 1.5 mm (0.0 mm) | 1.0 mm (↓0.5 mm) |
| | DF-#5 | 4.0 mm | 4.0 mm (0.0 mm) | 4.5 mm (↑0.5 mm) | 3.0 mm (↓1.0 mm) |
| Output responses | Weight | 155 kg | 225.3 kg (↑70.3 kg, 45.4%) | 240.5 kg (↑85.5 kg, 55.2%) | 222.2 kg (↑67.2kg, 43.4%) |
| | LC1 – Loading (Max. von-Mises stress) | 260.0 MPa | 151.6 MPa (↓108.4 MPa, 41.7%) | 151.7 MPa (↓108.3 MPa, 41.7%) | 151.3 MPa (↓108.8 MPa, 41.8%) |
| | LC2 – Operation (Max. von-Mises stress) | 236.6 MPa | 134.2 MPa (↓102.4 MPa, 43.3%) | 148.8 MPa (↓87.8 MPa, 37.1%) | 143.4 MPa (↓93.1 MPa, 39.4%) |
| | LC3 – Braking (Max. von-Mises stress) | 285.2 MPa | 175.5 MPa (↓109.7 MPa, 38.5%) | 177.5 MPa (↓107.7 MPa, 37.8%) | 171.1 MPa (↓114.1MPa, 39.3%) |

factors for which the maximum stress under all design load cases was calculated at the allowable yield stress of 182.8 MPa or less were explored, among which the combination with the lowest weight increase rate was selected as the best design case. Table 9 shows the best design plan selected for each DOE technique.

As shown in Table 9, the best design case in all DOE methods satisfied the allowable yield stress at a level in which the maximum stress was similar for all design load cases compared to the initial design, although there was a variation in weight. Among the DOE methods for the structural design of the AOSC considered in this study, the CCD method exhibited a weight increase rate of 43.4%, which was superior to the OAD and BBD methods, while the BBD method showed the highest increase rate of 55.2%. In terms of the change in thickness of the main member, the main frame (DF-#1) thickness design factor tended to increase to the upper limit of 6.0 mm for all DOE techniques, while the remaining design factors showed variations of 1.0 mm or less. Considering the weight increase rate and the number of experiments of DOE, which represents the numerical calculation cost, CCD was shown to be the most efficient method for deriving improvement cases for the AOSC's structural design. Fig. 7 shows the overall stress and deformation distribution results of the enhanced best design case calculated from CCD for LC3.

As shown in the results of Fig. 4 and Fig. 7, the maximum stress value was improved by 39% in the best design case compared to the initial design, the location of maximum stress moved from the main frame to the center bracket, and the maximum deformation was improved by 81%. The cause of the movement of the maximum stress location is attributed to the main frame member's thickness increasing

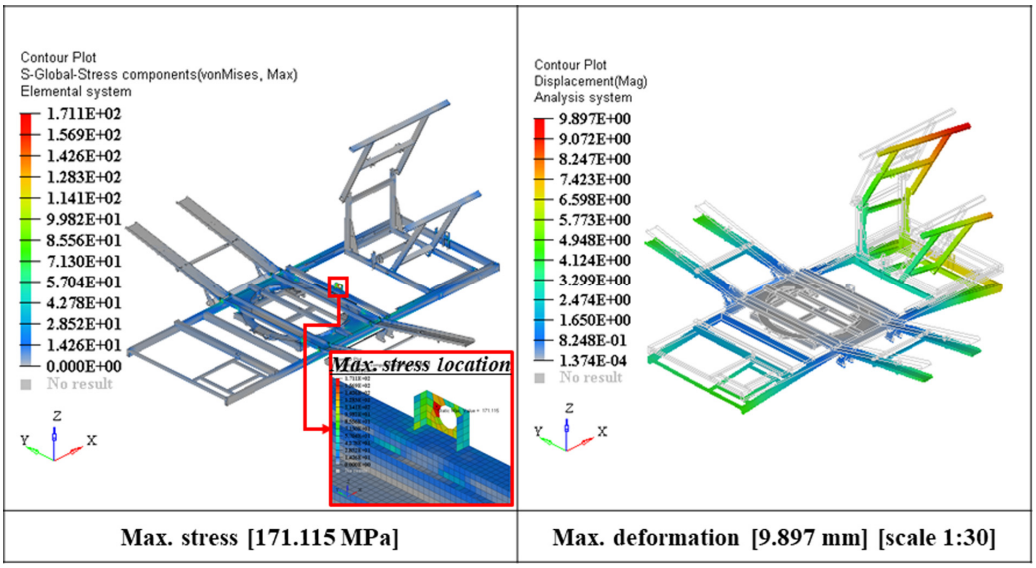


**Fig. 7** LC3 - Overall stress and deformation contours for enhanced design based on the CCD method

**Table 10** Main effect results

| Design factors | Weight | | | LC1 – Max. stress | | | LC2 – Max. stress | | | LC3 – Max. stress | | |
|---|---|---|---|---|---|---|---|---|---|---|---|---|
| | OAD | BBD | CCD | OAD | BBD | CCD | OAD | BBD | CCD | OAD | BBD | CCD |
| DF-#1 | 58.7% | 58.7% | 58.6% | 36.7% | 44.1% | 32.0% | 35.4% | 43.5% | 31.2% | 33.9% | 37.8% | 32.5% |
| DF-#2 | 23.5% | 23.5% | 23.6% | 5.9% | 4.1% | 6.2% | 6.3% | 4.8% | 6.8% | 5.3% | 3.6% | 5.9% |
| DF-#3 | 6.3% | 6.3% | 6.3% | 1.7% | 2.8% | 1.1% | 0.7% | 2.3% | 0.5% | 1.5% | 2.0% | 1.6% |
| DF-#4 | 7.1% | 7.1% | 7.1% | 0.9% | 0.7% | 0.6% | 1.4% | 0.8% | 1.6% | 1.6% | 0.7% | 1.8% |
| DF-#5 | 4.5% | 4.5% | 4.5% | 6.1% | 2.8% | 4.2% | 5.1% | 1.6% | 3.7% | 6.7% | 4.4% | 4.6% |

more than that of the bracket. Moreover, the overall structural safety improved as the maximum stress location moved from the main frame (main structural member) to the bracket (local member). A quantitative main effect analysis of the design factors for each response function was conducted according to the DOE method using the experimental matrix of OAD, BBD, and CCD, the results of which are shown in Table 10. The main effect is an indicator of the observed response function's average change according to the change in the level of the design factor, i.e., the sensitivity. As such, the greater the effect calculated for each design factor, the higher the importance for the response function of that design factor.

As shown in Table 10, in all DOE methods, the effect of the main frame (DF-#1) was greatest on the maximum stress of the weight and design load cases, and the strength of the collector frame (DF-#4) showed the lowest main effect. The principal effect on weight was nearly identical in all DOE methods, while that on the strength of DF-#1 in BBD was higher than in the other DOE methods. Accordingly, an exploration of design enhancement cases applying various DOE techniques was performed. The results indicated that the most effective exploration method was to apply CCD to enhance the strength performance of the AOSC's structural design, and that the main frame (DF-#1) was the most important structural member to consider in design.

### 3.3 Review of DOE Suitability Through Approximate Modeling

Because approximate models are typically generated from DOE, by quantitatively examining the accuracy of the generated approximate model, the overall suitability of the DOE method considering the number of experiments, the level of design variables, and DOE method selection, can be verified (Lee and Song, 2013). To verify the suitability of the sensitivity analysis results of major structural members and the exploration of AOSC improvement cases using various DOE techniques applied in Section 3.2, approximate modeling using RSM was conducted for each DOE technique, and the RSM design space exploration accuracy generated from each DOE technique was examined. The least-squares method can be used to define the RSM, a quadratic polynomial regression model, as follows (Song and Lee, 2010).

$$g = A_0 + \sum_{i=1}^{k} A_i Z_i + \sum_{i=1}^{k} A_{ii} Z_i^2 + \sum\sum_{i<1}^{k} A_i Z_i Z_j + e \tag{3}$$

From the $n$ experimental points calculated using the DOE techniques (OAD, BBD, and CCD), if matrix $Z$ expressed by $k$ basic variables and the real response vector $g$ is given, then the relationship between $g$ and $Z$ can be expressed as follows.

$$g = ZA_R + e \tag{4}$$

To minimize the random error vector $e$ and estimate the unknown RSM approximation coefficient vector $A_R$, a least squares function is applied as follows.

$$A_R = (Z^T Z)^{-1} Z^T g \tag{5}$$

Applying the approximation coefficient calculated from Eq. (5), the quadratic regression approximate model is expressed as follows.

$$\tilde{g}(x)_R = a_0^r + \sum_{i=1}^{k} a_i^r x_i + \sum_{i=1}^{k} a_{ii}^r x_i^2 + \sum\sum_{i<1}^{k} a_{ij}^r x_i x_j \tag{6}$$

An RSM approximate model of Eq. (6) is generated for each response function using the results of the DOE techniques (OAD, BBD, and CCD). Fig. 8 shows the response surface results of DF-#1 and DF-#5 (design factors with high main effect), and for LC3 (the braking case maximum stress response function) using the CDD method among the RSM approximate model results.

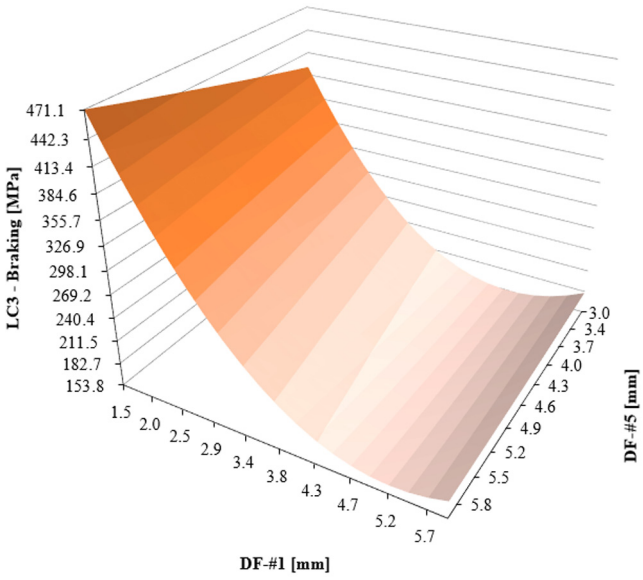


**Fig. 8** Response surface result for LC3 from the CCD method

**Table 11** Comparison of RSM accuracy

| Approximate model | $R^2$ value | | | |
|---|---|---|---|---|
| | Weight | LC1 - Loading | LC2 - Operation | LC3 - Braking |
| RSM - OAD | 1.00 | 0.976 | 0.974 | 0.976 |
| RSM - BBD | 1.00 | 0.992 | 0.977 | 0.987 |
| RSM - CCD | 1.00 | 0.973 | 0.977 | 0.989 |

As shown in Fig. 8, the RSM, a quadratic regression approximate model, effectively approximates the nonlinear design space of von-Mises stress, the LC3 response function.

The accuracy of the approximate model calculated from each DOE method is determined by $R^2$ as shown in Eq. (7).

$$R^2 = 1 - \frac{\sum(t_i - y_i)^2}{\sum(t_i - \overline{t_i})^2} \tag{7}$$

where $t_i$ is the actual value, $y_i$ is the predicted value estimated from the approximate model, and $\overline{t_i}$ is the average of the actual values. When $R^2$ is 1.0, the predicted value estimated from the approximate model exactly matches the actual value in the entire design space. Table 11 shows the accuracy analysis results of the RSM generated by the response function using each DOE technique.

As shown in Table 11, the accuracy of the approximated RSM was very high for each response function. The accuracy of the approximate model of weight was 1.0, which signifies no difference with the actual value for all DOE techniques. In terms of the accuracy of the approximate model for the response function under each design load case, an error of less than 3% of the actual value was observed, and the difference between DOE methods was found to be very small. Therefore, this study found that the overall DOE implementation method used to analyze the sensitivity of major structural members and explore enhanced design cases of the AOSC's structure was reasonable, which includes the number of experiments, levels of design variables, and DOE method selection.

## 4. Conclusions

To efficiently derive a design improvement case that secures the design safety of the AOSC, this study explored best design cases applying various DOE techniques, conducted a sensitivity analysis of major structural members, and compared the results according to DOE characteristics. The key findings of this study are summarized as follows.

(1) The structural analysis results of the initial design stage demonstrated that design improvements are required to secure the strength and safety of the AOSC's structural design. For this purpose, the influence of the major design members on strength performance was analyzed using DOE, and design improvement cases that satisfy the allowable stress while minimizing weight increase were explored.

(2) Among the three DOE methods considered in this study (OAD, BBD, and CCD), the best design case in all DOE methods satisfied the allowable yield stress at a level in which the maximum stress was similar for all design load cases compared to the initial design, although there was a variation in weight. The weight increase rate of CCD was lower than that of OAD and BBD, and that of BBD was the highest. Considering the weight increase rate and the number of experiments of DOE, which represents the numerical calculation cost, CCD was shown to be the most efficient method for deriving improvement cases for the AOSC's structural design.

(3) Given that the design problem investigated in this study in relation to CCD involves the nonlinear response characteristics of stress and five design factors, it was found that the most suitable method to evaluate the main effect and generate a high-accuracy approximate model is to conduct 43 runs of three-level experiments.

(4) As demonstrated in the structural design sensitivity analysis, in all DOE methods, the effect of the main frame (DF-#1) was greatest on the maximum stress of the weight and design load cases, and the strength of the collector frame (DF-#4) showed the lowest significant effect. The main effect on weight was nearly identical in all DOE methods, while that on the strength of DF-#1 in BBD was higher than the other DOE methods.

(5) To verify the suitability of the sensitivity analysis results of major structural members and the exploration of DOE-based AOSC improvement cases applied in this study, approximate modeling using RSM was conducted for each DOE technique. The design space exploration accuracy of RSM generated from each DOE method was examined. According to the results, the accuracy of the approximate model did not differ from the actual value in all DOE methods, and in terms of the accuracy of the approximate model for the response function under each design load case, an error of less than 3% of the actual value was observed, and the difference between DOE methods was found to be very small.

(6) This study found that the overall DOE implementation method used to analyze the sensitivity of major structural members and explore enhanced design cases of the AOSC's structure was reasonable; this includes the number of experiments, level of design variables, and DOE method selection. The DOE method-based design exploration approach proposed in this study is considered to be useful for enhancing the design performance of ocean and fisheries equipment that rely on empirical design techniques or must apply new designs.

## Acknowledgments

This paper has been written with the support of Jeollannam-do ('2019 R&D supporting program' operated by Jeonnam Technopark), and was supported by X-mind Corps program of National Research Foundation of Korea(NRF) funded by the Ministry of Science, ICT (No. 2019H1D8A1105567).

## References

Box, G.E.P., & Behnken, D.W. (1960). Some New Three Level Designs for the Study of Quantitative Variables. Technometrics, 2(4), 455-475. https://doi.org/10.1080/00401706.1960.10489912

DNV-GL. (2015). Structural Design of Offshore Units - WSD Method (DNVGL-OS-C201). Det Norske Veritas AS.

Ji, Y.J., Kwak, J.S., Lee, H.Y., & Kim, S.C. (2015). Optimal Arrangement of Resilient Mount Installed on Frame Support Structure at Shipboard Equipment under Shock Load. Journal of the Society of Naval Architects of Korea, 52(4), 298-304. https://doi.org/10.3744/SNAK.2015.52.4.298

Kim, Y., Park, P.W., Park, K.Y., & Ryu, J.C. (2015). Optimization of Arc Brazing Process Parameters for Exhaust System Parts Using Box-Behnken Design of Experiment. Journal of Welding and Joining, 33(2), 23-31. https://doi.org/10.5781/JWJ.2015.33.2.23

Lee, S.G., Han, K.U., & Park, H.J. (2019). Find Future Jobs And Value Added in Fisheries in Related Industries (KMI Trend Analysis, 161). Korea Maritime Institute.

Lee, D.M., & Kim, S.Y. (2014). Sensitivity Analysis of Design Parameters for Quadruple Offset Butterfly Valve by Operating Torque. Journal of Ocean Engineering and Technology, 28(2), 160-166. https://doi.org/10.5574/KSOE.2014.28.2.160

Lee, J., & Song, C.Y. (2013). Estimation of Submerged-arc Welding Design Parameters Using Taguchi Method and Fuzzy Logic. Proceedings of the Institution of Mechanical Engineers Part B: Journal of Engineering Manufacture, 227(4), 532-542. https://doi.org/10.1177/0954405413476487

Park, J.H., Lee, D., Yang, J.W., & Song, C.Y. (2019). Design Enhancement to Avoid Radar Mast Resonance in Large Ship using Design of Experiments. Journal of Ocean Engineering and Technology, 33(1), 50-60. https://doi.org/10.26748/KSOE.2018.088

Park, J.M., Park, C.H., Kim, T.S., & Choi, D.H. (2011). Optimal Determination of Pipe Support Types in Flare System for Minimizing Support Cost. Journal of the Society of Naval Architects of Korea, 48(4), 325-329. https://doi.org/10.3744/SNAK.2011.48.4.325

Park, S.H. (2012). Design of Experiments. Minyoung Publishing Co., Seoul.

Simulia. (2018). Abaqus User Manual. Simulia.

Song, C.Y., & Lee, J. (2010). Comparative Study of Approximate Optimization Techniques in CAE-Based Structural Design. Transactions of the Korean Society of Mechanical Engineers A, 34(11), 1603-1611. https://doi.org/10.3795/KSME-A.2010.34.11.1603

Song, C.Y., Lee, J., & Choung, J.M. (2011). Reliability-based Design Optimization of an FPSO Riser Support Using Moving Least Squares Response Surface Meta-models. Ocean Engineering, 38(1), 304-318. https://doi.org/10.1016/j.oceaneng.2010.11.001

## Author ORCIDs


| Author name | ORCID |
|---|---|
| Song, Chang Yong | 0000-0002-1098-4205 |
| Lee, Dong-Jun | 0000-0002-0610-1756 |
| Lee, Jin Sun | 0000-0002-4191-5472 |
| Kim, Eun Mi | 0000-0002-7209-6844 |
| Choi, Bo-Youp | 0000-0002-1868-5146 |

KSOE
Original Research Article

**Journal of Ocean Engineering and Technology** 34(4), 263-271 August, 2020
https://doi.org/10.26748/KSOE.2019.052

pISSN 1225-0767
eISSN 2287-6715

# 3D Topology Optimization of Fixed Offshore Structure and Experimental Validation

Hyun-Seok Kim[1], Hyun-Sung Kim[2], Byoungjae Park[1] and Kangsu Lee[3,4]

[1]*Senior Researcher, Offshore Plant and Marine Energy Research Division, Korea Research Institute of Ships and Ocean Engineering (KRISO), Daejeon, Korea*
[2]*Researcher, Offshore Plant and Marine Energy Research Division, Korea Research Institute of Ships and Ocean Engineering (KRISO), Daejeon, Korea*
[3]*Principal Researcher, Offshore Plant and Marine Energy Research Division, Korea Research Institute of Ships and Ocean Engineering (KRISO), Daejeon, Korea*
[4]*Professor, School of Ships & Ocean Engineering, University of Science and Technology, Daejeon, Korea*

**KEY WORDS:** Fixed offshore structure, 3D topology optimization, 3D metal printer, Universal testing machine, Experimental validation

**ABSTRACT:** *In this study, we performed a three-dimensional (3D) topology optimization of a fixed offshore structure to enhance its structural stiffness. The proposed topology optimization is based on the solid isotropic material with penalization (SIMP) method, where a volume constraint is applied to utilize an equivalent amount of material as that used for the rule-based scantling design. To investigate the effects of the main legs of the fixed offshore structure on its structural stiffness, the leg region is selectively considered in the design domain of the topology optimization problem. The obtained optimal designs and the rule-based scantling design of the structure are manufactured by 3D metal printing technology to experimentally validate the topology optimization. The behaviors under compressive loading of the obtained optimal designs are compared with those of the rule-based scantling design using a universal testing machine (UTM). Based on the structural experiments, we concluded that by employing the topology optimization method, the structural stiffness of the structure was enhanced compared to that of the rule-based scantling design for an equal amount of the fabrication material. Furthermore, by effectively combining the topology optimization and rule-based scantling methods, we succeeded in enhancing the structural stiffness and improving the breaking load of the fixed offshore structure.*

## 1. Introduction

Fixed-type offshore structures consist of an upper topside and a lower supporting structures to support them. These structures are designed to continuously produce gas and oil at the targeted installation site during the design life. Therefore, it may result in a considerable economic loss when damages or failures of such structures occur. Furthermore, since most of the fixed-type offshore structures are located at a distance from land and isolated, there are significant limitations for its repair. Therefore, designing a fixed offshore structure requires a high level of structural safety, which is strictly governed by the regulations of classification society. Designs based on the regulations of classification society are known to result in a safe fixed-type offshore structures. However, when series of hurricanes struck the Gulf of Mexico in 2005, more than 100 offshore structures were destroyed and over 50 were damaged. Therefore, it is necessary to develop a novel fixed-type offshore structure design beyond the existing regulations of classification society which can improve the structural stiffness.

Topology optimization maximizes the performance of the structure under given constraints. Compared to the size and shape optimizations, topology optimization has an advantage that it can yield a dramatic change in the topology of the resulting optimal design. Therefore, topology optimization has been widely used in various areas since its introduction by Bendsoe and Kikuchi (1988). However, the optimal design obtained through topology optimization was considerably challenging to implement because it has an unclear interface owing to the intermediate material density resulting from the characteristics of

Received 25 June 2019, revised 3 January 2020, accepted 22 April 2020
Corresponding author Kangsu Lee: +82-42-866-3351, klee@kriso.re.kr
It is noted that this paper is revised edition based on proceedings of KAOST 2019 in Jeju.

the solid isotropic material with penalization (SIMP) method (Bendsoe, 1995). Therefore, efforts have been undertaken to overcome the shortcomings of the stepped boundary obtained through topology optimization using the level-set function. However, due to the development of three-dimensional (3D) printing technology and advancement of computer aided design (CAD) technology, constraints on implementing the optimal design obtained from the topology optimization have been resolved and again topology optimization is attracting attention.

Since most of the obstacles on the implementation of optimal design from topology optimization, the method is gradually applied in the design of offshore structures. Lee et al. (2016) applied the topology optimization method to the design of the transition piece between a fixed-type wind turbine and a jacket-type supporting structure. They developed an optimal design where weight and stress concentration are reduced compared to the original design. Furthermore, the optimal design of transition piece improved the fatigue life of the offshore structure. Also, Kim et al. (2017) applied the topology optimization method to develop a new design of fixed jacket offshore structure panel which maximizes structural stiffness while utilizing the same amount of material of the original design that is based on the rules of classification society and compared there performance numerically. Furthermore, Lee et al. (2018) experimentally verified an optimal design of a two-dimensional (2D) fixed jacket offshore structure panel obtained through topology optimization using a universal testing machine (UTM) and 3D metal printing technology. In addition, although it is slightly different approach that was made in this research, a study was conducted to derive the optimal connectivity of structural members for the helideck of offshore structures, using a genetic algorithm and an attainable design set concept (Sim and Ha, 2019). However, in the previous studies, the topology optimization method was limitedly applied to the substructures or approximate 2D structures of offshore structures. Furthermore, the optimal connectivity of members was derived only for the joints predefined in the formulation process. Therefore, it is necessary to develop a novel offshore structure design by applying topology optimization to the entire structure.

In this study, the optimal design of a 2D fixed jacket offshore structure panel performed by Kim et al. (2017) to examine the applicability of the topology optimization method to offshore structures was expanded to 3D topology optimization of fixed offshore structures to consider the out-of-plane displacement. A 3D fixed offshore structure was designed to be installed at a certain target location using the scantling method and structural strength evaluation method proposed by Lee et al. (2017) and Kim et al. (2018). The 3D topology optimization of the fixed offshore structure was performed by using ANSYS, a commercial structural analysis software, to maximize structural stiffness under the constraint of utilizing the same amount of materials as the original design which is based on classification society rules. Furthermore, to investigate the influence of the legs of fixed-type offshore structures, which are major members to support the entire structure from external loads, they were considered in the design domain selectively and the results were compared. Furthermore, a structural test was carried out for each design by utilizing 3D printing technology, non-contact video extensometer, and UTM under compressive load. Through the experiment, improvement in the performance of the optimal design obtained from topology optimization was experimentally verified by comparing the behavior with the original design based on the classification society rules.

## 2. Optimal Design of Fixed Offshore Structure

### 2.1 Design of Fixed Offshore Structure Based on Classification Society Rules

The design of fixed offshore structures based on the classification society rules is performed using cylindrical members. However, since the topology optimization in this study is performed based on 3D solid elements, these were considered with square cross-sections for experimentall validation as shown in Fig. 1(a). A 130m fixed jacket structure (Kim et., 2018), which is designed based on the AISC (American Institute of Steel Construction) Code of Standard Practice for Steel Buildings and Bridges (AISC, 2016) and API(American Institute of Steel Construction) Recommended Practice 2A-WSD (API, 2002), was used as a reference for the original design of 3D fixed offshore structure considered in this research. Here, wind, wave, and current loads at extreme condition were considered as external loads acting on the structure. The applied wind load was 53 m/s. A wave with a height of 16 m was applied as the wave load, and the fifth order stream

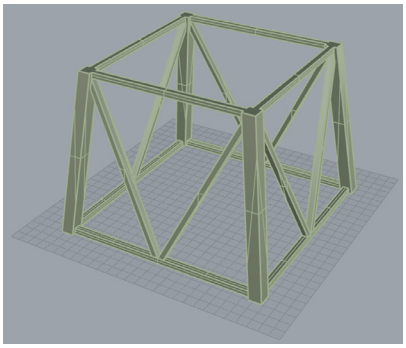

(a) 3D view of rule scantling based design

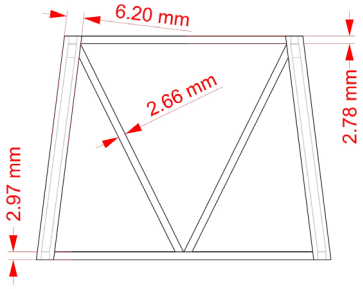


(b) Dimensions of rule scantling based design

**Fig. 1** Rule scantling based design of fixed offshore structure

function theory corresponding to a period of 14 s was applied. A profile which decreases with an increase in the water depth was used for the current load with the surface current velocity of 2.495 m/s. To compare the structural performance of the optimal design derived through topology optimization with that of the design based on the classification society rules, designs of the fixed offshore structure were fabricated utilizing 3D metal printer with the scale ratio of approximately 273:1. Dimensions of each member are shown in Fig. 1(b).

### 2.2 3D Topology Optimization Formulation of the Fixed Offshore Structure

The 3D topology optimization of the fixed offshore structure based on the solid elements was formulated to minimize the structural compliance of the structure, so that the structural stiffness of the structure could be maximized. The structural compliance is expressed as the product of the external force $f$ and displacement $u$ for the number of elements (NE) in the entire design domain, as shown in Eq. (1). To compare and verify the high effectiveness of the optimal designs derived by topology optimization, a volume constraint using the relative material density $\rho_i$ and initial volume $V_0$ of each element is introduced as Eq. (2). Thereby, an amount of material ( $V_c$) equal to that in the rule-based scantling design (shown in Fig. 1) could be used in the topology optimization. Based on SIMP, the design variables in the 3D topology optimization problem of the fixed offshore structure can be expressed with $\rho_i$ and the initial material property $E_0$ of each element as shown in Eq. (3). Here, the penalty parameter $n$ was set as 3. The penalty parameter interpolates the relative material density so that it can be close to the extreme values of 0.0 and 1.0 to reduce the proportion of members with intermediate densities in the topology optimization. It generally exhibits stable convergence at values

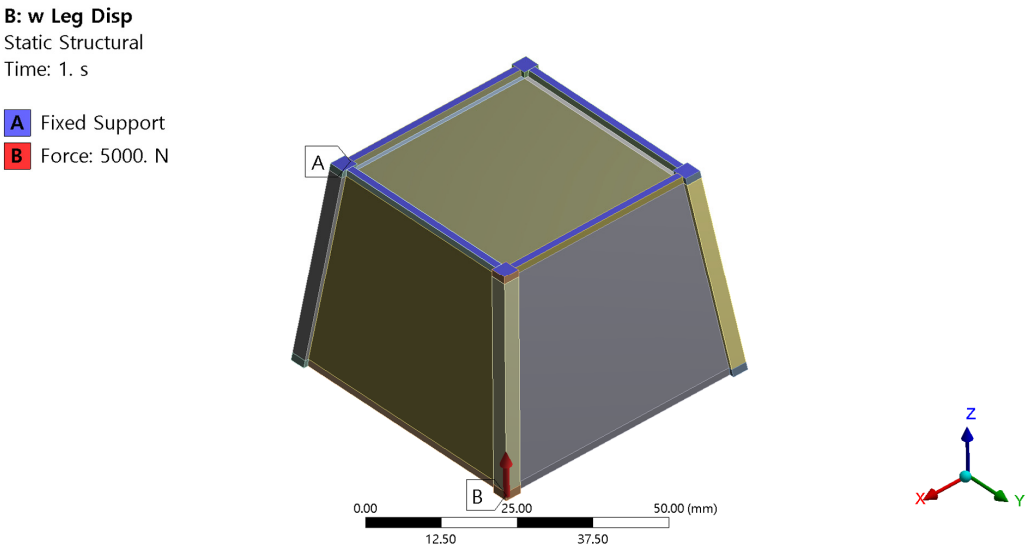


(a) Displacement boundary condition

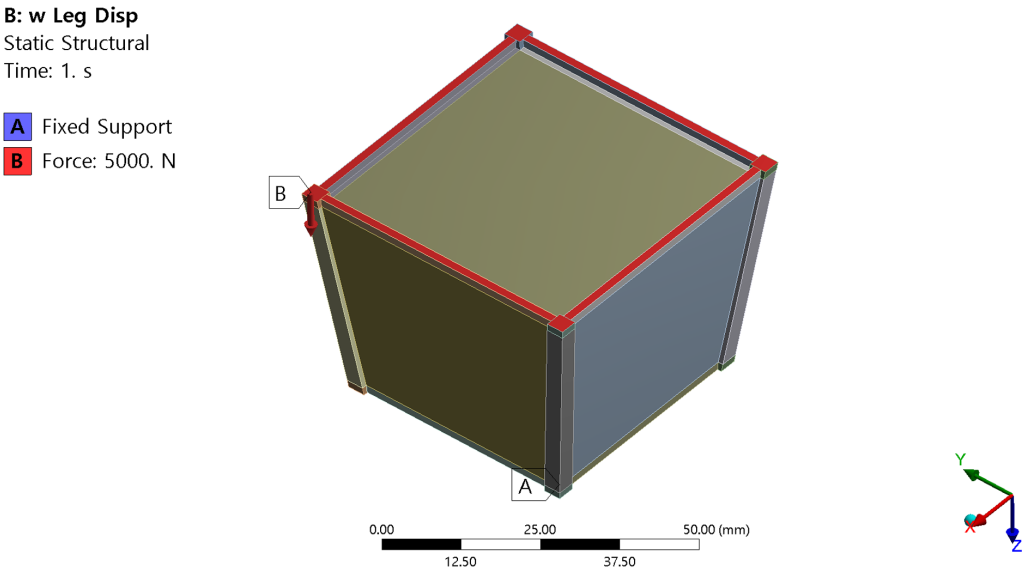


(b) Force boundary condition

**Fig. 2** Boundary conditions for 3D topology optimization of fixed offshore structure

between 2 and 4. Furthermore, a very small value was selected as the lower limit of the relative material density (as shown in Eq. (4)) to prevent singularity in numerical analysis owing to the void elements generated in the topology optimization process.

$$Minimize\ C = \sum_{i=1}^{NE} f_i u_i \tag{1}$$

$$Subject\ to\ \sum_{i=1}^{NE} \rho_i V_0 \leq V_c \tag{2}$$

$$E_i = \rho_i^n E_o \quad (i = 1,2,...,NE) \tag{3}$$

$$0 < \rho_{\min} \leq \rho_i \leq 1 \tag{4}$$

### 2.3 Boundary Conditions and Design Domain for 3D Topology Optimization of the Fixed Offshore Structure

The displacement and force boundary conditions of the fixed offshore structure were assigned to the top and bottom of the structure, respectively, considering connectivity, as shown in Fig. 2. A fixed boundary condition is applied as the displacement boundary condition. A compression load owing to the self-weight of the topside structure was assigned as the force boundary condition. In general, fixed offshore structures experience large loads in the horizontal direction. However, in this study, a compression load of 5 kN caused by the self-weight of the top structure was assumed to seek the applicability of the topology optimization method to the design of fixed offshore structures. Topology optimization problem is a problem of determining the optimal connectivity of members (i.e., the topology),

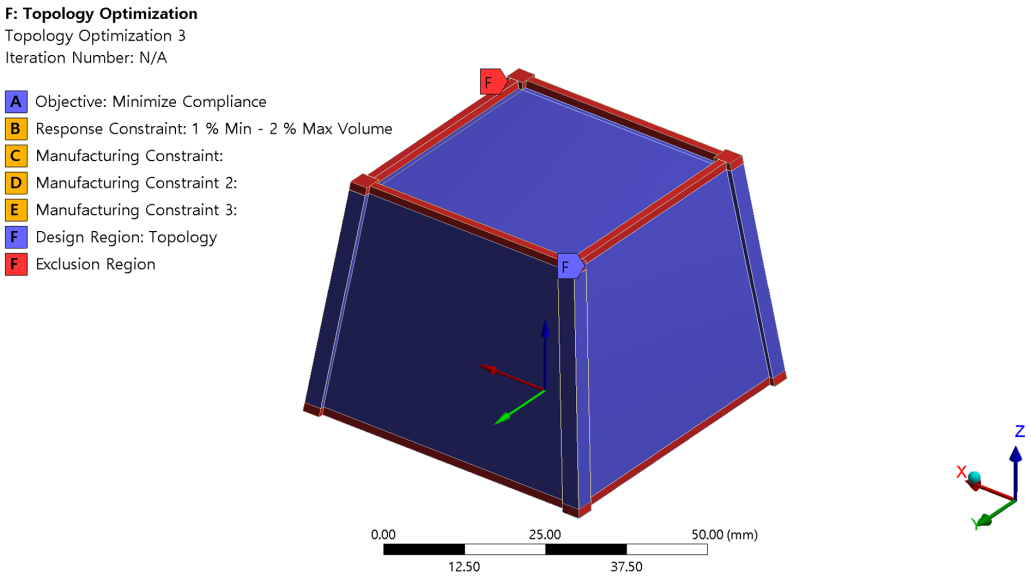


(a) Design domain including region of legs

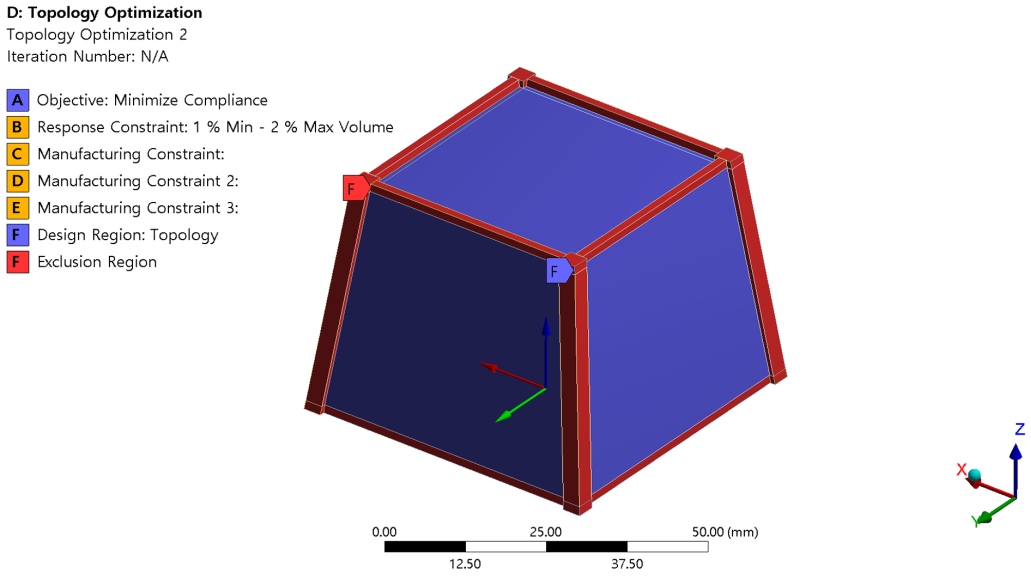


(b) Design domain excluding region of legs

**Fig. 3** Design domains for 3D topology optimization of fixed offshore structure

which maximizes the stiffness of the structure under the given force and displacement boundary conditions. However variation in the magnitude of the loads within the elastic region does not significantly affect the result of the topology optimization.

The blue colored area in Fig. 3 indicates the design domain considered in the topology optimization of the fixed offshore structure. To investigate the influence of the legs of original fixed offshore structure based on the rules of classification society, design domains with and without considering legs are introduced as Fig. 3(a) and Fig. 3(b), respectively. The red colored areas, expect the legs, in Fig. 3 are the horizontal braces and are excluded from the design domains since the force and displacement boundary conditions are applied. A minimum member thickness constraint was applied to prevent the generation of thin members through the topology optimization. Symmetric conditions and minimum and maximum element sizes were additionally considered for the experimental validation of topology optimization results utilizing 3D metal printing.

### 2.4 3D Topology Optimization of the Fixed Offshore Structure

The 3D topology optimization of the fixed offshore structure was performed using ANSYS Workbench Mechanical Enterprise 2019 R1, a commercial structural analysis software . Here, the static structural module and the topology optimization module were employed for structural analysis and topology optimization, respectively. The 3D optimal designs of the fixed offshore structure that satisfy the given displacement and force boundary conditions as well as the volume constraint were derived as shown in Fig. 4. When the legs of the fixed offshore structure were considered in the design domain under the

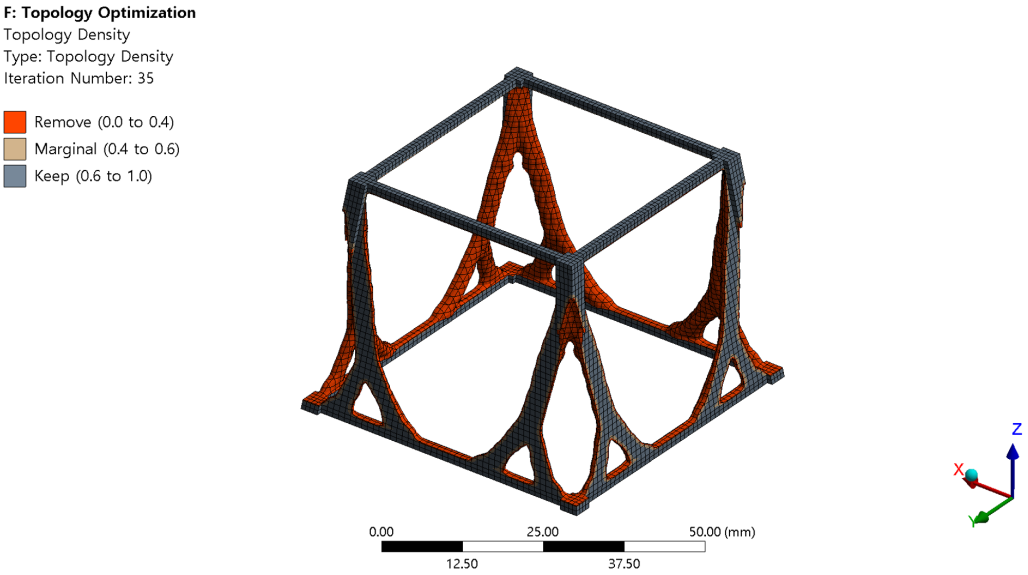


(a) Optimal design without legs

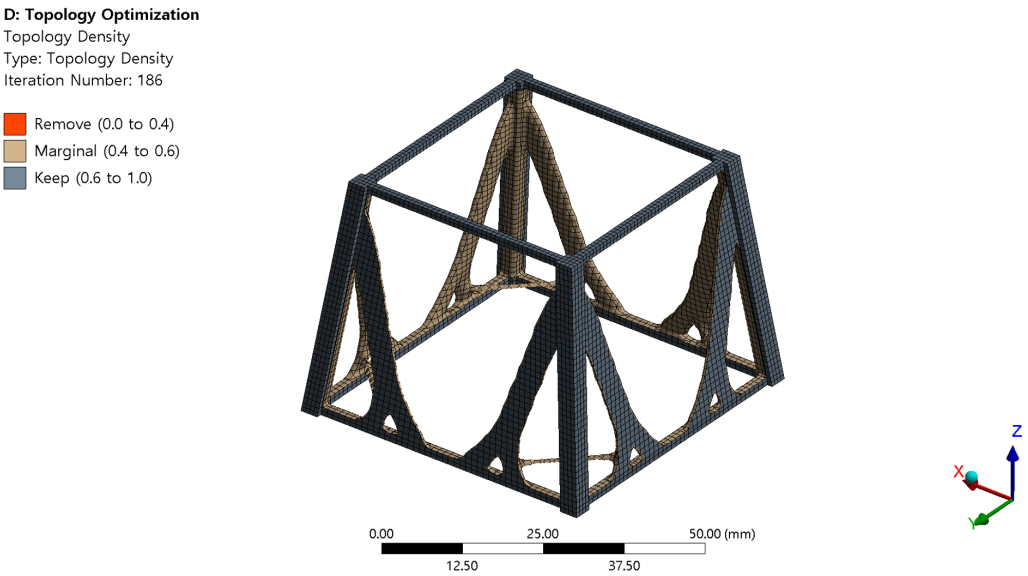


(b) Optimal design with legs

**Fig. 4** Optimal designs obtained from 3D topology optimization of fixed offshore structure

**Table 1** Volume comparison of each design

| Design | Volume ($mm^3$) | Ratio (%) |
|---|---|---|
| Rule scantling based design | 23,385.66 | 100.00 |
| Optimal design without legs | 23,835.05 | 101.92 |
| Optimal design with legs | 23,500.26 | 100.49 |

compression load (Fig. 4(a)), the top sections of the legs were included in the load transfer path and their shapes were maintained. However, the bottom sections were replaced by the Y-shaped braces on both the sides. Meanwhile, when the legs were excluded from the design domain of the topology optimization (Fig. 4(b)), Y-shaped braces similar to the ones in the previous case were generated on both sides of the legs. However, these braces show a relatively thin thickness and wide width compared to the previous optimal design. It was also observed that horizontal braces for reinforcing the space between each plane were freshly generated to increase the stiffness for the out-of-plane displacement under the given load condition. Table 1 compares the volumes of the optimal designs derived through topology optimization (shown in Fig. 4) with that of the rule-based scantling design (shown in Fig. 1). As shown in the table, the optimal designs obtained through topology optimization exhibited volume differences of less than 2%, from the rule-based scantling design.

### 2.5 Conversion of the Topology Optimization Results into CAD Data

The topology optimization of the fixed offshore structure was performed using ANSYS considering the constraints for 3D metal printing. Thus, it cannot stringently satisfy the volume constraint of the use of an amount of material equal to that in the rule-based scantling design, which was applied in this study. Therefore, in this study, the relative material densities of the elements that express the boundaries of the structure in the optimal designs obtained through topology optimization were adjusted so that the results of the topology optimization could match the amount of material in the rule-based scantling design with a maximum error of approximately 3%. In addition, the optimal designs obtained by the topology optimization are derived in the form of mesh data because the topology optimization method is based on the finite element method. Therefore, it is necessary to convert these mesh data into CAD information to fabricate specimens utilizing 3D metal printer to be used in the structural test for experimental validation of the topology optimization results. The mesh data derived through the topology optimization were directly converted into CAD information, i.e., into standard tessellation language (STL) geometry that satisfies the given volume constraint, using SpaceClaim of ANSYS Workbench Mechanical Enterprise 2019 R1. Fig. 5 shows the results of converting each optimal design of the fixed offshore structure into CAD information.

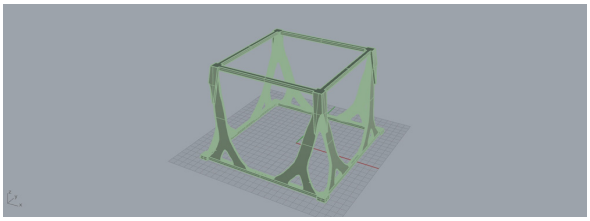

(a) CAD data of optimal design without legs

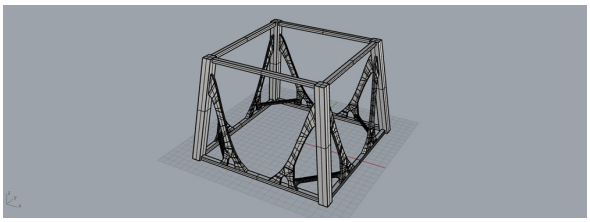

(b) CAD data of optimal design with legs

**Fig. 5** Conversion of topology optimization results to CAD data

## 3. Experimental Validation of Topology Optimization of Fixed Offshore Structure

### 3.1 Fabrication of Structural Test Specimens Using a 3D Metal Printer

To experimentally verify the effectiveness of topology optimization, the specimens of the rule-based scantling design and the optimal designs derived through 3D topology optimization were fabricated from Inconel 718 (a nickel–chromium-based alloy) and a 3D metal printer, as shown in Fig. 6. The properties of materials do not significantly affect its results because topology optimization aims to

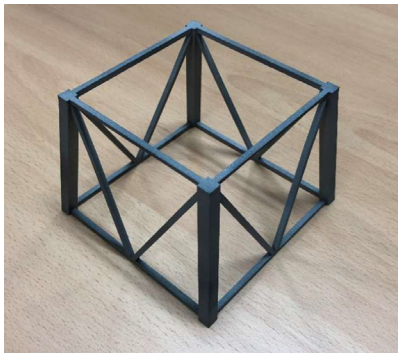

(a) Rule scantling based design

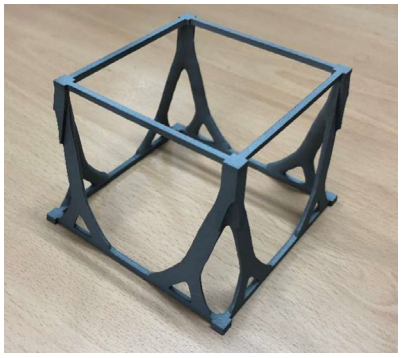

(b) Optimal design without legs

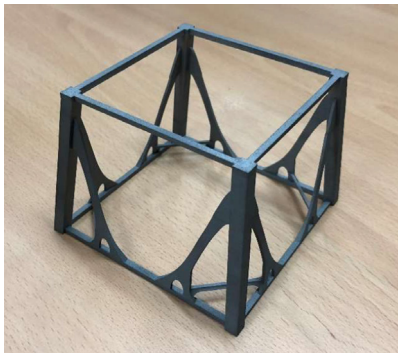

(c) Optimal design with legs

**Fig. 6** Manufacturing of fixed offshore structure designs by utilizing 3D metal printer

**Table 2** Mechanical properties of Inconel 718

| Material | Density ($g/cm^3$) | Tensile strength (MPa) | Yield strength (MPa) |
|---|---|---|---|
| Inconel 718 | 8.19 | 1,350 | 1,180 |

determine the connectivity of materials that maximizes the stiffness of the structure. Inconel 718, one of the commonly used materials for 3D metal printing, was used in this study to examine the applicability of topology optimization to the design of fixed offshore structures. Its mechanical properties are summarized in Table 2.

### 3.2 Experimental Validation of the Topology Optimization Results

A structural test was conducted under compressive loading using a 100 ton UTM (as shown in Fig. 7) for experimental validation of each optimal design of the fixed offshore structure obtained from 3D topology optimization. The UTM was set to control the maximum displacement of the specimen, and it was operated at the rate of 5 mm/min. The test was conducted until each specimen fractured as shown in Fig. 8. Through the structural test, the displacement and load under compressive loading were derived for the rule-based scantling design, optimal design without legs in the design domain, and optimal design with legs in the design domain. The reaction force of each structure measured by the UTM according to the vertical displacement is expressed through the force–displacement curves in Fig. 9. Since topology optimization is a method for determining the connectivity of members that maximizes the stiffness of the structure in the elastic region, the degree of improvement in the stiffness of the structure because of topology optimization can be obtained by comparing the displacement of the optimal designs derived through topology optimization to that of the existing design under a similar load. The topology optimization of the fixed offshore structure was performed considering a design load of 5 kN, where the structure is assumed to be within the elastic region. However, in this study, we compared the displacement and its ratio when 100 kN load is applied to clearly show the effectiveness of topology optimization, as tabulated in Table 3, since the original rule based offshore jacket design is out of elastic region while optimal designs are still inside or at the end stage of elastic region. As shown in the table, the optimal design that did not consider legs in the design domain during topology optimization and the optimal design that included legs in the design domain exhibited approximately 30% and 12% lower displacement, respectively, compared with the rule-based scantling design under the same load.

This result is due to the improvement in the structural stiffness of the fixed offshore structure from topology optimization. It was also observed that the optimal design that did not consider the legs of the rule-based scantling design exhibited a higher degree of improvement in structural stiffness than the optimal design that included the legs, under compressive loading. However, the optimal design when legs are considered in the design domain showed a higher fracture load than the optimal design without legs considered in the design domain,

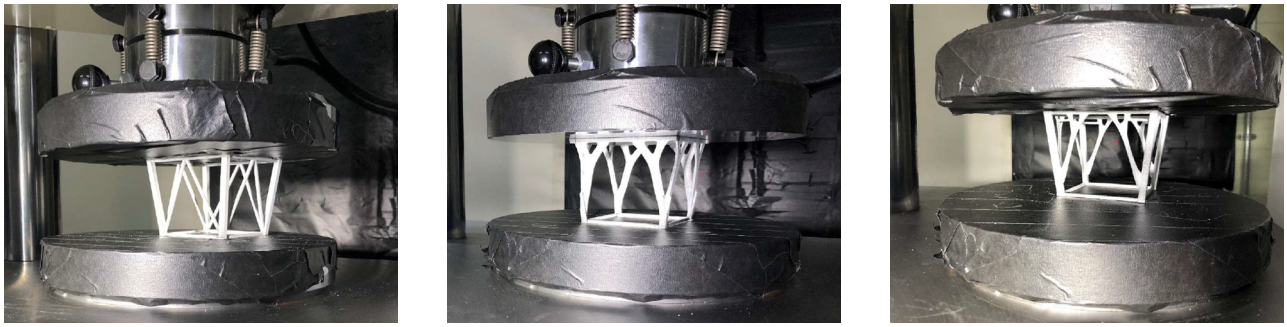

(a) Experiment of rule scantling based design (b) Experiment of optimal design without legs (c) Experiment of optimal design with legs

**Fig. 7** Structural experiment of fixed offshore structure designs by utilizing UTM

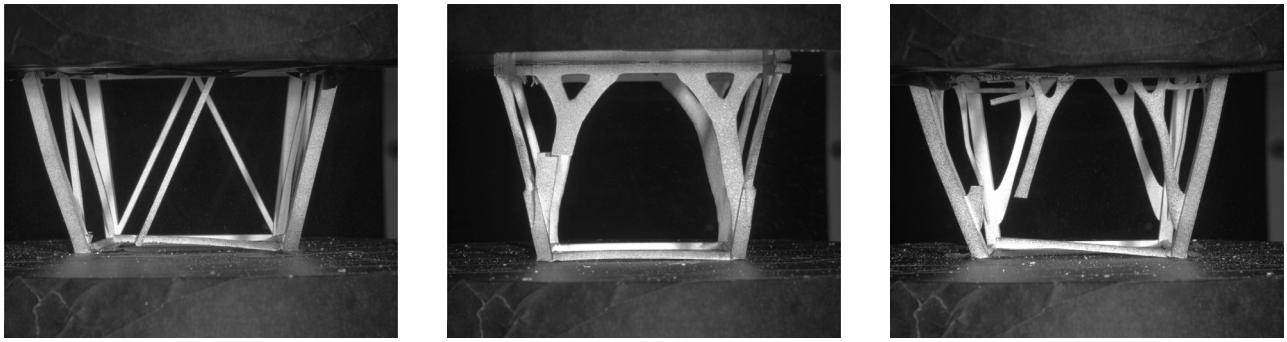

(a) Rule scantling based design specimen (b) Optimal design without legs specimen (c) Optimal design with legs specimen

**Fig. 8** Last step of the structural experiments of each specimen

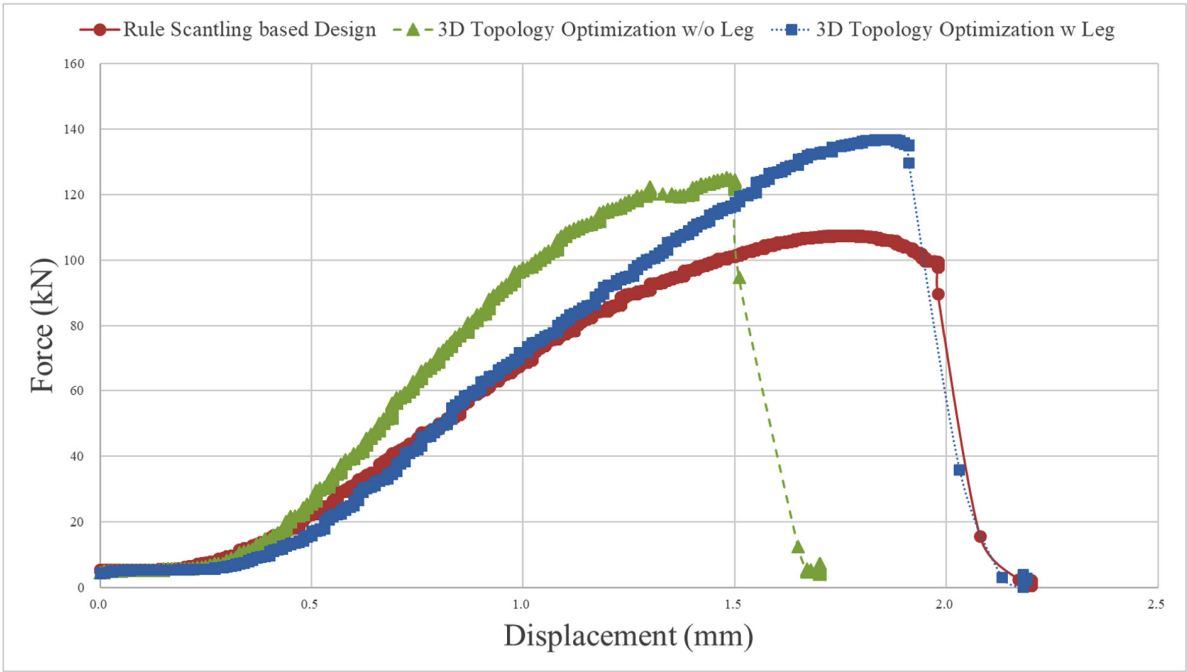


**Fig. 9** Force-displacement curves obtained from structural experiment

**Table 3** Displacement and load comparison

| | Displacement at 100 kN (mm) | Displacement Ratio |
|---|---|---|
| RCS design | 1.46 | 1.00 |
| Optimal design without legs | 1.04 | 0.71 |
| Optimal design with legs | 1.29 | 0.88 |

although it exhibited relatively lower structural stiffness. This implies that when rule-based scantling method, which has been developed based on long experience and knowledge, and the topology optimization method, which is capable of deriving innovative design and optimal connectivity, are effectively combined, it is possible to improve the structural stiffness as well as their structural performance.

## 4. Conclusion

In this study, the optimal designs of a fixed offshore structure with improved structural stiffness were derived through 3D topology optimization using the same amount of material as the original rule based design. To examine the influence of the legs of the rule-based scantling design on the structural stiffness of the structure, they were considered selectively in the design domain of the topology optimization problem. For experimental validation, mesh and material data obtained from topology optimization is converted to CAD data utilizing ANSYS SpaceClaim and manufactured employing 3D metal printing technology.

Through the structural experiment utilizing UTM, it is shown that optimal designs obtained from topology optimization show improvement in structural stiffness compared to the original rule-based design. Optimal design which considered legs as design domain showed higher structural stiffness compared to the one not considering legs in the design domain. However, the optimal design derived when the legs were not considered in the design domain of the topology optimization problem showed the highest fracture load, although the degree of improvement in its structural stiffness was relatively lower than that when the legs were considered. This implies that it is possible to improve the stiffness and structural performance of structures by effectively combining the rule-based scantling method with the topology optimization method, which is capable of deriving the connectivity of members that improves the structural stiffness of fixed offshore structures. Although to implement this developed technique to the industry, a method which can consider cylindrical members in topology optimization, as well as consideration of manufacturability, productivity, transportation, and various environmental loadings is necessary. Furthermore, it is also essential to review the structural safety based on the rules of classification society of the proposed optimal designs.

## Acknowlogement

This research was supported by a grant from Endowment Project of “Core Technology Development of Hydro-elasticity based Structural Damage Assessment for Offshore Structures considering Uncertainty” funded by Korea Research Institute of Ships and Ocean engineering (PES3490).

## References

American Petroleum Institute. (2002). API Recommended Practice

2A-WSD. Washington, D.C.: API Publishing Service.

American Institute of Steel Construction. (2016). The 2016 AISC Code of Standard Practice for Steel Buildings and Bridges (ANSI/AISC 303-16). Chicago, Illinois: AISC.

Bendsoe, M.P., & Kikuchi, N. (1988). Generating Optimal Topologies in Structural Design using a Homogenization Method. Computer Methods in Applied Mechanics and Engineering, 71(2), 197-224. http://dx.doi.org/10.1016/0045-7825(88)90086-2

Bendsoe, M.P. (1995). Optimization of Structural Topology, Shape, and Material. Heidelberg, Berlin: Springer. https://doi.org/10.1007/978-3-662-03115-5

Kim, D., Lee, K., Kim, B.W., Park, B., & Kim, H.-S. (2018). Jacket Design and Structural Strength Evaluation of Fixed Offshore Platform. Proceedings of The Korean Association of Ocean Science and Technology Societies Joint Conference, Jeju, Korea, 307-311.

Kim, H.-S., Lee, K., Park, B., & Kim, D. (2017). A Comparative Study of Offshore Platform Design Based on Rule Scantling and Topology Optimization. Proceedings of International Mechanical Engineering Congress and Exposition, Tampa, Florida.

Lee, K., Park, B., Kim, H.-S., & Kim, D. (2017). Study of Rule Scantling Method and Structural Strength Evaluation to Obtain Structural Design Technology for Fixed Offshore Platform. KRISO Technical Report, 58, 69-79.

Lee, K., Kim, H.-S., Park, B., & Kim, D. (2018). Topology Optimization of Offshore Jacket Structure Panel and Experimental Validation. Proceedings of The Korean Association of Ocean Science and Technology Societies Joint Conference, Jeju, Korea, 280-283.

Lee, Y.-S., Gonzalez, J.A., Lee, J.H., Kim, Y.I., Park, K.C., & Han, S. (2016). Structural Topology Optimization of the Transition Piece for an Offshore Wind Turbine with Jacket Foundation. Renewable Energy, 85, 1214-1225. https://doi.org/10.1016/j.renene.2015.07.052

Sim, K., & Ha, S.-H. (2019). Structural Design Optimization of Lightweight Helidecks using Genetic Algorithm and Attainable Design Sets. Proceedings of Computational Structural Engineering Institute of Korea Annual Conference, Busan, Korea, 99.

## Author ORCIDs



| Author name | ORCID |
|---|---|
| Kim, Hyun-Seok | 0000-0001-5803-6477 |
| Kim, Hyun-Sung | 0000-0002-2627-6625 |
| Park, Byoungjae | 0000-0002-8943-1477 |
| Lee, Kangsu | 0000-0002-9505-6802 |

KSOE
Original Research Article

**Journal of Ocean Engineering and Technology** 34(4), 272-276 August, 2020
https://doi.org/10.26748/KSOE.2019.058

pISSN 1225-0767
eISSN 2287-6715

# Optimization Approach for a Catamaran Hull Using CAESES and STAR-CCM+

Zhang Yongxing[1] and Dong-Joon Kim[2]

[1]*Graduate Student, Interdisciplinary Program of Marine Convergence Design, Pukyong National University, Busan, Korea*
[2]*Professor, Department of Naval Architecture and Marine Systems Engineering, Pukyong National University, Busan, Korea*

**KEY WORDS:** Optimization, Catamaran, CAESES, STAR-CCM+, Free-form deformation, Non-dominated sorting genetic algorithm (NSGA)-II

**ABSTRACT:** *This paper presents an optimization process for a catamaran hull form. The entire optimization process was managed using the CAD-CFD integration platform CAESES. The resistance of the demi-hull was simulated in calm water using the CFD solver STAR-CCM+, and an inviscid fluid model was used to reduce the computing time. The Free-Form Deformation (FFD) method was used to make local changes in the bulbous bow. For the optimization of the bulbous bow, the Non-dominated Sorting Genetic Algorithm (NSGA)-II was applied, and the optimization variables were the length, breadth, and angle between the bulbous bow and the base line. The Lackenby method was used for global variation of the bow of the hull. Nine hull forms were generated by moving the center of buoyancy while keeping the displacement constant. The optimum bow part was selected by comparing the resistance of the forms. After obtaining the optimum demi-hull, the distance between two demi-hulls was optimized. The results show that the proposed optimization sequence can be used to reduce the resistance of a catamaran in calm water.*

## 1. Introduction

Simulation-driven design is one of the most important methods for ship optimization. With the development of computer-aided design technology, research on hull shape optimization through computer simulation has gradually been applied to design more energy-efficient and environmentally friendly ships. In the preliminary design stage, it is very important to optimize the hydrodynamic characteristics of the hull form. As computers speed up and memory grows, researchers are experimenting more with Computer Aided Design (CAD) and simulation (CFD) methods.

Due to the complex geometry shape of a ship's hull, it is difficult to use numerical methods to describe it. Therefore, researchers often choose to modify the hull form by making changes to a basic design. Lackenby (1950) developed a method to modify a hull by controlling the position of the center of buoyancy and shifting the section curves. Since then, the Lackenby method has been widely used in hull modification.

In recent years, there have mainly been two popular ways of modifying a bulbous bow geometry: parametric modeling and the Free-Form Deformation (FFD) method. Chrismianto and Kim (2014) used a Cubic Bezier curve and curve-plan intersection methods to generate a parametric bulbous bow. Luo and Lan (2017) used a B-Spline curve and NURBS curve to generate a parametric bulbous bow in the CAD-CFD integration platform CAESES. Plug-in software called Grasshopper was used to generate a parametric bulbous bow from a few vertexes and NURBS curves.

The wave-making resistance of a ship hull depends largely on the bow part (the area between the stem and mid-ship). It is efficient to optimize the bow part of a ship to reduce the wave-making resistance. The bulbous bow and the hull between the bulbous bow and mid-ship are two main parameters to optimize.

Different governing equations are used in a CFD solver to predict a ship hull's hydrodynamic performance. One of the most popular methods is the Reynolds averaged Navier-Stokes (RANS) method. Zhang et al. (2018) used the RANS method to calculate the total resistance in an optimization framework (Park et al., 2019; Kim et al., 2019). Usually, hundreds of simulations are carried out in an optimization process, and the hydrodynamic performance prediction can be quite a time consuming. Researchers have tried different ways to reduce the computing time. Han et al. (2012) selected a non-linear potential flow using the Rankine panel method to predict trim and sink

Received 12 July 2019, revised 22 June 2020, accepted 16 July 2020
Corresponding author Dong-Joon Kim: +82-51-629-6614, djkim@pknu.ac.kr

during a simulation. Kostas et al. (2015) used the Neumann-Kelvin formulation and the boundary element method (BEM) to simulate the wave-making resistance.

Many kinds of optimization equations have been used to find an optimal solution quickly and accurately. Zhang et al. (2018) used the Particle Swarm Optimization (PSO) algorithm to help find an optimal bulbous bow. Huang et al. (2016) implemented a "new improved Artificial Bee Colony" (NIABC) algorithm in KCS hull optimization. Gammon implemented a Multi-Objective Genetic Algorithm (MOGA) in the optimization of a fishing vessel, and the optimization equations showed high accuracy and efficiency.

In this study, the wave-making resistance of a catamaran in calm water was selected as the objective function for optimization. The length, breadth, and angle of the bulbous bow were modified by the FFD method and then optimized by the Non-dominated Sorting Genetic Algorithm (NSGA)-II. The bow part was optimized by simulating nine different hull forms that were modified by the Lackenby method and then comparing them. Finally, after obtaining the optimal demi-hull, the distance between two demi-hulls was optimized.

## 2. Demi-hull Geometry Modification Method

### 2.1 Bulbous Bow Modification

The FFD and Lackenby methods were applied to modify the hull geometry. The bulbous bow area begins from station No. 20, and it was modified in three dimensions: the length, breadth, and its angle with the baseline. Fig. 1 shows how the FFD method is applied to the bulbous bow. The bulbous bow shape is modified by a control box with certain control points on it (Tomas and Scott, 1986). The bulbous bow angle $\alpha$ is defined in Fig. 1c as the angle between the base line and the rotated control box. The clockwise direction is defined as positive, and the anticlockwise direction is defined as negative.

Fig. 2 shows the length of the bulbous bow modified under the constraint of $-0.02LOA \leq \Delta L \leq 0.02LOA$, where $\Delta L$ is the change of length of the bulbous bow, and $LOA$ is the overall length. Fig. 3 shows the breadth of the bow modified under the constraint of $0.8B \leq B' \leq 1.3B$, where $B$ is the original breadth of the bow, and $B'$ is the breadth of the new bow. Fig. 4 shows the angle of the bow modified under the constraint of $-9° \leq \alpha \leq 3°$, where $\alpha$ is the difference from the original angle.

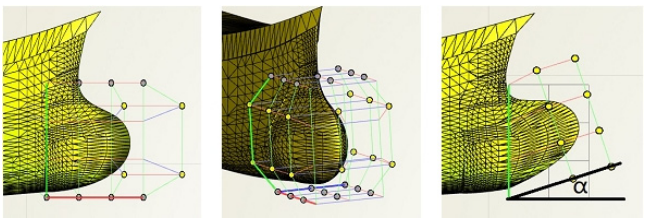


(a) (b) (c)

**Fig. 1** The FFD method for the length (a), breadth (b) and angle (c) of the bulbous bow

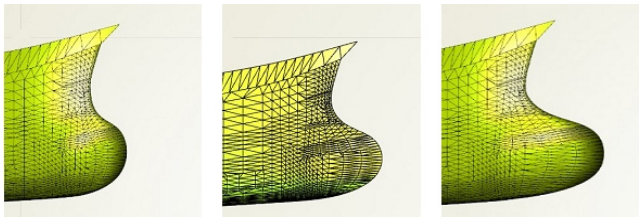

(a) (b) (c)

**Fig. 2** Right view of the bulbous bow at (a) $\Delta L$ of $-0.02LOA$, (b) original $\Delta L$, and (c) $\Delta L$ of $0.02LOA$

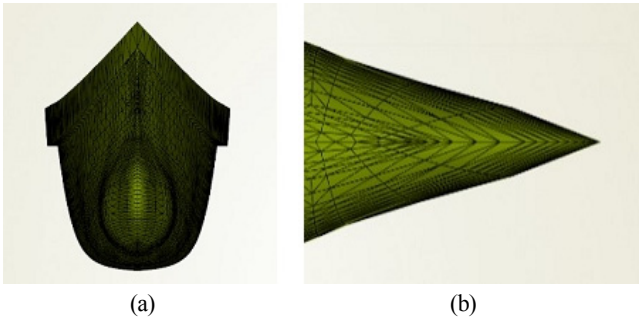

(a) (b)

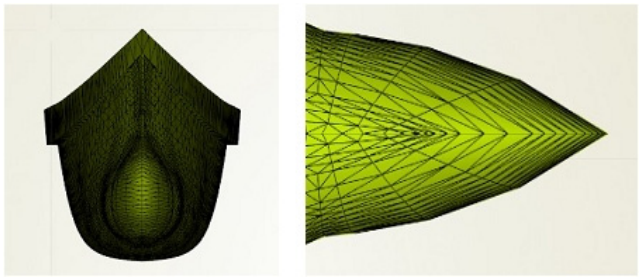

(c) (d)

**Fig. 3** Front view (a) and Top view (b) of the bulbous bow at a breadth of $0.8B$ and front view (c) and top view (d) at a breadth of $1.3B$

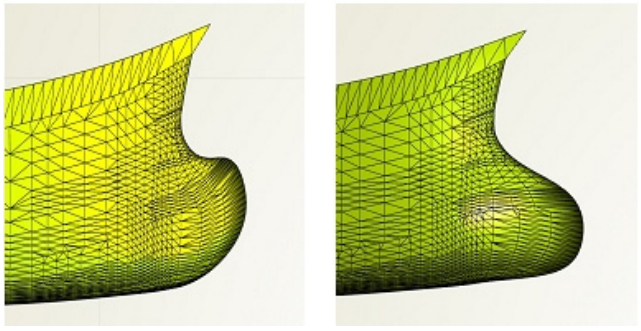

**Fig. 4** Right view of the bulbous bow at an angle of -9° (left) and an angle of 3° (right)

### 2.2 Bow Part Modification

The bow part is the part of the hull between the bulbous bow and mid-ship. The Lackenby method was used for the bow part modification. The longitudinal center of buoyancy (LCB) was changed slightly while the displacement was kept constant. The change in LCB ($\Delta LCB$) was set as a design variable. Fig. 5 shows the bow part

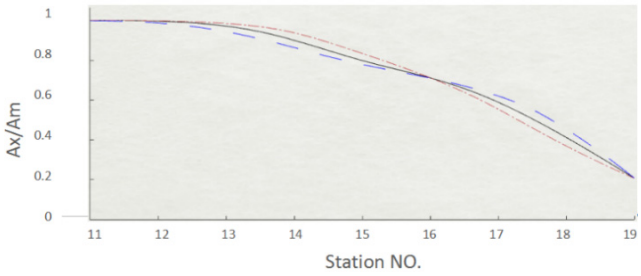


**Fig. 5** Sectional area curve of bow part with LCB moved forward by 0.4% (blue) and backward by 0.4% (red)

modified by moving the LCB by ±0.4%. The inflection point of the original sectional area curve was located around station 16, so this station was set to be the modification center.

## 3. Numerical Calculation by STAR-CCM+

A high-speed catamaran was selected as an example for optimization, and its main data are shown in Table 1. The high-speed catamaran travels with a high Froude number (i.e., $Fn > 0.3$). In this case, the viscous resistance is usually a smaller proportion of the total resistance, and the contribution of the bow part to the viscous resistance is negligible. Therefore, optimizing the resistance in an inviscid fluid is an effective way to optimize the performance of the high-speed ship. STAR-CCM+ was selected to perform the numerical simulation and evaluation, and the fluid model was set as an inviscid fluid model.

To reduce the computing time and ensure the accuracy of the wave pattern of the free surface, the mesh was set to be relatively thin in the Z direction and wide in the X and Y directions, as in Fig. 6. A total of 460,000 mesh cells were generated, and the mesh is shown in Fig. 6.

**Table 1** Main data of the demi-hull

| Item | Value |
|---|---|
| $L_{OA}$ | 21.7 (m) |
| $L_{PP}$ | 20.0 (m) |
| $B$ | 2.5 (m) |
| $D$ | 3.2 (m) |
| $d$ | 1.6 (m) |
| $V$ | 10.28 (m/s) |
| $Fn$ | 0.73 |

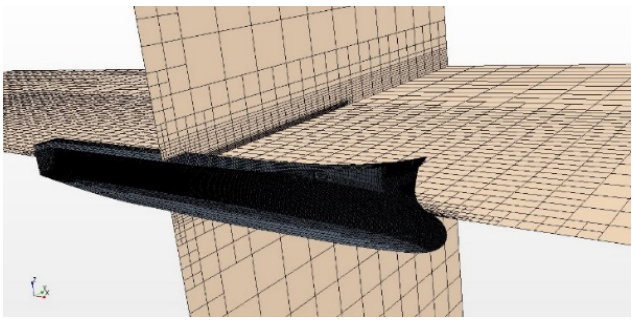

**Fig. 6** Mesh distribution for the simulation

## 4. Software Integration and Demi-hull Optimization

### 4.1 Bulbous Bow Optimization

The resistance was simulated in STAR-CCM+ and fed back to CAESES by coupling the two programs. The FFD method was used to modify the bulbous bow shape with the design variables: the length, breadth, and angle. NSGA-II was then used to obtain the optimal bulbous bow.

Fig. 7 shows a flow chart of the NSGA-II process for the design variables of the bulbous bow. Firstly, 27 initial design plans were generated by changing the bulbous bow length, breadth, and angle defined by the FFD method as the first generation. 27 simulations were then carried out in STAR-CCM+ to obtain the resistance results. The plans that performed well were selected to mutate and crossover to obtain the next generation.. New generations of hull plans were simulated and selected again and again until the resistance results converged.

Fig. 8 shows the resistance results of the inviscid fluid after 5 generations of different bulbous bow plans. The results are from 135 simulations carried out by STAR-CCM+. The noted point represents the optimal solution. Fig. 9 shows the evolution of the length, breadth, and angle. It can be seen that the length converges to 1.018, the breadth converges to 1.14, and the angle converges to 2.64°.

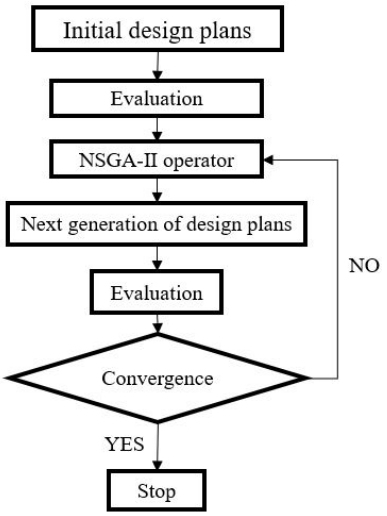


**Fig. 7** NSGA-II algorithm process in CASES

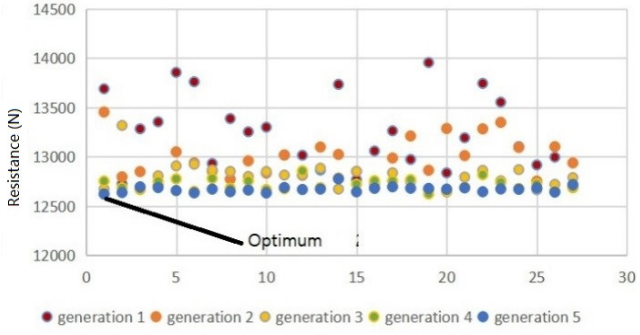


**Fig. 8** Resistance of inviscid fluid after 5 generations

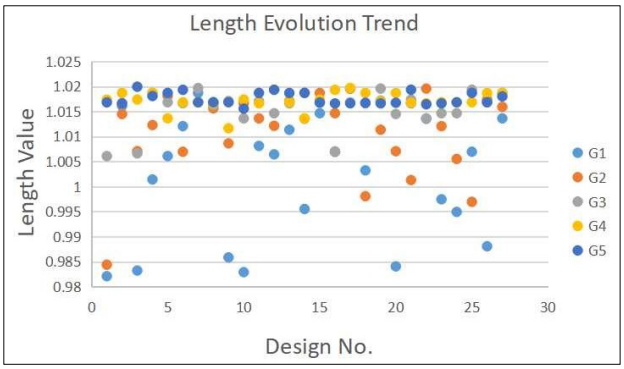


(a) Length

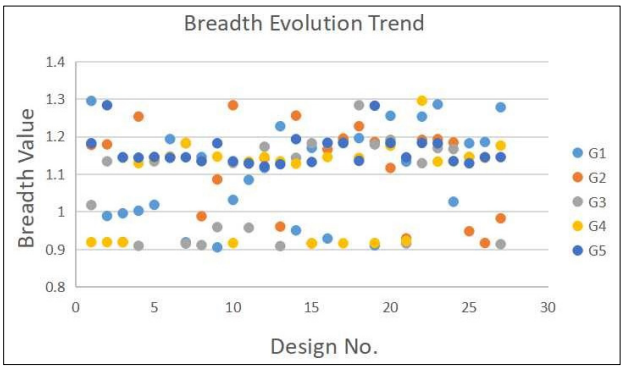


(b) Breadth

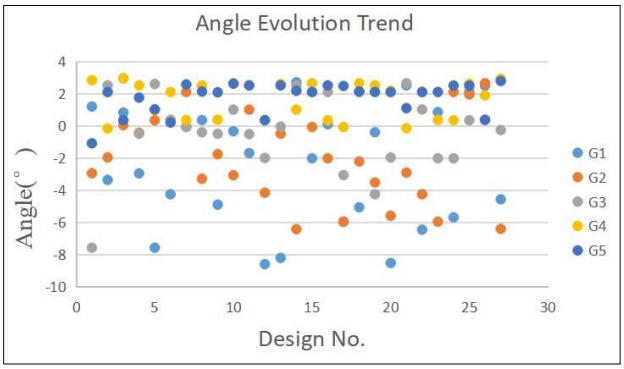


(c) Angle

**Fig. 9** Design variables evolution in 5 generations

### 4.2 Bow Part Optimization

The bow part was modified by using the Lackenby method to shift the section curve, and the design variable was $\Delta LCB$. A total of 9 different plans from the Lackenby method were computed, and the optimized demi-hull form was obtained. Fig. 10 shows a flow chart of choosing the optimal demi-hull.

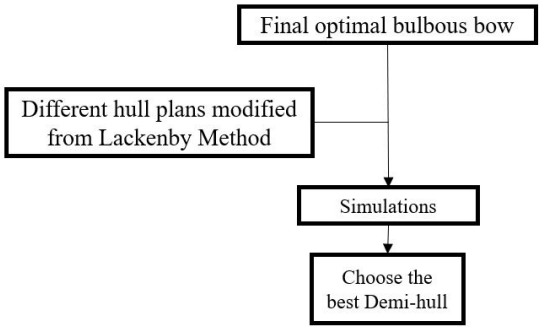


**Fig. 10** Process of choosing the optimal demi-hull

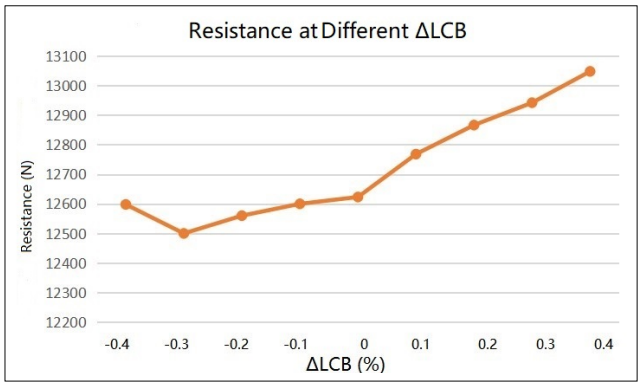


**Fig. 11** Resistance for different bow part plans at *Fn* 0.73

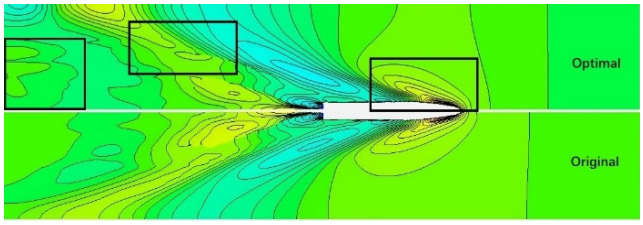


**Fig. 12** Wave pattern comparison between original and optimal hull at design speed.

Fig. 11 shows the simulation results of the 9 different hull forms from the Lackenby method. The results show that the resistance was reduced by about 1% when the longitudinal center of buoyancy was moved backward by 0.3%.

The wave pattern comparison is shown in Fig. 12. The 3 main differences are pointed out with 3 black squares. The wave pattern at the bow of the optimal demi-hull is smaller, and the wave pattern in the far field of the optimal demi-hull is lower than the original one.

## 5. Optimization of Distance Between Demi-hulls

According to Millward (1992), the effect on the resistance coefficient is separated into three parts. The effect of the distance has no rules to follow when *Fn* is in the range of around 0.2 to 0.4. In the *Fn* range of 0.4 to 0.7, the distance between the demi-hulls has a positive correlation with the total wave-making resistance. When the distance between the demi-hulls is larger, the negative interference of the two demi-hulls is weaker. When *Fn* is beyond 0.7, the 2 lines of the resistance coefficient begin to cross, which means the effect of the distance also has no rules to follow. However, we do know that there is a potential optimal distance.

With the design speed of the catamaran (*Fn*=0.73), 19 different cases of separation between the two demi-hulls were generated and simulated. The results are shown in Fig. 13. The resistance of the catamaran is smallest when *S/L* is 0.42. This means the optimal distance of the two demi-hulls is 8.4 m. *S* is the distance between the

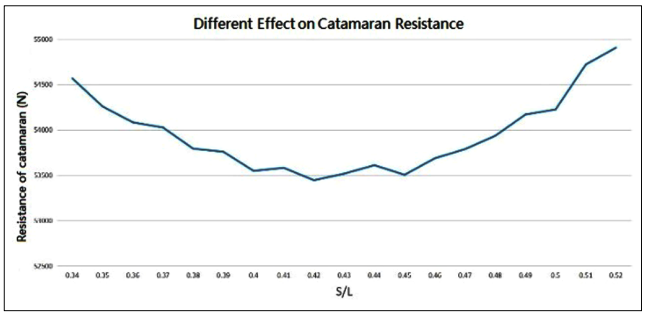


**Fig. 13** Resistance of the catamaran for different separation plans

two demi-hulls, and *L* is the length of the catamaran. The results show that the distance between the demi-hulls of the catamaran does have an optimal value in this case.

## 6. Conclusion

The hull form of a high-speed catamaran was optimized by coupling the software CAESES and STAR-CCM+. The resistance simulation was carried out using the RANS method, and the fluid model was set to inviscid to reduce the computing time. The bulbous bow of the demi-hull was optimized by a genetic algorithm, and the forms were generated by the FFD method for various lengths, breadths, and angles. The bow part between the bulbous bow and the mid-ship was then optimized by simulating 9 different hull forms that were modified by the Lackenby method while keeping the displacement of the demi-hull constant. The design variable was $\Delta LCB$. The distance between the two demi-hulls was then optimized by simulating 19 different separation cases.

The wave-making resistance of the optimal demi-hull was reduced by 6.2% compared to the original demi-hull. The total resistance of the catamaran had optimal performance when the distance between the two demi-hulls was 8.4 m ($S/L$=0.42). The results showed that this optimization loop is feasible and efficient. The NSGA-II algorithm was used for only the bulbous bow optimization, and the bow part was optimized independently. However, the bulbous bow and the bow part affect each other. Future work will focus on optimizing the bulbous bow and bow part of the hull together to find the best combination of the two parts.

## Acknowledgments

This work was supported by a Research Grant of Pukyong National University (2020Year).

## References

Chrismianto, D., & Kim, D.J. (2014). Parametric Bulbous Bow Design Using the Cubic Bezier Curve and Curve-plane Intersection Method for the Minimization of Ship Resistance in CFD. Journal of Marine Science and Technology, 19(4), 479-492. https://doi.org/10.1007/s00773-014-0278-x

Han, S.H., Lee, Y.S., & Choi, Y.B. (2012). Hydrodynamic Hull form Optimization Using Parametric Models. Journal of Marine Science and Technology, 17, 1-17. https://doi.org/10.1007/s00773-011-0148-8

Huang, F.X., Wang, L.J., & Yang, C. (2016). A New Improved Artificial Bee Colony Algorithm for Ship Hull form Optimization. Engineering Optimization, 48(4), 672-686. https://doi.org/10.1080/0305215X.2015.1031660

Kim, Y.C., Kim, Y., Kim, J., & Kim, K.S. (2019). Application of the Overset Grid Scheme (Suggar++) for Flow Analysis around a Ship. Journal of the Society of Naval Architects of Korea, 56(1), 47-57. https://doi.org/10.3744/SNAK.2019.56.1.047

Kostas, K.V., Ginnis, A.I., Politis, C.G., & Kaklis, P.D. (2015). Ship-hull Shape Optimization with a T-spline Based BEM Iso-geometric Solver. Computer Methods in Applied Mechanics and Engineering, 284, 611-622. https://doi.org/10.1016/j.cma.2014.10.030

Luo, W., & Lan, L. (2017). Design Optimization of the Lines of the Bulbous Bow of a Hull Based on Parametric Modeling and Computational Fluid Dynamics Calculation. Mathematical and Computational Applications, 22(4), 1-12. https://doi.org/10.3390/mca22010004

Lackenby, H. (1950). On the Systematic Geometrical Variation of Ship Forms. RINA Transactions, 92, 289-309.

Millward, A. (1992). The Effect of Hull Separation and Restricted Water Depth on Catamaran Resistance. Transactions of the Royal Institute of Naval Architects, 134, 341-349.

Park, K., Kim, D.J., Kim, S.Y., & Rhee, S.H. (2019). A Study on the Resistance Performance and Flow Pattern of High Speed Planing Hull using CFD. Journal of the Society of Naval Architects of Korea, 56(1), 23-33. https://doi.org/10.3744/SNAK.2019.56.1.023

Thomas, W.S., & Scott, R.P. (1986). Free-form Deformation of Solid Geometric Models. Proceedings of SIGGRAPH - Special Interest Group on GRAPHics and Interactive Techniques, 20, 151-159.

Zhang, S.L., Zhang, B.J., Tezdogan, T., Xu, L., & Lai, Y.Y. (2018). Computational Fluid Dynamics-based Hull form Optimization Using Approximation Method. Engineering Applications of Computational Fluid Mechanics, 12(1), 74-88. https://doi.org/10.1080/19942060.2017.1343751

## Author ORCIDs


| Author name | ORCID |
|---|---|
| Zhang Yongxing | 0000-0003-2610-6594 |
| Kim, Dong-Joon | 0000-0003-0730-8721 |

KSOE
Review Article

**Journal of Ocean Engineering and Technology** 34(4), 277-284 August, 2020
https://doi.org/10.26748/KSOE.2020.018

pISSN 1225-0767
eISSN 2287-6715

# Underwater Acoustic Research Trends with Machine Learning: Active SONAR Applications

Haesang Yang[1], Sung-Hoon Byun[2], Keunhwa Lee[3], Youngmin Choo[4] and Kookhyun Kim[5]

[1]*Research Professor, Department of Naval Architecture & Ocean Engineering, Seoul National University, Seoul, Korea*
[2]*Principal Researcher, Ocean System Engineering Research Division, Korea Research Institute of Ships & Ocean Engineering, Daejeon, Korea*
[3]*Associate Professor, Department of Defense System Engineering, Sejong University, Seoul, Korea*
[4]*Assistant Professor, Department of Defense System Engineering, Sejong University, Seoul, Korea*
[5]*Associate Professor, School of Naval Architecture & Ocean Engineering, Tongmyong University, Busan, Korea*

**KEY WORDS:** Underwater acoustics, Active SONAR system, Machine learning, Deep learning, Signal processing, Active target classification

**ABSTRACT:** *Underwater acoustics, which is the study of phenomena related to sound waves in water, has been applied mainly in research on the use of sound navigation and range (SONAR) systems for communication, target detection, investigation of marine resources and environments, and noise measurement and analysis. The main objective of underwater acoustic remote sensing is to obtain information on a target object indirectly by using acoustic data. Presently, various types of machine learning techniques are being widely used to extract information from acoustic data. The machine learning techniques typically used in underwater acoustics and their applications in passive SONAR systems were reviewed in the first two parts of this work (Yang et al., 2020a; Yang et al., 2020b). As a follow-up, this paper reviews machine learning applications in SONAR signal processing with a focus on active target detection and classification.*

## 1. Introduction

Underwater acoustics is the study of the phenomena related to the generation, propagation, transmission and reception of sound waves in water. It is applied in a variety of underwater activities such as underwater communication, target detection, and investigation of marine resources and environments, mainly using sound navigation and ranging (SONAR) systems. The main objective of underwater acoustic remote sensing is to indirectly acquire information on a target of interest using acoustic data. To extract information from acoustic data, machine learning, which has been recently attracting significant attention, has been employed in a variety of ways. The machine learning techniques mainly used in underwater acoustics and their applications in passive SONAR systems are introduced in the first two parts of this work, respectively (Yang et al., 2020a; Yang et al., 2020b). In the review article, we review the research on the application of machine learning in active SONAR systems for target detection and classification.

## 2. Active SONAR Signal Processing

The passive SONAR-based target localization technique discussed in the previous part (Yang et al., 2020b) can be applied to active SONAR systems without significant modification. However, a key difference between passive and active SONAR target detection is that, in passive SONAR systems, sounds generated by targets of interest such as ships and fish are received, whereas in active SONAR systems, the observer directly transmits a signal and receives a scattered signal from the target. Consequently, for active SONAR detection, various techniques have been developed to utilize the characteristics of the sound source or those of a scattered signal depending on the properties of the target, unlike in the case of passive SONAR detection. This review article is aimed primarily at discussing active target detection and classification.

### 2.1 Active Target Detection and Classification

Traditional active SONAR signal processing can be largely classified into the processes of (1) detecting the signal of interest, (2)

Received 4 March 2020, revised 11 April 2020, accepted 13 April 2020
Corresponding author Youngmin Choo: +82-2-6935-2532, ychoo@sejong.ac.kr

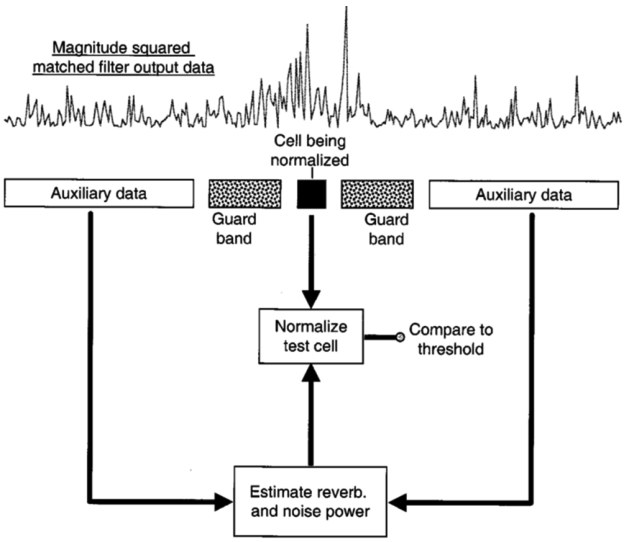


**Fig. 1** Flow diagram of the normalization scheme depicting how the reverberation and background noise power is estimated from leading and lagging windows of auxiliary data. A conventional matched filter detector would compare the normalized data to a threshold to declare detection (Abraham and Willett, 2002).

identifying (or classifying) the signal of interest, and (3) tracking the signal of interest (Abraham, 2019). In particular, because active SONAR transmits a signal and detects a scattered signal from the target, noise that differs from the transmitted signal is removed before signal detection is performed, by using a matched filter after beamforming. However, because the signal scattered by the rough interface or underwater scatterer is also similar to the sound source signal, it cannot be conveniently removed even using a matched filter. In addition, the clutter signal scattered by the local domain, such as a sea floor outcrop, exhibits a behavior similar to that of the target signal. In this manner, when an active SONAR is in operation, a false alarm can be triggered by a scattered/clutter signal other than the target signal. Consequently, the target detection performance deteriorates.

In the typical target detection process, the target is identified based on a threshold. In particular, the cell-averaging constant false alarm rate (CFAR) is a tool for normalizing the signal considering the noise effect around the target signal of interest and for applying a threshold to increase the target detection performance (Fig. 1) (Abraham, 2019; Abraham and Willett, 2002). In addition, in another technique for improving the performance, a variable that incorporates the variation of the signal-to-noise ratio over time is designed to explore a section in which a scattered signal by the target exists (Abraham and Willett, 2002).

In the aforementioned active SONAR signal processing, after the detection of the signal of interest, a post-processing technique such as clustering is applied to remove the clutter signals that exhibit a behavior similar to that of the target signal as much as possible. Finally, a SONAR operator manually determines whether the signal is the target or clutter by using the visual (e.g., spectrogram) or auditory (e.g., timbre) information of the signal. In an environment where clutter signals are likely to occur, such as shallow waters, the number of tasks for the SONAR operator increases. To reduce this workload, studies on the application of machine learning to active target signal detection have begun. In particular, the following techniques have been proposed to reduce the amount of computation. First, a target signal candidate group is searched by a conventional target detection method. In addition, a detector that has been trained with the target signal characteristics of active SONAR data is applied to determine whether the detected signal is the target signal (Young and Hines, 2007). However, if the machine learning-based target signal classifier is applied directly to the entire acquired signal rather than being limited to the first detected target signal, the detection and classification steps of the conventional active SONAR signal processing can be integrated into one process (Shin et al., 1997). In this regard, machine learning-based target detection and machine learning-based target classification are used without distinction in this review article.

Gorman and Sejnowski (1988b) conducted the first classification of target signals by applying machine learning in underwater acoustics. In their studies, a metal cylinder and a cylindrical rock were selected as the target and the clutter, respectively. The target signals and clutter-scattered signals were measured according to the aspect angles. In particular, the linear frequency modulation signal was used as the sound source signal in their study. Based on the concept that the frequency variation of a scattered signal over time can be observed with a short-time Fourier transform, a spectral envelop displaying the frequency energy according to the observation time was used as the input value of the neural network. In addition, they experimentally demonstrated that the targets can be detected with a high and stable classification performance (that is, the effect of the initial value of an irregularly generated neural network is marginal) if the scattered signal of various aspect angles is included in the training data and the training is performed using a hidden layer and a neural network with a sufficient number of neurons. Furthermore, Gorman and Sejnowski (1988a) attempted to describe the neural network's classification process for target signals (using weights of a hidden layer and neurons activated thereby) in association with the scattered signal's characteristics (bandwidth and onset/decay characteristics).

As described above, the machine learning-based target detection technique that applies the classify-before-detect strategy must utilize comprehensive information of the observation signal similar to how a SONAR operator uses various information to determine the target. In particular, to reduce false alarms caused by clutter signals, raw data must be converted to a domain that makes it convenient to distinguish target signals from clutter signals (Fig. 2). In this regard, as a representative example, Shin et al. (1997) observed and analyzed different target signals with respect to the shape or internal structure of the target. Furthermore, features effective for target/clutter signal identification were extracted to improve the target detection performance. These included time variations, frequency spectra,

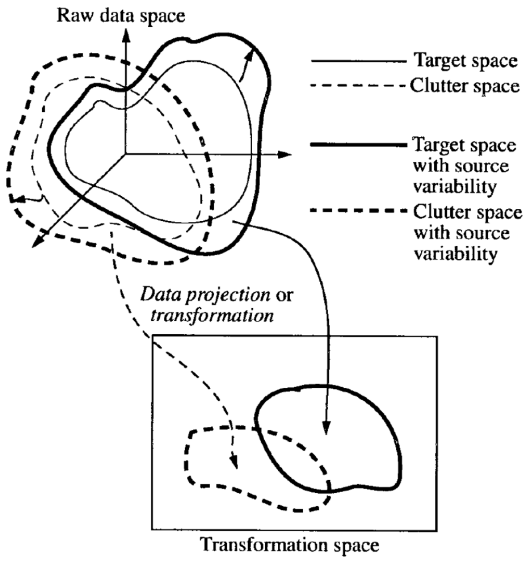


**Fig. 2** Selection of appropriate projection spaces can improve clutter-reduction performance. Stochastic impulsive sources generally enlarge the target and clutter spaces spanned by raw time-domain data. The main goal of projection-space investigation is to represent both classes (i.e., target and clutter) compactly in the transformation space for improved class separation and lower false alarm rate (Shin et al., 1997).

frequency variation over time, and auditory characteristics of the observed signals. Then, features optimized for target signal classification were selected and combined with several machine learning algorithms, including neural networks, to detect the target signals. This method displayed performance superior to that of the conventional method by producing fewer false alarms and higher target signal classification accuracy.

It was mentioned earlier that target detection becomes challenging owing to signals scattered by various underwater clutter. Nevertheless, the SONAR operator is trained to recognize the differences between the scattered target signal and the scattered clutter signal. Based on this, Young and Hines (2007) proposed a target signal detector reflecting the SONAR operator's auditory perception. In particular, acoustic cognitive features (timbre characteristics), which are the main aspects of interest in musical acoustics, were extracted from the signal duration containing the target or clutter signal. That is, the equivalent rectangular bandwidth (ERB) scale is defined based on the human tendency of analyzing the low frequency band in more detail while detecting a sound. In this nonlinear frequency scale, when a gammatone filter is applied to the original signal, the filtered time series signal can be obtained in each frequency band. The time delay between the start (or end) of the echo and the peak of the temporal envelop and the slope of the line joining the start (or end) of the echo and the peak of the temporal envelop obtained through the above process were used as features (Fig. 3(a)). In addition, the energy in each frequency band of the signal can be calculated through the above process, and a perceptual loudness function can be derived through the

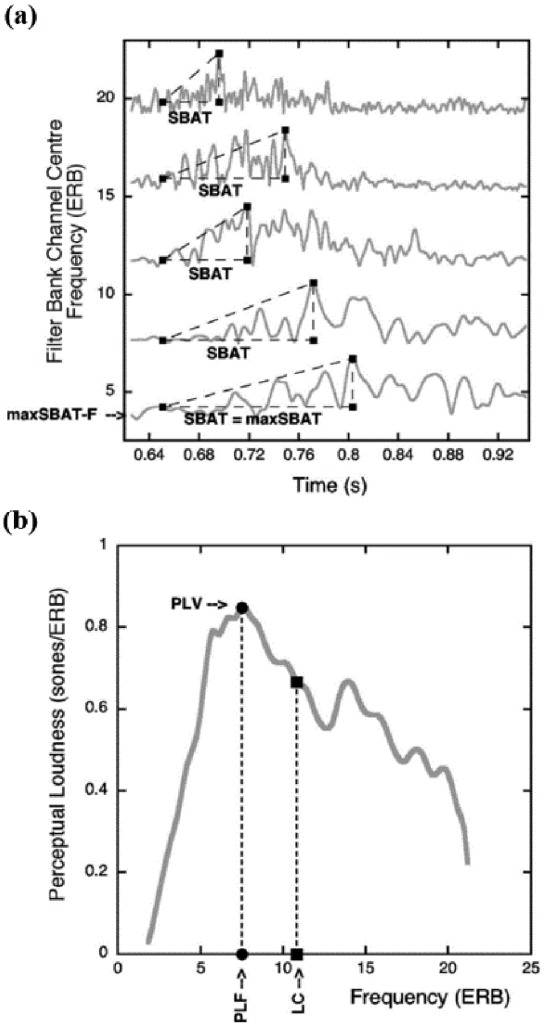


**Fig. 3** (a) Extraction of sub-band attack time feature values from several channels of the auditory filter bank; the lowest trace exhibits the maximum sub-band attack time (maxSBAT) and the frequency of this filter bank channel corresponds to maxSBAT-F. (b) Extraction of peak loudness frequency (PLF), peak loudness value (PLV), and loudness centroid (LC) feature values from a perceptual loudness function (Young and Hines, 2007).

calculation (Fig. 3(b)). The feature vectors reflecting the auditory perception characteristics of humans were defined by combining the peak value of this function and the corresponding frequency with the previously designed features. Then, to avoid having an excessive number of dimensions, elements effective for target/clutter classification were selected from among the feature vector elements. Furthermore, the feature vector dimension was reduced through principal component analysis, and the resulting vectors were used as final input values. In this manner, the characteristics reflecting human auditory perception characteristics were combined with a simple machine learning algorithm such as a Gaussian classifier to classify target signals such as marine structures. Thereby, the target signals differing from clutter signals were classified with high accuracy.

The performance of the target signal classifier reflecting the timbre characteristics is affected by the wave propagation phenomenon depending on the ocean environment, noise, and time-varying ocean environment. In this regard, Murphy and Hines (2014) tested the proposed target signal classifier for robustness against variations in the ocean environment, using target/clutter signals (Clutter07/Clutter09) measured in different environments. In this case, apart from characteristics of the ocean environment (such as underwater sound speed or noise), the experimental design factors including the transmitted signal for measuring the target/cutter signal, ship route, and object used as the target/clutter were set identically in both of experiments.

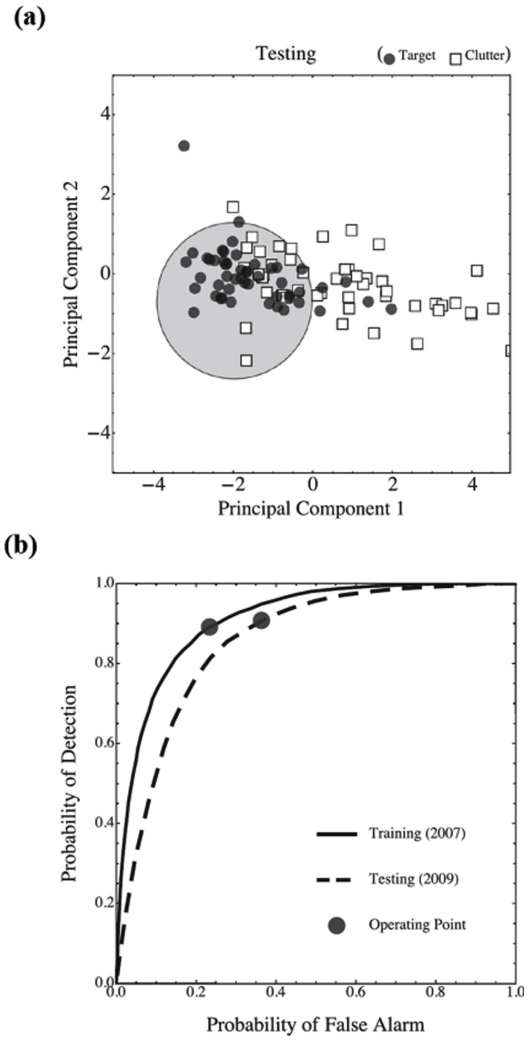


**Fig. 4** (a) Scatter plot of testing echoes in the reduced (two-dimensional) feature space. The circular gray target region contains 90% of the target echoes (black dots) and the surrounding white clutter region contains 64% of the clutter echoes (outlined white squares). (b) ROC curves corresponding to the training dataset (solid line) and testing dataset (dashed line). The training AUC value is 0.91 (outstanding discrimination), and the testing AUC value is 0.86 (excellent discrimination). The Bayes-rate operating point (black circle) is shown at (0.23, 0.89) on the training curve and at (0.36, 0.90) on the testing curve (Murphy and Hines, 2014).

In their study, the Gaussian classifier was used as a classifier similarly as in the previous study (Young and Hines, 2007). Furthermore, the data obtained from Clutter07 were used for training. The performance of the classifier can be evaluated through a receiver-operating-characteristic (ROC) curve displaying the relationship between the probability of detection and the probability of false alarm. The target classifier performance is determined by calculating the area under the ROC curve (AUC). The AUC has a value between zero and one. The closer the value is to one, the higher is the target classification performance. A value of 0.91 was obtained when the AUC was calculated by applying the classifier trained with Clutter07 data to data from among Clutter07 not used for training. This demonstrates that the timbre-based target detector displays remarkable classification performance. Furthermore, a classifier trained with Clutter07 data was applied to Clutter09 data to obtain an AUC value of 0.86 (Fig. 4). Although this value is low compared to the result of using test data obtained in an environment identical to that of the training data, it evidently exhibits remarkable classification performance.

Another related study tested the auditory perception capability of humans to classify target/clutter signals and compared this capability with the performance of a timbre-based target signal classifier (Allen et al., 2011). The subjects participating in the target/clutter signal classification experiment were able to distinguish the target signal from the clutter signal while using acoustic signals in all the frequency bands. However, when the experiment was performed with scattered signals that removed the signal component of the low frequency band, the target classification rate was substantially reduced. However, the timbre-based target signal classifier showed similar performance to those of most subjects. In particular, it was observed that unlike humans, the performance of the classifier slightly decreased when the signal bandwidth was limited.

A study that analyzed the probability distribution characteristics of clutter signals that limit the operation of active SONAR and applied them to classification is described as follows. Gelb et al. (2010) distinguished between target and clutter using the distribution characteristics of the matched clutter signal according to space–time. The clutter signals can be divided into bottom-like, compact stationary, and compact nonstationary classes. In this study, the probability distribution of the observed signal according to the above classes was derived by applying K-distribution and generalized Pareto distribution to unthresholded data and thresholded data, respectively. At this time, if the parameters of each distribution are adjusted and fitted to the observed signal, the distribution of parameters depends on the clutter class. Meanwhile, it is possible to directly calculate cumulants from the locally observed signal according to the class. These cumulants are also distributed differently according to the clutter signal class. By combining this with a classifier that estimates a class based on the probability distribution of input features, such as a Gaussian mixture model, it was demonstrated that the clutter signal could be classified according to its class.

### 2.2 Seafloor Target Detection and Classification

Active SONAR can be used to detect targets on the seafloor or buried in sediment, as well as underwater targets. Early statistical studies on the classification of buried targets using the monostatic SONAR system were performed to develop a target classification technique using signals received from different aspect angles of the target by utilizing one sensor. Runkle et al. (1999a; 1999b) extracted features from the signals scattered from the target using a matching pursuit technique, one of the sparse representation algorithms, and classified five types of objects using a hidden Markov model. In addition, at approximately the same time, the results of applying pattern recognition techniques different from those used in the above study to detect buried targets were also published (Trucco and Pescetto, 2000; Trucco, 2001). They segmented the beamformed signals into partially overlapping frames, projected them into the time-frequency space, and classified the extracted features using a multivariate Gaussian classifier. In particular, they demonstrated that this method performed well even with the data obtained by an active SONAR system operating remotely with a low grazing angle.

Azimi-Sadjadi, et al. (2000) applied wavelet packet decomposition and linear predictive coding to backscattered target/clutter signals to extract features that can conveniently classify target/clutter, and they combined them with a neural network to obtain a classifier that can classify a target signal with high performance. At this time, the target signals comprised a signal scattered from a bullet-shaped metal object and one from a plastic material object with a truncated cone shape. The clutter signals were scattered from four types of clutters: a water-filled drum, an irregularly shaped limestone rock, soft granite, and water-logged logs. These targets and clutters were placed in a water tank environment with a limited size. The target/clutter backscattered signals were measured according to the aspect angle. Then, to generate a realistic target/clutter backscattered signal, preprocessing was applied to remove the interference of signals from multiple paths in a limited tank environment. Subsequently, a simulated reverberation signal was added. Furthermore, in their study, pre-processed observation signals and transmission signals were divided into multiple bands using wavelet packet decomposition. Moreover, cross-correlation of observation signals and transmission signals in each segmented band was performed, and the results were expressed using an autoregressive (AR) model. Here, when high-dimensional feature vectors are generated by combining AR coefficients derived according to each segmented band, features effective for convenient identification of target/clutter signals are extracted using the Fisher discriminant function. In addition, the dimension of the input feature vectors is reduced. Training and test data were sorted according to aspect angle, and performance was evaluated by training a two-layer neural network using the aforementioned feature vectors as inputs. The classifier proposed in their study exhibited performance superior to those of other existing classifiers. In particular, the results obtained by combining the results of backscattered signal classification at adjacent aspect angles showed higher performance improvements over those using the backscattered signals of a single aspect angle.

Azimi-Sadjadi et al. (2002) improved the previously developed target classifier further and proposed an adaptive target classifier that can achieve high performance even when using test data obtained in a different environment from the ocean environment of the training data. Here, the basic classifier used as a non-adaptive classifier is identical to the aforementioned two-layer neural network. The adaptive target classifier proposed in this study transforms the input vector into a vector insensitive to variations in the environment by adding a linear mapping between the input and the hidden layer of the non-adaptive classifier. In this process, the non-adaptive classifier is fixed, and the weight for linear mapping is learned. In particular, the difference between the output values of the adaptive and non-adaptive classifiers is increased using K-nearest neighbors (K-NN) and a 2-D sigmoid cost function. In their study, the effectiveness of the proposed method was verified by using test data having reverberation levels different from those of the training data. The proposed adaptive classifier exhibited higher performance in an environment with a reverberation level higher than that of the existing classifier.

Meanwhile, while developing a target signal classifier, even when the same input vector is used, classification performance may vary according to the machine learning algorithm used and according to the characteristic of the input data. Li et al. (2004) combined the input vectors defined by Azimi-Sadjadi et al. (2000) with multivariate Gaussian, K-NN, probabilistic neural networks, and support vector machines (SVMs) in addition to neural networks. They also compared and analyzed their performances. Among these, the SVM-based target signal classifier exhibited the most stable and remarkable performance. In addition, Yao et al. (2002) compared the results of classification by using the classifier developed by Azimi-Sadjadi et al. (2000) for different data having bandwidths of 40 kHz and 80 kHz. The result was presented in terms of ROC, error locations, and generalization and robustness for the noise. In their study, the result obtained using data with the 80 kHz bandwidth showed higher classification performance. Accordingly, a sub-band fusion technique based on the contribution of each band with subdivision of the broadband data was also proposed.

### 2.3 AUV and Automatic Target Recognition System

Underwater image information obtained via sensors such as side scan SONAR or synthetic aperture SONAR is generally used when classifying targets on the seafloor, such as mines, using an autonomous underwater vehicle (AUV). Recently, several studies have been presented that produced high-performance, high-resolution image processing and classification results through the application of machine learning for automatic target recognition (Isaacs, 2015; Kriminger et al., 2015; Myers and Fawcett, 2010). However, these methods have a limitation in that real-time processing is challenging. In particular, targets buried in the sediment cannot be classified following these approaches. In this regard, Fischell and Schmidt (2015) proposed a machine learning-based signal processing technique

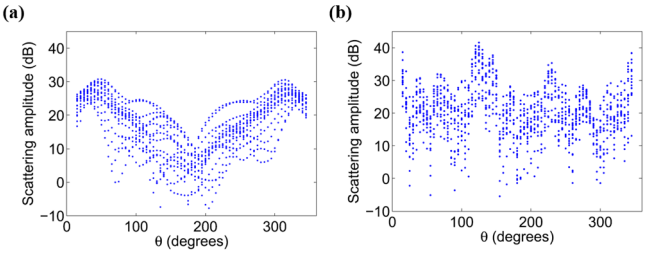


**Fig. 5** Simulated scattering amplitude dependence on angle for spherical and cylindrical targets. is calculated by setting the target at (0, 0) and the source at (-60, 0) such that the source is at 180°. Amplitudes shown here are for multiple receiver depths and ranges to the target. (a) Spherical target. (b) Cylindrical target (Fischell and Schmidt, 2015).

capable of real-time target classification in a system installed on an AUV. In general, when a signal emitted from a fixed sound source is scattered by a target, the scattering intensity depends on the angle between the line joining the sound source and target and that joining the target and receiver (azimuthal angle). Here, the intensity of scattered radiation for a specific target varies only marginally according to the distance between the sound source and receiver or the depth of the receiver. However, it varies substantially according to the azimuthal angle. In addition, the scattering radiation pattern displayed for all the azimuthal angles is highly dependent on the type of target (Fig. 5). Therefore, in their study, an input vector for machine learning was defined by using a bistatic scattering radiation pattern. Furthermore, it was combined with SVM to perform classification into spherical and cylindrical targets. The scattering radiation pattern used for training was normalized using the mean and standard deviation of the scattering intensity and discretized at regular azimuthal angle intervals. In this case, if multiple scattering intensities exist in the same discrete azimuthal angle, the feature value of the corresponding azimuthal angle is calculated as the median value. In this manner, scattering radiation patterns for all the azimuthal angles discretized at specific intervals can be represented using vectors, which can be used as inputs to the SVM. This target classifier was tested according to the discrete interval of the azimuthal angle and the number of data. It was verified that real-time target shape classification is possible using data (BayEx'14) obtained by an AUV in a real underwater environment.

Meanwhile, the target scattering amplitude according to the azimuthal angle depends on the properties of the seafloor, depth of the surface layer of the marine sediments, and depth of burial of the target. Therefore, the performance of the target classifier may deteriorate when the ocean environment and the experimental conditions for obtaining the training data differ from those of the test data. To address this problem, Fischell and Schmidt (2017a) analyzed the performance of the sphere/cylinder target classifier according to the inconsistencies between the ocean environment and the experimental conditions and proposed a method to reduce the performance degradation. In particular, their study reduced the dependence on similar environmental variations by adding a process whereby the mean and variance of the vectorized discrete scattering radiation pattern became zero and one, respectively. In addition, in this study, bistatic scattering tendency according to the seafloor properties, surface depth of marine sediments, and depth of buried targets were calculated using a simulator and utilized as training data for learning. The actual measurement data were used as test data. Then, it was verified that in the training environment with seafloor properties identical to those of the operating environment of the AUV, good classification performance was obtained even under conditions where the depth of the surficial sediment or the degree of buried targets were inconsistent. However, a rapid performance degradation of the classifier was observed when the seafloor properties differed from those in the environment for actual data acquisition. In this case, simulation was performed by varying the depth of the surface layer and that of the buried target, using these as training data to improve the classifier performance. It is considered that these improved results were achieved because various scattering tendencies and conditions were provided as observation information compared to the use of only specific conditions.

In the case of a cylindrical-shaped target, the scattering radiation pattern varies depending on the aspect angle between the axis of the target and the line joining the sound source and target. Fischell and Schmidt (2017b) proposed a method for estimating the aspect of a target from the scattered signal of the target measured using an AUV by utilizing a scattering radiation pattern that depends on the aspect angle. In this technique utilizing SVM regression, the simulator generated normalized scattering radiation pattern according to the target's aspect angle and trained it. Even for the cases when the ocean environment of the simulation did not match the environment of actual test data acquisition, it was verified that the target aspect classifier trained with simulation data derived a specific aspect angle with high accuracy when feature vectors were constructed using a sufficient number of measurement signals.

## 3. Conclusion

This review article summarizes the trend in the recent application of the highly advanced machine learning technology for target detection and classification using an active SONAR system. Depending on the characteristics of the active SONAR system that utilizes the signal transmitted from the sound source and scattered by the target, existing conventional signal processing techniques, acoustic modeling, and machine learning complement each other and produce improved results in terms of various aspects such as sound source characteristics, target properties, and target/clutter signal characteristics. The machine learning-based active target detection secured sufficient information on the target by utilizing the signals received from various aspect angles of the target and the feature factors extracted from the time-frequency space. Hence, it is possible to achieve significant reduction in the number of false alarm caused by clutter with signal characteristics similar to those of the target. In addition, it is likely that

human error from individual experience, level of proficiency, and skill differences would be significantly reduced using the automatic target detection technology, to be developed in the future, through the use of target detection techniques that reflect and incorporate human auditory perception capability.

## Acknowledgments

This research was supported by a grant from Endowment Project funded by KRISO (PES3570).

## References

Abraham, D.A. (2019). Underwater Acoustic Signal Processing: Modeling, Detection, and Estimation. Springer.

Abraham, D.A., & Willett, P.K. (2002). Active Sonar Detection in Shallow Water Using the Page Test. IEEE Journal of Oceanic Engineering, 27(1), 35-46. https://doi.org/10.1109/48.989883

Allen, N., Hines, P.C., & Young, V.W. (2011). Performances of Human Listeners and an Automatic Aural Classifier in Discriminating between Sonar Target Echoes and Clutter. The Journal of the Acoustical Society of America, 130(3), 1287-1298. https://doi.org/10.1121/1.3614549

Azimi-Sadjadi, M.R., Yao, D., Huang, Q., & Dobeck, G.J. (2000). Underwater Target Classification Using Wavelet Packets and Neural Networks. IEEE Transactions on Neural Networks, 11(3), 784-794. https://doi.org/10.1109/72.846748

Azimi-Sadjadi, M.R., Yao, D., Jamshidi, A.A., & Dobeck, G.J. (2002). Underwater Target Classification in Changing Environments Using an Adaptive Feature Mapping. IEEE Transactions on Neural Networks, 13(5), 1099-1111. https://doi.org/10.1109/TNN.2002.1031942

Fischell, E.M., & Schmidt, H. (2015). Classification of Underwater Targets from Autonomous Underwater Vehicle Sampled Bistatic Acoustic Scattered Fields. The Journal of the Acoustical Society of America, 138(6), 3773-3784. https://doi.org/10.1121/1.4938017

Fischell, E.M., & Schmidt, H. (2017a). Environmental Effects on Seabed Object Bistatic Scattering Classification. The Journal of the Acoustical Society of America, 141(1), 28-37. https://doi.org/10.1121/1.4972273

Fischell, E.M., & Schmidt, H. (2017b). Supervised Machine Learning for Estimation of Target Aspect Angle from Bistatic Acoustic Scattering. IEEE Journal of Oceanic Engineering, 42(4), 759-769. https://doi.org/10.1109/JOE.2017.2650759

Gelb, J.M., Heath, R.E., & Tipple, G.L. (2010). Statistics of Distinct Clutter Classes in Midfrequency Active Sonar. IEEE Journal of Oceanic Engineering, 35(2), 220-229. https://doi.org/10.1109/JOE.2009.2031547

Gorman, R.P., & Sejnowski, T.J. (1988a). Analysis of Hidden Units in a Layered Network Trained to Classify Sonar Targets. Neural Networks, 1(1), 75-89. https://doi.org/10.1016/0893-6080(88)90023-8

Gorman, R.P., & Sejnowski, T.J. (1988b). Learned Classification of Sonar Targets Using a Massively Parallel Network. IEEE Transactions on Acoustics, Speech, and Signal Processing, 36(7), 1135-1140. https://doi.org/10.1109/29.1640

Isaacs, J.C. (2015). Sonar Automatic Target Recognition for Underwater UXO Remediation. Proceedings of the IEEE Conference on Computer Vision and Pattern Recognition (CVPR) Workshops, 134-140.

Kriminger, E., Cobb, J.T., & Principe, J.C. (2015). Online Active Learning for Automatic Target Recognition. IEEE Journal of Oceanic Engineering, 40(3), 583-591. https://doi.org/10.1109/JOE.2014.2340353

Li, D., Azimi-Sadjadi, M.R., & Robinson, M. (2004). Comparison of Different Classification Algorithms for Underwater Target Discrimination. IEEE Transactions on Neural Networks, 15(1), 189-194. https://doi.org/10.1109/TNN.2003.820621

Murphy, S.M., & Hines, P.C. (2014). Examining the Robustness of Automated Aural Classification of Active Sonar Echoes. The Journal of the Acoustical Society of America, 135(2), 626-636. https://doi.org/10.1121/1.4861922

Myers, V., & Fawcett, J. (2010). A Template Matching Procedure for Automatic Target Recognition in Synthetic Aperture Sonar Imager. IEEE Signal Processing Letters, 17(7), 683-686. https://doi.org/10.1109/LSP.2010.2051574

Runkle, P., Bharadwaj, P., Couchman, L., & Carin, L. (1999a). Hidden Markov Models for Multi-aspect Target Identification. IEEE Transactions on Signal Processing, 47(7), 2035-2040. https://doi.org/10.1109/78.771050

Runkle, P., Carin, L., Couchman, L., Bucaro, J.A., & Yoder, T.J. (1999b). Multiaspect Identification of Submerged Elastic Targets via Wave-based Matching Pursuits and Hidden Markov Models. The Journal of the Acoustical Society of America, 106, 605−616. https://doi.org/10.1121/1.427029

Shin, F.B., Kil, D.H., & Wayland, R.F. (1997). Active Impulsive Echo Discrimination in Shallow Water by Mapping Target Physics-derived Features to Classifiers. IEEE Journal of Oceanic Engineering, 22(1), 66-80. https://doi.org/10.1109/48.557541

Trucco, A. (2001). Detection of Objects Buried in the Seafloor by a Pattern Recognition Approach. IEEE Journal of Oceanic Engineering, 26(4), 769-782. https://doi.org/10.1109/48.972118

Trucco, A., & Pescetto, A. (2000). Acoustic Detection of Objects Buried in the Seafloor. Electronics Letters, 36(18), 1595-1596. https://doi.org/10.1049/el:20001065

Yang, H., Lee, K., Choo, Y., Kim, K. (2020a). Underwater Acoustic Research Trends with Machine Learning: General Background. Journal of Ocean Engineering and Technology, 34(2), 147-154. https://doi.org/10.26748/KSOE.2020.015

Yang, H., Lee, K., Choo, Y., & Kim, K. (2020b). Underwater Acoustic Research Trends with Machine Learning: Passive SONAR Applications. Journal of Ocean Engineering and Technology, 34(3), 227-236. https://doi.org/10.26748/KSOE.2020.017

Yao, D., Azimi-Sadjadi, M.R., Jamshidi, A.A., & Dobeck, G.J. (2002). A Study of Effects of Sonar Bandwidth for Underwater Target Classification. IEEE Journal of Oceanic Engineering, 27(3), 619-627. https://doi.org/10.1109/JOE.2002.1040944

Young, V.W., & Hines, P.C. (2007). Perception-based Automatic Classification of Impulsive-source Active Sonar Echoes. The Journal of the Acoustical Society of America, 122(3), 1502-1517. https://doi.org/10.1121/1.2767001

## Author ORCIDs


| Author name | ORCID |
|---|---|
| Yang, Haesang | 0000-0001-7101-5195 |
| Byun, Sung-Hoon | 0000-0001-6971-7489 |
| Lee, Keunhwa | 0000-0003-4827-3983 |
| Choo, Youngmin | 0000-0002-9100-9494 |
| Kim, Kookhyun | 0000-0002-4214-4673 |

# Instructions for Authors

## General information

To submit a manuscript to the Journal of Ocean Engineering and Technology (JOET), it is advised to first carefully read the aims and the scope section of this journal, as it provides information on the editorial policy and the category of papers it accepts. Unlike many regular journals, JOET usually has no lag in acceptance of a manuscript and its publication. Authors that find a match with the aims and the scope of JOET are encouraged to submit as we publish works from all over the world. JOET adheres completely to guidelines and best practices published by professional organizations, including Principles of Transparency and Best Practice in Scholarly Publishing (joint statement by COPE, DOAJ, WAME, and OASPA (http://doaj.org/bestpractice) if otherwise not described below. As such, JOET would like to keep the principles and policies of those professional organizations during editing and the publication process.

## Research and publication ethics

Details on publication ethics are found in http://joet.org/authors/ethics.php. For the policies on research and publication ethics not stated in the Instructions, Guidelines on Good Publication (http://publicationethics.org/) can be applied.

## Requirement for membership

One of the authors who submits a paper or papers should be member of the Korean Society of Ocean Engineers (KSOE), except a case that editorial board provides special admission of submission.

## Publication type

Article types include scholarly monographs (original research articles), technical articles (technical reports and data), and review articles. The paper should have not been submitted to other academic journal. When part or whole of a manuscript was already published to conference papers, research reports, and dissertations, then the corresponding author should note it clearly in the manuscript.

## Copyright

After published to JOET, the copyright of manuscripts should belong to KSOE. A transfer of copyright (publishing agreement) form can be found in submission website (http://www.joet.org).

## Manuscript submission

Manuscript should be submitted through the on-line submission website (http://www.joet.org). The date that corresponding author submits a paper through on-line website is the official date of submission. Other correspondences can be sent by an email to the Editor in Chief or secretariat. The manuscript must be accompanied by a signed statement that it has been neither published nor currently submitted for publication elsewhere. The manuscript should be written in English or Korean. Ensure that online submission are in a standard word processing format (Hangul or MS Word are accepted). Ensure that graphics are high-resolution. Be sure all necessary files have been uploaded/ attached.

## Authors' checklist

Please refer to “Authors' Checklist” for details.

## Article structure

Manuscript must be edited in the following order: (1) Title, (2) Authors' names and affiliations, (3) Keywords, (4) Abstract, (5) Nomenclature (optional), (6) Introduction, (7) Main body (analyses, tests, results, and discussions), (8) Conclusions, (9) Acknowledgements (optional), (10) References, (11) Appendices (optional).

### *Abstract*

A concise and factual abstract is required. The abstract should state briefly the background, purpose and methods of the research, the principal results and conclusions. An abstract should be written in around 300 words. References are not cited in abstract whenever possible. Also, non-standard or uncommon abbreviations should be avoided, but if essential they must be defined at their first mention in the abstract itself.

### *Keywords*

Immediately after the abstract, provide a maximum of 5 or 6 keywords.

### *Unit*

Use the international system units(SI). If other units are mentioned, please give their equivalent in SI.

### *Equations*

All mathematical equations should be c1early printed/typed using well accepted explanation. Superscripts and subscripts should be typed clearly above or below the base line. Equation numbers should be given in Arabic numerals enclosed in parentheses on the right-hand margin.

### *Tables*

Tables should be numbered consecutively with Arabic numerals. Each table should be fully titled. All tables should be referred to in the texts.

### *Figures*

Figures should be numbered consecutively with Arabic numerals. Each figure should be fully titled. All figures should be referred to in the texts. All the illustrations should be of high quality meeting with the publishing requirement with legible symbols and legends.

### *Conflict of interest*

It should be disclosed here according to the statement in the Research and publication ethics regardless of existence of conflict of interest. If the authors have nothing to disclose, please state: “No potential conflict of interest relevant to this article was reported.”

### *Funding*

Funding to the research should be provided here. Providing a FundRef ID is recommended including the name of the funding agency, country and if available, the number of the grant provided by the funding agency. If the funding agency does not have a FundRef ID, please ask that agency to contact the FundRef registry (e-mail: fundref.registry@crossref.org). Additional detailed policy of FundRef description is available from http://www.crossref.org/fundref/. Example of a funding description is as follows:

The study is supported by the Inha University research fund (FundRef ID: 10.13039/501100002632), and the Korea Health Personnel Licensing Examination Institute research fund (FundRef ID: 10.13039/501100003647).

### *Acknowledgments*

Any persons that contributed to the study or the manuscript, but not meeting the requirements of an authorship could be placed here. For mentioning any persons or any organizations in this section, there should be a written permission from them.

### *References in text*

References in texts follow the APA style. Authors can also see how references appear in manuscript text through the 'Template'.

### *Reference list*

Reference list follows the APA style. Authors can see how references should be given in reference section through the 'Template'.

### *Appendices*

The appendix is an optional section that can contain details and data supplemental to the main text. If there is more than an appendix, they should be identified as A, B, C, etc. Formulae and equations in appendices should be given separate numbering: Eq. (A1), Eq. (A2), etc.; in a subsequent appendix, Eq. (B1) and so on. Similarly for tables and figures: Table A1; Fig. A1, etc.

### *ORCID (Open Researcher and Contributor ID)*

All authors are recommended to provide an ORCID. To obtain an ORCID, authors should register in the ORCID web site: http://orcid.org. Registration is free to every researcher in the world. Example of ORCID description is as follows:

Joonmo Choung: https://orcid.org/0000-0003-1407-9031

## Peer review and publication process

The peer review process can be broadly summarized into three groups: author process, review process, and publishing process for accepted submissions. General scheme is presented in Figure 1.

### *Check-in process for review*

If the manuscript does not fit the aims and scope of the Journal or does not adhere to the Instructions to Authors, it may be rejected immediately after receipt and without a review. Before reviewing, all submitted manuscripts are inspected by Similarity Check powered by iThenticate (https://www.crossref.org/services/similarity-check/), a plagiarism-screening tool. If a too high degree of similarity score is found, the Editorial Board will do a more profound content screening.

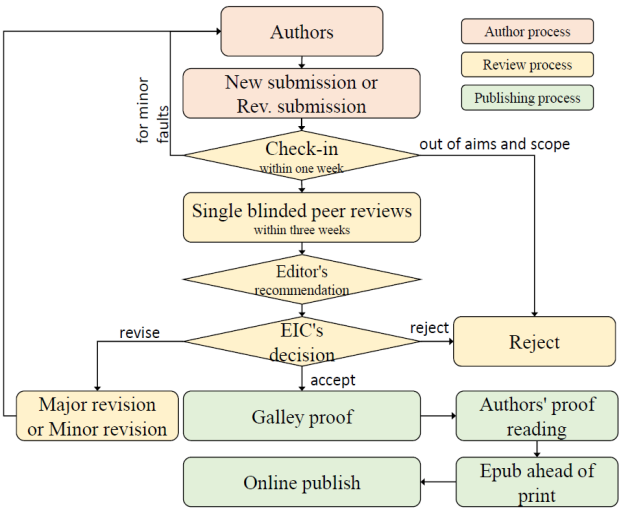


**Figure 1** Flow chart of the peer review and publication process of JOET

The criterion for similarity rate for further screening is usually 15%; however, rather than the similarity rate, the Editorial Board focuses on cases where specific sentences or phrases are similar. The settings for Similarity Check screening are as follows: It excludes quotes, bibliography, small matches of 6 words, small sources of 1%, and the Methods section.

### *Number of reviewers*

Reviewers will be selected from the list of reviewers. Manuscripts are then peer reviewed by at least 2 experts in the corresponding field, usually by 2.

### *Peer review process and the author response to the reviewer comments*

JOET adopts single blind review, which means that the authors do not know the identity of the reviews. All papers, including those invited by the Editor, are subject to peer review.

The review period is 4 weeks. Usually the first decision is made within a week after completion of the review. The Editorial Board's decision after the review will be one of followings: Accept, Minor revision, Major revision, or Rejection. The Editorial Board may request the authors to revise the manuscript according to the reviewers' comments. If there are any requests for revision of the manuscript by the reviewers, the authors should do their best to revise the manuscript. If the reviewer's opinion is not acceptable or is believed to misinterpret the data, the author should reasonably indicate that. After revising the manuscript, the author should upload the revised files with a separate response sheet to each item of the reviewer's commentary. The author's revisions should be completed within 3 months after the request. If it is not received by the due date, the Editorial Board will notify the author. To extend the revision period beyond 3 months, the author should negotiate that with the Editorial Board. The manuscript review process can be provided for up two rounds. If the authors wish further review, the Editorial Board may consider it. The Editorial Board will make a final decision on the approval of the submitted manuscript for publication and can request any further corrections, revisions, and deletions of the article text if necessary. Statistical editing is also performed if the data requires professional statistical review by a statistician.

***Processing after acceptance***

If the manuscript is finally accepted, the galley proof will be sent to the corresponding author after professional manuscript editing and English proofreading. Proofreading should be performed for any misspellings or errors by the authors. After final proofreading, the manuscript may appear at the journal homepage as an article in press with a unique DOI number for rapid communication. All published articles will be replaced by the replacement XML file and a final PDF.

***Feedback after publication***

If the authors or readers find any errors, or contents that should be revised, it can be requested from the Editorial Board. The Editorial Board may consider erratum, corrigendum or a retraction. If there are any revisions to the article, there will be a CrossMark description to announce the final draft. If there is a reader's opinion on the published article with the form of Letter to the editor, it will be forwarded to the authors. The authors can reply to the reader's letter. Letter to the editor and the author's reply may be also published.

***How the journal handle complaints and appeals***

The policy of JOET is primarily aimed at protecting the authors, reviewers, editors, and the publisher of the journal. If not described below, the process of handling complaints and appeals follows the guidelines of the Committee of Publication Ethics available from: https://publicationethics.org/appeals

- *Who complains or makes an appeal?*

Submitters, authors, reviewers, and readers may register complaints and appeals in a variety of cases as follows: falsification, fabrication, plagiarism, duplicate publication, authorship dispute, conflict of interest, ethical treatment of animals, informed consent, bias or unfair/inappropriate competitive acts, copyright, stolen data, defamation, and legal problem. If any individuals or institutions want to inform the cases, they can send a letter via the contact page on our website: https://www.joet.org/about/contact.php. For the complaints or appeals, concrete data with answers to all factual questions (who, when, where, what, how, why) should be provided.

- *Who is responsible to resolve and handle complaints and appeals?*

The Editorial Board or Editorial Office is responsible for them. A legal consultant or ethics editor may be able to help with the decision making.

- *What may be the consequence of remedy?*

It depends on the type or degree of misconduct. The consequence of resolution will follow the guidelines of the Committee of Publication Ethics (COPE).

## Article processing charge

***Payment due***

Article processing charge (APC) covers the range of publishing services JOET provides. This includes provision of online tools for editors and authors, article production and hosting, and customer services. Upon editorial acceptance of an article for the regular review service and upon submission of an article for the fast review service, the corresponding author will be notified that payment is due.

***APC***

The APC up to 6 pages is ₩200,000 (or ＄200) for the regular review service and ₩550,000 (or ＄550) for the fast review service. For papers longer than 6 pages, an extra APC of $30 per page is charged. No taxes are included in this charge.

***Payment methods***

*Credit card payment* can be made online using a secure payment form as soon as the manuscript has been editorially accepted. We will we send a receipt by email once payment has been processed. Please note that payment by credit card carries a surcharge of 10% of the total APC.

*Invoice payment* is due within 7 days of the manuscript receiving editorial acceptance. Receipts are available on request.

Journal of Ocean Engineering and Technology 00(0), 000-000, December, 2100
https://doi.org/10.26748/KSOE.2100.000
pISSN 1225-0767
eISSN 2287-6715
Original Research Article, Technical Article, Review Article, etc

# Title of Article

Firstname Lastname[1], Firstname Lastname[2] and Firstname Lastname[3]

[1]*Professor, Department of OO, OO School, OO University, Busan, Korea*
[2]*Graduate Student, Department of OO, OO University, Seoul, Korea*
[3]*Senior Researcher, Department of OO, OO Engineering. Corp., Seoul, Korea*

**KEY WORDS:** Lumped mass line model, Explicit method, Steel lazy wave riser (Immediately after the abstract, provide a maximum of 5 or 6 keywords.)

**ABSTRACT:** *A concise and factual abstract is required. The abstract should state briefly the purpose of the research, the principal results and major conclusions. An abstract should be written in around 300 words and is often presented separately from the article, so it must be able to stand alone. For this reason, References should be avoided, but if essential, then cite the author(s) and year(s). Also, non-standard or uncommon abbreviations should be avoided, but if essential they must be defined at their first mention in the abstract itself.*

## Nomenclature

| | |
|---|---|
| *ITOC* | Increment of total operating cost ($/yr) |
| *LHV* | Lower heating value (kJ/kg) |
| *Pw* | Power (kW) |
| *T* | Temperature (K) |
| *V* | Volume ($m^3$) |
| $\rho$ | Density ($kg/m^3$) |

## 1. Introduction

The introduction should briefly place the study in a broad context and highlight why it is important. It should define the purpose of the work and its significance. The current state of the research field should be reviewed carefully and key publications cited. Please highlight controversial and diverging hypotheses when necessary. Finally, briefly mention the main aim of the work and highlight the principal conclusions. As far as possible, please keep the introduction comprehensible to scientists outside your particular field of research.

## 2. General Information for Authors

### 2.1 Requirement for Membership

One of the authors who submits a paper or papers should be member of The Korea Society of Ocean Engineers (KSOE), except a case that editorial board provides special admission of submission.

### 2.2 Publication type

Manuscript is made up of scholarly monographs, technical reports and data. The paper should have not been submitted to other academic journal. Conference papers, research reports, dissertations and review articles can be submitted to Journal Of Ocean Engineering and Technology (JOET). When part or whole of a paper was already published to conference papers, research reports, dissertations, and review articles, then corresponding author should note it clearly in the manuscript. After published to JOET, the copyright of manuscript belongs to KSOE.

(example) It is noted that this paper is revised edition based on proceedings of KAOST 2100 in Jeju.

### 2.3 Manuscript submission

Manuscript should be submitted through the on-line manuscript website (http://www.joet.org). The date that corresponding author submits a paper through on-line website is official date of submission. Other correspondences can be sent by an email to the Editor in Chief. The manuscript must be accompanied by a signed statement that it has been neither published nor currently submitted for publication elsewhere. The manuscript should be written in English or Korean and a

Received 00 February 2100, revised 00 October 2100, accepted 00 October 2100
Corresponding author Firstname Lastname: +82-51-759-0656, e-mail@e-mail.com
It is a recommended paper from the proceedings of 2019 spring symposium of the Korea Marine Robot Technology (KMRTS).

minimum standard of the proficiency in the English or Korean language should be met before submission to the editorial office.

Ensure that online submission or submission by e-mail text files are in a standard word processing format (Hangul or MS Word are preferred). Ensure that graphics are high-resolution. Be sure all necessary files have been uploaded/attached.

2.3.1 Authoer's checklist and Transfer of copyright

Authoer's checklist and Transfer of copyright can be found in submission hompage (http:/www.joet.org).

### 2.4 Research and Publication Ethics

Authorship should be limited to those who have made a significant contribution to the conception, design, execution, or interpretation of the reported study. All those who have made significant contributions should be listed as co-authors. Where there are others who have participated in certain substantive aspects of the research project, they should be acknowledged or listed as contributors.

The corresponding author should ensure that all appropriate co-authors and no inappropriate co-authors are included on the paper, and that all co-authors have seen and approved the final version of the paper and have agreed to its submission for publication.

Details on publication ethics are found in the journal's website (http://joet.org/authors/ethics.php). For the policies on research and publication ethics not stated in the Instructions, Guidelines on Good Publication (http://publicationethics.org/) can be applied.

## 3. Manuscript

Manuscript must consist of as follow: (1) Title, (2) Author's information (include title), (3) Key word, (4) Abstract, (5) Nomenclature description, (6) Introduction, (7) Body (analysis, test, results and discussion, (8) Conclusion, (9) Acknowledgements, (10) Reference, (11) Appendix, etc.

### 3.1 Unit

Use the international system units(SI). If other units are mentioned, please give their equivalent in SI.

### 3.2 Equations

All mathematical equations should be clearly printed/typed using well accepted explanation. Superscripts and subscripts should be typed clearly above or below the base line. Equation numbers should be given in Arabic numerals enclosed in parentheses on the right-hand margin. They should be cited in the text as, for example, Eq. (1), or Eqs. (1)-(3).

$$G_{GEV}(x;\mu,\sigma,\xi)=\begin{cases}\exp[-(1+\xi(x-\mu)/\sigma)^{-1/\xi}] & \xi\neq 0\\ \exp[-\exp(-(x-\mu)/\sigma)] & \xi=0\end{cases} \quad (1)$$

in which $\mu$, $\sigma$, and $\xi$ represent the location ("Shift" in figures), scale, and shape parameters, respectively.

### 3.3 Tables

Tables should be numbered consecutively with Arabic numerals. Each table should be typed on a separate sheet of paper and be fully titled. All tables should be referred to in the text.

**Table 1** Tables should be placed in the main text near to the first time they are cited

| Item | Buoyancy riser |
|---|---|
| Segment length[1] (m) | 370 |
| Outer diameter (m) | 1.137 |
| Inner diameter (m) | 0.406 |
| Dry weight (kg/m) | 697 |
| Bending rigidity ($N\cdot m^2$) | 1.66E8 |
| Axial stiffness (N) | 7.098E9 |
| Inner flow density ($kg\cdot m^3$) | 881 |
| Seabed stiffness ($N/m/m^2$) | 6,000 |

[1]Tables may have a footer.

### 3.4 Figures

All the illustrations should be of high quality meeting with the publishing requirement with legible symbols and legends. In preparing the illustrations, authors should consider a size reduction during the printing process to have acceptable line clarity and character sizes. All figures should have captions. They should be referred to in the text as, for example, Fig. 1, or Figs. 1-3.

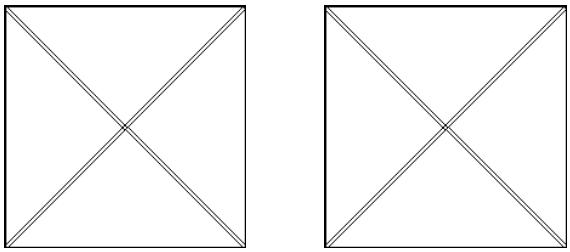

(a) Description of what is contained in the first panel

(b) Description of what is contained in the first panel

**Fig. 1** Schemes follow the same formatting. If there are multiple panels, they should be listed as: (a) Description of what is contained in the first panel; (b) Description of what is contained in the second panel. Figures should be placed in the main text near to the first time they are cited

### 3.5 How to describe the references in main texts

All references should be listed at the end of the manuscripts, arranged in order of Alphabet. References in texts follow the American Psychological Association (APA) style. The exemplary form of listed references is as follows:

Single author: (Kim, 1998) or Kim (1998)

Two authors: (Kim and Lee, 2000) or Kim and Lee (2000)

Three or more authors: (Kim et al., 1997) or Kim et al. (1997)

Two or more papers: (Lee, 1995a; Lee, 1995b; Ryu et al., 1998)

Year unknown: (Kim, n.d.) or Kim (n.d.)

## 4. Results

This section may be divided by subheadings. It should provide a concise and precise description of the experimental results, their interpretation as well as the experimental conclusions that can be drawn. Tables and figures are recommended to present the results more rapidly and easily. Do not duplicate the content of a table or a figure with in the Results section. Briefly describe the core results related to the conclusion in the text when data are provided in tables or in figures. Supplementary results can be placed in the Appendix.

## 5. Discussion

Authors should discuss the results and how they can be interpreted in perspective of previous studies and of the working hypotheses. The findings and their implications should be discussed in the broadest context possible. Future research directions may also be highlighted

## 6. Conclusions

This section can be added to the manuscript.

## Funding

Please add: “This research was funded by Name of Funder, grant number XXX” and “The OOO was funded by XXX”. Check carefully that the details given are accurate and use the standard spelling of funding agency names at https://search.crossref.org/funding

## Acknowledgments

In this section you can acknowledge any support given which is not covered by the author contribution or funding sections. This may include administrative and technical support, or donations in kind (e.g., materials used for experiments). For mentioning any persons or any organizations in this section, there should be a written permission from them.

## Conflict of interest

It should be disclosed here according to the statement in the Research and publication ethics regardless of existence of conflict of interest. If the authors have nothing to disclose, please state: “No potential conflict of interest relevant to this article was reported.”

## References

- Journal name should not be abbreviated.
- A private report with limited access or download availability can not be a reference.
- Include the digital object identifier DOI or URL for all references where available.
- Reference list follows the American Psychological Association (APA) style.

Referring to journal publications:

Author, A.A., Author, B.B., & Author, C.C. (Year). Title of Article. Journal Title, vol(no), pp-pp. https://doi.org/xx.xxxx/xxxxxx

Author, A.A., Author, B.B., Author, C.C. (accepted; in press). Title of Article. Title of Periodical. Retrieved from http://xx.xxx/x.pdf

Lee, T.K., Kim, T.W., Rim, C.W., & Kim, S.C. (2013). A Study on Calculation of Local Ice Pressures for ARAON Based on Data Measured at Arctic Sea. Journal of Ocean Engineering and Technology, 27(5), 88-92. https://doi.org/10.5574/KSOE.2013.27.5.088

Lee, T.K., Kim, T.W., Rim, C.W., & Kim, S.C. (accepted; in press). A Study on Calculation of Local Ice Pressures for ARAON Based on Data Measured at Arctic Sea. Journal of Ocean Engineering and Technology, Retrieved from http://xxx.xxx/xxx.pdf

Referring to conference proceedings:

Author, A.A., Author, B.B., & Author, C.C. (Year). Title of Article. Proceeding Title, City, Country, pp-pp. https://doi.org/xx.xxxx

Aoki, S., Liu, H., & Sawaragi, T. (1994). Wave Transformation and Wave Forces on Submerged Vertical Membrane. Proceedings of International Symposium Waves - Physical and Numerical Modeling, Vancouver, Canada, 1287-1296.

Tsukamoto, C.L., Lee, W., Yuh, J., Choi, S.K., & Lorentz, J. (1997). Comparison Study on Advanced Thruster Control of Underwater Robots. Proceedings of International Conference on Robotics and Automation, 1845-1850. https://doi.org/110.1109/ROBOT. 1997.619056

Referring to books:

Author, A.A. (Year). Title of Book (xx ed.). Location: Publisher.

Strunk, W., & White, E.B. (2000). The Elements of Style (4th ed.). NewYork, USA: Longman.

Schlichting, H. (1968). Boundary Layer Theory (6th ed.). New York, USA: McGraw-Hill.

Referring to theses or dissertations:

Author, A.A. (Year). Title of Doctoral Dissertation or Master’s thesis (Doctoral Dissertation or Master’s thesis). Name of Institution, City, Country.

Giovanni, I. (1998). Modelling and Identification of Underwater Robotic Systems (Ph.D. Thesis). University of Genova, Genova, Italy.

Referring to technical reports, rules, or guidelines:

Author, A.A. (Year). Title of report (Reprot No. xxx), Location: Publisher.

Likhomanov, V. (2010). Full-Scale Ice Trials of the Korean Research Icebreaker ARAON. Daejeon, Korea: Arctic and Antarctic Research Institute (AARI).

ABS. (2011). Guide for Ice Loads Monitoring Systems. Houston, USA: American Bureau of Shipping.

Lloyd’s Register. (2011). FDA ICE Fatigue Induced by Ice Loading,

ShipRight Design and construction - Fatigue Design Assesment. London, United Kingdom: Lloyd's Register.

Larson, M., & Kraus, N.C. (1989). SBEACH: Numerical Model for Simulating Storm-Induced Beach Change - Report 1 Empirical Foundation and Model Development (Technicla Report CERC-89-9). Coastal Engineering research center Vicksburg Ms.

Referring to patents:

Righsholder, A.A. (Year). Title of Patent. Patent number, Patent office with country.

Dawoo Shipbulding & Maringe Engineering (DSME). (2013). Distance Length Standardization Method for Preventing Interference at the time of Uploading Cell Guide of Container Ship. Unexamined Patent Publication 1020130044635, Korean Interllectual Property Office.

Referring to websites:

Righsholder, A.A. (Year). Title of webpage. Retrieved Month Year from http://xxxx

International Association of Classification Societies (IACS). (2010a). Common Structural Rules for Bulk Carriers. Retrieved July 2010 from http://www.iacs-data.org.uk

US Congressional Hearing. (2009). Strategic Importance of the Arctic in Us Policy. Retrieved June 2019 from https://fas.org/irp/arctic.pdf

Dawoo Shipbulding & Maringe Engineering (DSME). (2013). Distance Length Standardization Method for Preventing Interference at the time of Uploading Cell Guide of Container Ship. Retrieved June 2019 from https://patentimages.storage./pdfs/792.pdf

Referring to software:

Righsholder, A.A. (Year). Title of Software. Downloaded Month Year from http://xxxx

Referring to some exceptional cases:

- when authors are missing, institution can replace authors

National Oceanic and Atmospheric Administration (NOAA). (2015). Deep-ocean Assessment and Reporting of Tsunamis (DART). Retrieved December 2019 from https://nctr.pmel.noaa.gov/Dart/

- when dates or years are missing, it is replaced with "n.d."

National Oceanic and Atmospheric Administration (NOAA). (n.d.). Deep-ocean Assessment and Reporting of Tsunamis (DART).

- when more then seven authors, first 6 authors ... last author.

Yeu, T., Choi, H.T., Lee, Y., Chae, J., Lee, Y., Kim, S.S., ... Lee, T.H. (2019). Development of Robot Platform for Autonomous Underwater Intervention. Journal of Ocean Engineering and Technology, 33(2), 168-177. https://doi.org/10.26748/KSOE.2019.021

## Appendix

The appendix is an optional section that can contain details and data supplemental to the main text. For example, explanations of experimental details that would disrupt the flow of the main text, but nonetheless remain crucial to understanding and reproducing the research shown; figures of replicates for experiments of which representative data is shown in the main text can be added here if brief, or as Supplementary data. Mathematical proofs of results not central to the paper can be added as an appendix.

All appendix sections must be cited in the main text. In the appendixes, Figures, Tables, etc. should be labeled starting with 'A', e.g., Fig. A1, Fig. A2, etc.

Examples:

https://doi.org/10.26748/KSOE.2019.022

https://doi.org/10.26748/KSOE.2018.4.32.2.095

## Author ORCIDs

All authors are recommended to provide an ORCID. To obtain an ORCID, authors should register in the ORCID web site: http://orcid.org. Registration is free to every researcher in the world. Example of ORCID description is as follows:

| **Author name** | **ORCID** |
|---|---|
| So, Hee | 0000-0000-000-00X |
| Park, Hye-Il | 0000-0000-000-00X |
| Yoo, All | 0000-0000-000-00X |
| Jung, Jewerly | 0000-0000-000-00X |

# Authors' Checklist

The following list will be useful during the final checking of a manuscript prior to sending it to the journal for review. Please submit this checklist to the KSOE when you submit your article.

### < Checklist for manuscript preparation >

☐ I checked my manuscript has been 'spell-checked' and 'grammar-checked'.
☐ One author has been designated as the corresponding author with contact details such as
- E-mail address
- Phone numbers

☐ I checked abstract 1) stated briefly the purpose of the research, the principal results and major conclusions, 2) was written in around 300 words, and 3) did not contain references (but if essential, then cite the author(s) and year(s)).
☐ I provided 5 or 6 keywords.
☐ I checked color figures were clearly marked as being intended for color reproduction on the Web and in print, or to be reproduced in color on the Web and in black-and-white in print.
☐ I checked all table and figure numbered consecutively in accordance with their appearance in the text.
☐ I checked abbreviations were defined at their first mention there and used with consistency throughout the article.
☐ I checked all references mentioned in the Reference list were cited in the text, and vice versa according to the APA style.
☐ I checked I used the international system units (SI) or SI-equivalent engineering units.

### < Authorship checklist >

JOET considers individuals who meet all of the following criteria to be authors:

☐ Made a significant intellectual contribution to the theoretical development, system or experimental design, prototype development, and/or the analysis and interpretation of data associated with the work contained in the article.
☐ Contributed to drafting the article or reviewing and/or revising it for intellectual content.
☐ Approved the final version of the article as accepted for publication, including references.

### < Checklist for publication ethics >

☐ I checked the work described has not been published previously (except in the form of an abstract or as a part of a published lecture or academic thesis).
☐ I checked when the work described has been published previously in other proceedings without copyright, it has clearly noted in the text.
☐ I checked permission has been obtained for use of copyrighted material from other sources including the Web.
☐ I have processed Plasgiarism Prevention Check through reliable web sites such as www.kci.go.kr, http://www.ithenticate.com/, or https://www.copykiller.org/ for my submission.
☐ I agree that final decision for my final manuscript can be changed according to results of Plasgiarism Prevention Check by JOET administrator.
☐ I checked one author at least is member of the Korean Society of Ocean Engineers.
☐ I agreed all policies related to 'Research and Publication Ethics'
☐ I agreed to transfer copyright to the publisher as part of a journal publishing agreement and this article will not be published elsewhere including electronically in the same form, in English or in any other language, without the written consent of the copyright-holder.
☐ I made a payment for reviewing of the manuscript, and I will make a payment for publication on acceptance of the article.
☐ I have read and agree to the terms of Authors' Checklist.

| | | |
|---|---|---|
| Title of article | : | |
| Date of submission | : DD/MM/YYYY | |
| Corresponding author | : | signature |
| Email address | : | |

※ E-mail this with your signature to ksoehj@ksoe.or.kr

# Publishing Agreement

## ARTICLE DETAILS

Title of article :

Corresponding author :

E-mail address :

DOI : https://doi.org/10.26748/KSOE.2XXX.XXX

## YOUR STATUS

I am one author signing on behalf of all co-authors of the manuscript.

## ASSIGNMENT OF COPYRIGHT

I hereby assign to the Korean Society of Ocean Engineers, the copyright in the manuscript identified above and any tables, illustrations or other material submitted for publication as part of the manuscript (the "Article"). This assignment of rights means that I have granted to Korean Society of Ocean Engineers the exclusive right to publish and reproduce the Article, or any part of the Article, in print, electronic and all other media (whether now known or later developed), in any form, in all languages, throughout the world, for the full term of copyright, and the right to license others to do the same, effective when the Article is accepted for publication. This includes the right to enforce the rights granted hereunder against third parties.

## SCHOLARLY COMMUNICATION RIGHTS

I understand that no rights in patents, trademarks or other intellectual property rights are transferred to the Journal owner. As the author of the Article, I understand that I shall have: (i) the same rights to reuse the Article as those allowed to third party users of the Article under the CC-BY-NC License, as well as (ii) the right to use the Article in a subsequent compilation of my works or to extend the Article to book length form, to include the Article in a thesis or dissertation, or otherwise to use or re-use portions or excerpts in other works, for both commercial and non-commercial purposes. Except for such uses, I understand that the assignment of copyright to the Journal owner gives the Journal owner the exclusive right to make or sub-license commercial use.

## USER RIGHTS

The publisher will apply the Creative Commons Attribution-Noncommercial Works 4.0 International License (CC-BY-NC) to the Article where it publishes the Article in the journal on its online platforms on an Open Access basis.
The CC-BY-NC license allows users to copy and distribute the Article, provided this is not done for commercial purposes and further does not permit distribution of the Article if it is changed or edited in any way, and provided the user gives appropriate credit (with a link to the formal publication through the relevant DOI), provides a link to the license, and that the licensor is not represented as endorsing the use made of the work. The full details of the license are available at http://creativecommons.org/licenses/by-nc/4.0/legalcode.

## REVERSION OF RIGHTS

Articles may sometimes be accepted for publication but later rejected in the publication process, even in some cases after public posting in "Articles in Press" form, in which case all rights will revert to the author.

**☑ I have read and agree to the terms of the Journal Publishing Agreement.**

Corresponding author:

name signature

※ E-mail this with your signature to ksoehj@ksoe.or.kr (Papers will not be published unless this form is signed and returned)

# Research and Publication Ethics

Journal of Ocean Engineering and Technology (JOET) adheres to the guidelines published by professional organizations, including Committee on Publication Ethics (COPE; https://publicationethics.org/)

## 1. Authorship

***JOET considers individuals who meet all of the following criteria to be authors:***

1) Made a significant intellectual contribution to the theoretical development, system or experimental design, prototype development, and/or the analysis and interpretation of data associated with the work contained in the article.
2) Contributed to drafting the article or reviewing and/or revising it for intellectual content.
3) Approved the final version of the article as accepted for publication, including references.

Contributors who do not meet all of the above criteria may be included in the Acknowledgment section of the article. Omitting an author who contributed to your article or including a person who did not fulfill all of the above requirements is considered a breach of publishing ethics.

***Correction of authorship after publication:*** JOET does not correct authorship after publication unless a mistake has been made by the editorial staff.

## 2. Originality and Duplicate Publication

All submitted manuscripts should be original and should not be in consideration by other scientific journals for publication. Any part of the accepted manuscript should not be duplicated in any other scientific journal without permission of the Editorial Board, although the figures and tables can be used freely if the original source is verified according to the Creative Commons Attribution License (CC BY-NC). It is mandatory for all authors to resolve any copyright issues when citing a figure or table from other journal that is not open access.

## 3. Conflict-of-Interest Statement

Conflict of interest exists when an author or the author's institution, reviewer, or editor has financial or personal relationships that inappropriately influence or bias his or her actions. Such relationships are also known as dual commitments, competing interests, or competing loyalties. These relationships vary from being negligible to having a great potential for influencing judgment. Not all relationships represent true conflict of interest. On the other hand, the potential for conflict of interest can exist regardless of whether an individual believes that the relationship affects his or her scientific judgment. Financial relationships such as employment, consultancies, stock ownership, honoraria, and paid expert testimony are the most easily identifiable conflicts of interest and the most likely to undermine the credibility of the journal, the authors, or of the science itself. Conflicts can occur for other reasons as well, such as personal relationships, academic competition, and intellectual passion. If there are any conflicts of interest, authors should disclose them in the manuscript. The conflicts of interest may occur during the research process as well; however, it is important to provide disclosure. If there is a disclosure, editors, reviewers, and reader can approach the manuscript after understanding the situation and the background of the completed research.

## 4. Management Procedures for the Research and Publication Misconduct

When JOET faces suspected cases of research and publication misconduct such as a redundant (duplicate) publication, plagiarism, fabricated data, changes in authorship, undisclosed conflicts of interest, an ethical problem discovered with the submitted manuscript, a reviewer who has appropriated an author's idea or data, complaints against editors, and other issues, the resolving process will follow the flowchart provided by the Committee on Publication Ethics (http://publicationethics.org/resources/flowcharts). The Editorial Board of JOET will discuss the suspected cases and reach a decision. JOET will not hesitate to publish errata, corrigenda, clarifications, retractions, and apologies when needed.

## 5. Editorial Responsibilities

The Editorial Board will continuously work to monitor and safeguard publication ethics: guidelines for retracting articles; maintenance of the integrity of the academic record; preclusion of business needs from compromising intellectual and ethical standards; publishing corrections, clarifications, retractions, and apologies when needed; and excluding plagiarism and fraudulent data. The editors maintain the following responsibilities: responsibility and authority to reject and accept articles; avoiding any conflict of interest with respect to articles they reject or accept; promoting publication of corrections or retractions when errors are found; and preservation of the anonymity of reviewers.

## 6. Hazards and human or animal subjects

If the work involves chemicals, procedures or equipment that have any unusual hazards inherent in their use, the author must clearly identify these in the manuscript. If the work involves the use of animal or human subjects, the author should ensure that the manuscript contains a statement that all procedures were performed in compliance with relevant laws and institutional guidelines and that the appropriate institutional committee(s) has approved them. Authors should include a statement in the manuscript that informed consent was obtained for experimentation with human subjects. The privacy rights of human subjects must always be observed.

Ensure correct use of the terms sex (when reporting biological factors) and gender (identity, psychosocial or cultural factors), and, unless inappropriate, report the sex and/or gender of study participants, the sex of animals or cells, and describe the methods used to determine sex and gender. If the study was done involving an exclusive population, for example in only one sex, authors should justify why, except in obvious cases. Authors should define how they determined race or ethnicity and justify their relevance.

## 7. Secondary publication

It is possible to republish manuscripts if the manuscripts satisfy the conditions of secondary publication. These are:

- The authors have received approval from the Editorial Board of both journals (the editor concerned with the secondary publication must have access to the primary version).
- The priority for the primary publication is respected by a publication interval negotiated by editors of both journals and the authors.
- The paper for secondary publication is intended for a different group of readers
- The secondary version faithfully reflects the data and interpretations of the primary version.
- The secondary version informs readers, peers, and documenting agencies that the paper has been published in whole or in part elsewhere, for example, with a note that might read, "This article is based on a study first reported in the [journal title, with full reference]"
- The title of the secondary publication should indicate that it is a secondary publication (complete or abridged republication or translation) of a primary publication.

## 8. Complaints and Appeals

The process of handling complaints and appeals follows the guidelines of the COPE available from: https://publicationethics. org/appeals

## 9. Post-publication discussions and corrections

The post-publication discussion is available through letter to editor. If any readers have a concern on any articles published, they can submit letter to editor on the articles. If there found any errors or mistakes in the article, it can be corrected through errata, corrigenda, or retraction.


The Korean Society of Ocean Engineers